Gas Separation Exploiting Molecular Trapdoors in Small Pore Zeolites

Alexander, Thomas

Award date:
2019

Awarding institution:
University of Bath

Gas Separation Exploiting Molecular Trapdoors in Small Pore Zeolites

Thomas Alexander

A thesis submitted for the degree of Doctor of Philosophy

University of Bath

Department of Chemical Engineering

May 2019

Declaration of authorship and previous submission of work

The material presented here, for examination for the award of a higher degree by research, has not been incorporated into a submission for another degree. Wherever contributions of others are involved in the work, every effort has been made to indicate this clearly, with due reference to literature and acknowledgement of collaborative research and discussions.

Candidate's signature:

Thomas Alexander

Abstract

Zeolite RHO has recently been identified as a promising candidate for the separation of CO_2 and CH_4. This is due to the presence of extraframework cations in the eight membered rings (8MR) which occupy the spaces between cages and act as gatekeepers, selectively allowing the uptake of CO_2 but restricting the uptake of CH_4.

The mechanism by which the cations move to allow the passage of CO_2 molecules is not fully understood and computationally has only been studied at the quantum level. This does not allow the gating phenomenon to be observed directly and so the aim of this work is to use faster classical simulations to gain insight into the separation mechanism.

Zeolite RHO is a particularly flexible zeolite and on gas loading undergoes both a phase transition and cell expansion. This makes these simulations particularly challenging to model correctly. One of the first stages in this work is therefore to ensure that the behaviour framework is reproduced adequately.

Using an optimised set of force field parameters, two mechanisms are found for CO_2 diffusion. The first occurs when a gate-keeping 8MR cation is pushed through a double eight ring (D8R) by a CO_2 molecule and the second, less common mechanism, occurs when the D8R is completely unoccupied by a cation.

The work focuses mainly on the diffusion of CO_2 but other gases are also examined. Studies of the diffusion of noble gases through Na-RHO show that Xe and Kr are blocked by Na^+ cations, whilst Ar shows low diffusivity. He shows very high diffusivity due to its small size. The gas diffusion rates through RHO can be tuned by adjusting the Si/Al ratio as well as the choice of cation. For mixed Li/Na-RHO systems, increasing the Na^+ content increases CO_2 equilibrium uptake but leads to a drop in diffusivity. Higher silicon content frameworks have larger limiting pore diameters, giving faster diffusion rates.

Acknowledgements

First of all, I would like to thank my supervisors, Professor Tina Düren, Dr Valeska Ting and Dr Carmelo Herdes at the University of Bath and Dr Carole Morrison at the University of Edinburgh for their valuable inputs through the course of the project.

I would also like to thank the three post-docs who I have worked with during my project: Dr Claire Hobday for her assistance in carrying out DFT simulations and discussions about crystallography; Dr Gaël Donval for his insights into Monte Carlo and Molecular Dynamics simulations and running them efficiently on HPC clusters; and Dr Stephen Wells for useful discussions about zeolites.

I would also like to say thank you to the other members of the EPSRC cation-gating consortium: Professor Stefano Brandani, Dr Enzo Mangano and Dr Maarten Verbraeken at the University of Edinburgh for carrying out practical adsorption work; Professor Paul Wright, Dr Veselina Georgieva, Dr Magdalena Lozinska and Elliott Bruce at the University of St. Andrews for synthesizing the samples and carrying out XRD measurements; Dr John Casci & Dr Alessandro Turrina at Johnson Matthey and Dr Bill Casteel at Air Products for providing useful industrial feedback.

I would like to say a particular thank you to Professor Julian Gale for providing invaluable assistance with GULP during the early days of the project. I would also like to thank Dr James Grant, Dr Tom Underwood and Dr Andrey Brukhno for help resolving problems with early versions of DL-MONTE and Professor Ilian Todorov and Dr Alin Marin Elena for help in sorting early problems encountered with DL-POLY. I am also grateful to Dr Marco Sant, Dr Carlos Nieto-Draghi and Dr Salvador Rodríguez-Gómez Balestra for assistance with various zeolite forcefields tried through the course of this project.

I would also like to thank everyone who helped me get started with molecular simulations as an undergraduate: Professor Tina Düren, Professor Lev Sarkisov, Dr Matthew Lennox, Dr Ana Maria Banu, Dr Linjiang Chen and Dr Peyman Moghadam.

I would also like to thank everyone in the IT departments at the University of Bath and University of Edinburgh who has provided support with both my office PC and their respective clusters (Balena and Eddie).

Finally, I would like to thank the University of Bath and EPSRC (grant number EP/N032918/1) for funding this project.

Table of Contents

1. **Introduction**

The separation of gases is not a spontaneous process and on an industrial plant is often one of the most energy intensive unit operations [1]. In a typical coal fired power station for example, an additional post-combustion carbon capture unit would typically consume 25-40% [2] of the station's total power output. Of this 70% would be used in the physical separation of gases, with the remaining 30% used for gas compression [3].

The three standard techniques used for industrial gas separations are cryogenic distillation, membrane separation and adsorption. Of these, adsorption is probably the most widely used [4].

In an adsorption process, a multicomponent stream of compressed gas is fed through a column filled with a porous, solid adsorbent. The rate at which different gas molecules diffuse through the column varies depending on the relative gas-solid interaction strength (thermodynamics) and the size of the gas molecules in relation to the size of the pores (kinetics). The time taken for a gas molecule to travel between the inlet and outlet of a column is known as the breakthrough time.

The time between the breakthrough of the first and subsequent components can be used to produce an enriched stream of the least strongly adsorbed component. During desorption and regeneration, when the solid is purged of adsorbed gases, an enriched stream of the more strongly adsorbed component can be produced.

Desorption occurs through one or both of lowering the pressure inside the column and heating the column. Either approach makes adsorption less favourable and results in detachment of molecules from the adsorbent. Once detached, the desorbed gas is purged by passing a non-adsorbing gas through the column (regeneration).

Both thermal swing and vacuum swing desorption are energetically demanding. Small improvements in performance can therefore translate to large cost and

energy savings on a full-scale industrial column. The three main targets for identifying a more promising adsorbent are:

i) Improving the equilibrium selectivity of an adsorbent (a measure of the relative strength of interaction between two components with the solid)
ii) Improving the kinetic selectivity (a measure of the relative gas diffusion rates through the solid)
iii) Lowering the heat of adsorption (the energy required to remove the gases during desorption).

Most adsorption columns make use of zeolites or activated carbons as adsorbents. Small-scale adsorption columns in niche applications sometimes also use metal organic frameworks (MOFs) [5]. The underlying mechanism for the separation of gases in these cases is normally via a difference in interaction energy (as above), or by molecular sieving.

Molecular sieving is a kinetic, rather than thermodynamic effect. If the size of a molecule is larger than the aperture of the solid's pores, it cannot easily diffuse through the solid. In the case where only the smaller component is able to diffuse through the column, a very high selectivity is achieved. However, if either the gas molecules or the framework are flexible and undergo a conformational change as the gas molecule approaches a pore window, diffusion of the larger gas molecules may still be possible. This often reduces the selectivity of the adsorbent.

In some cases, it is possible to take advantage of the flexible nature of a framework to achieve pore-size modification. This is where the framework is tuned either through atom substitution or through addition of a side chain so that the new pore size achieves a higher kinetic selectivity in a given separation.

In zeolite science, a third mechanism, cation gating, has recently come to the fore [6] [7] [8]. This occurs when extra-framework cations sit in the windows between pores and move temporarily away from the window when in the immediate vicinity of

certain gases. Below a critical admission temperature, where the cations have enough energy to migrate spontaneously away from their original sites [6], these cations act as barriers to gas diffusion.

Cations sitting in their equilibrium positions lie in a deep energy well, from which they are not easily dislodged. However, it is believed that gas molecules with an electronic quadrupole moment, dipole moment or high polarizability can flatten the energy well allowing the cation to move, reversibly, a short distance away from the centre of the host ring [6]. This temporary displacement allows a gas molecule to diffuse through the unoccupied window before the cation returns to its equilibrium position. This process is referred to as cation-gating or trapdoor separation.

One of the first high selectivity trapdoor separations was described for the chabazite (CHA) family of zeolites [6]. For the CO_2/CH_4 separation at 10 bar and 273 K, a pure component CO_2/CH_4 selectivity[1] of 21 was recorded for K-CHA (Si/Al = 1.2). At 273 K and 100 kPa, the pure component selectivity increased to 93. In a binary breakthrough experiment consisting of 15 % CO_2 and 85% CH_4 (v/v) at 293 K and 116 kPa, a CO_2/CH_4 separation of 79 was recorded.

Trapdoor separations can be the underlying cause of unusual 'size inversion' separations [6]. For example, in the separation[2] of CO (σ = 3.76 Å) and N_2 (σ = 3.64 Å) by Cs-CHA (Si/Al = 2.5) at 273 K in a range of pressures between 0.1 and 1-bar, the reported selectivity of larger CO over smaller N_2 is ≈7. This unusual effect occurs because CO is able to pull the Cs^+ cation away from the 8MR whilst N_2 cannot.

[1] The pure component selectivity at a given temperature and pressure is defined as: the moles of gas of species A adsorbed / moles of gas of species B adsorbed

[2] σ is defined here as the kinetic diameter. (Throughout the rest of the work it is used to represent the Lennard-Jones parameter.)

The aim of this work is to understand trapdoor phenomena in the less well studied zeolite RHO system using a range of computational approaches. The study focuses on developing an accurate model that agrees with existing experimental data for the Na-RHO structure, both with and without adsorbed CO_2. The work is then extended to other gases of interest and onto trapdoor behaviour and pore size modification in Li-RHO and Li/Na mixtures.

Molecular simulations offer an easy way to observe the cation gating phenomena and quantify the energetic barriers that must be overcome for gas diffusion. The ultimate aim of the study is to work towards a model that allows a range of RHO type zeolites to be quickly assessed, identifying where experimental efforts should be targeted in tailoring a RHO zeolite for a given separation of interest.

In Chapter 2, the structure of zeolite RHO is introduced and then the range of simulation techniques used in this work are summarised. A short literature review for zeolite RHO is also provided.

In Chapter 3, the quality of the parameters used in the work is assessed against a range of key structural properties including the unit cell length and framework expansion on CO_2 loading. In particular, the choice of the cation parameters is found to have a significant effect on the cation distribution and CO_2 adsorption isotherm. Modifications are also made to the framework parameters to improve on the size and shape of the windows compared to those seen in DFT (Density Functional Theory) simulations and experimental work.

In Chapter 4, the diffusion mechanism of CO_2 through Na-RHO is examined. The energy barrier to CO_2 diffusion is calculated both with and without a cation present and the motion of intercage CO_2 is quantified using the best available model.

In Chapter 5, a range of different gas separations are examined, including the O_2/N_2 separation, separation of noble gases and CO_2/CH_4 separation.

In Chapter 6, the study is extended to investigate the degree to which it is possible to modify the size of the windows in zeolite RHO by adjusting the Si/Al ratio and changing the cation species.

In the final section (Chapter 7), an overview of the work is given with suggestions for future work.

A full description of all simulation parameters and a set of sample input files are provided in Appendices A - E.

2. Simulation techniques and theoretical background

2.1. Preface

This chapter outlines the key theoretical points relevant to the modelling of zeolites. First the structure of zeolite RHO [9] is introduced and then the molecular simulation techniques themselves. Finally, a literature summary of previous work into zeolite RHO is provided.

2.2. The structure of zeolite RHO

Like all zeolites, RHO is built up of a series of TO_4 tetrahedra (where T is a generic symbol used to represent either a silicon or an aluminium atom). These tetrahedra arrange into composite building units that may, in turn, be broken down into secondary building units (Table 2.1). Zeolite RHO comprises two composite building units (CBUs): a double 8-ring (D8R) and a Linde type A cage (*lta*). These CBUs are broken down into three secondary building units: four, six and eight membered rings.

Table 2.1: Composite building units for zeolite RHO and their constituent secondary building units [10]

Composite building units	Secondary building units		
			
lta cage	8MR	6MR	4MR
			
D8R cage	8MR	4MR	

Reprinted with permission from the Internal Zeolite Association. Copyright 2017. Credit to Ch. Baerlocher and L.B. McCusker, Database of Zeolite Structures, http://www.iza-structure.org/databases/ [10]

The composite building units act as building blocks that repeat regularly to produce a large 3D structure. This is shown in Figure 2.1, which shows a 2 x 2 x 2 RHO supercell. Emphasis is given to the D8Rs with lighter bonds used to show the set of connecting *lta* cages.

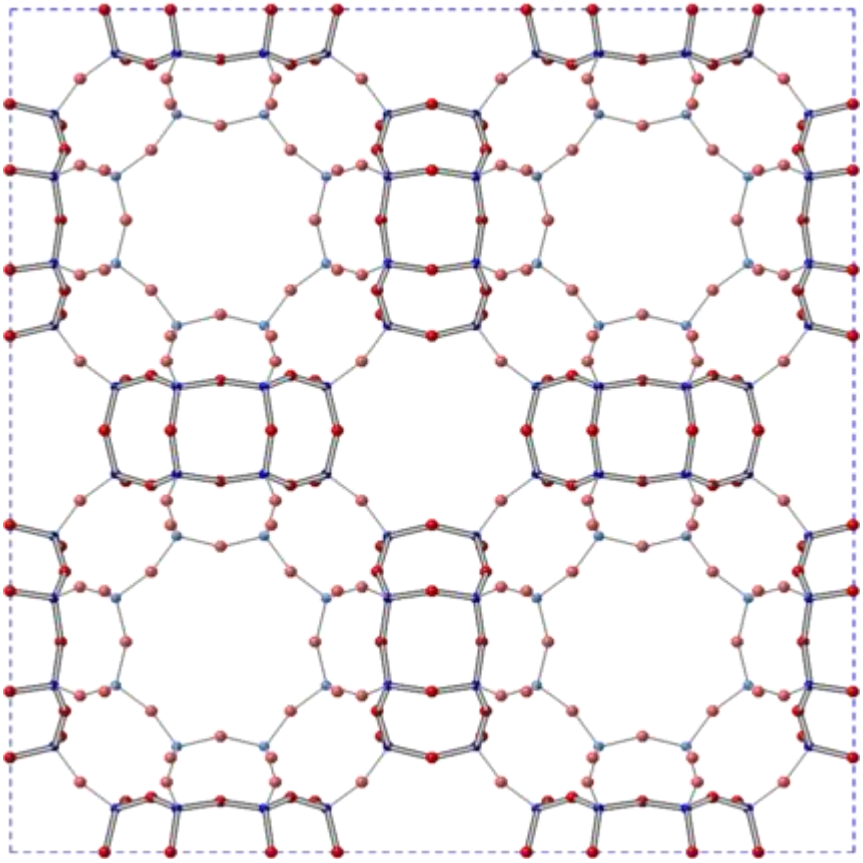

Figure 2.1: Expanded 2 x 2 x 2 supercell of zeolite RHO (Red = Oxygen, Blue = Silicon). The length of each dashed, bounding edge is 28.838 Å

In its simplest theoretical form, RHO would consist of silicon and oxygen only (Figure 2.1). During the synthesis stage however, a degree of aluminium substitution is required to stabilise the structure [11]. This stabilisation arises from a reduction in internal stress due to lower energy O-Al-O (rather than O-Si-O) interactions [11] coupled with the presence of extra framework cations, which have a templating [12] effect that help the structure grow. This is confirmed by DFT studies which show, for example, that the $[SiAlO(OH)_6]^-$ cluster formed during synthesis is four times lower in energy than the equivalent all silica $[Si_2O(OH)_6]^-$ form [13].

A result of substituting silicon atoms (which have a formal charge of +4) for aluminium atoms (which have a formal charge of +3) is that the framework has a net negative charge. This net charge is compensated for by extra framework cations. These do not form part of the zeolite backbone but instead are mobile and are located in the zeolite cages/windows.

Extra framework cations in RHO sit in one of three sites: in the centre of a double 8 ring, in the centre of a single eight ring or in the centre/to the side of a six membered ring (6MR). For short time periods, cations may be found outside these regions but the three main sites (Figure 2.2) represent the bottom of an energy well from which the cations do not readily move. In this work, a cation is considered to be in a site if it is within a 3 Å radius of the positions below (Figure 2.2). Where a cation is within a 3 Å radius of more than one site, the location is taken as the site to which the cation is closest. Approximate locations of the cation sites are provided in Table 2.2.

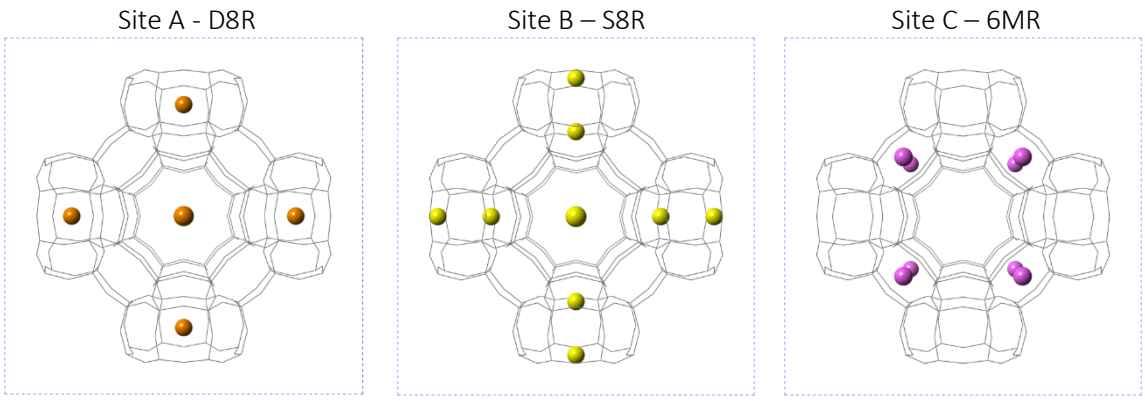

Figure 2.2: Location of cation sites in zeolite RHO

Table 2.2: Approximate fractional coordinates of cations in RHO zeolite

	Site A	Site B	Site C
Fractional coordinates	(0,0,1/2)	(0,0,1/3)	(1/3,1/3,1/3)

It is easiest to show RHO in a symmetrical form (as Figure 2.2) however it can exist in two phases (Figure 2.3), a highly symmetric form ($Im\bar{3}m$) or an acentric form ($I\bar{4}3m$). For fully dehydrated, cation-exchanged RHO at 300 K and 1 atm, with no gas molecules adsorbed, the acentric form is adopted. At atmospheric pressure, there is a gradual transition to the centric form with increasing

temperature, which is thought to complete at 800 K [14]. The transition is reversible and RHO regains the acentric form on cooling. Adsorption of gas molecules, such as CO_2, also causes a gradual transition from the acentric to centric form [15].

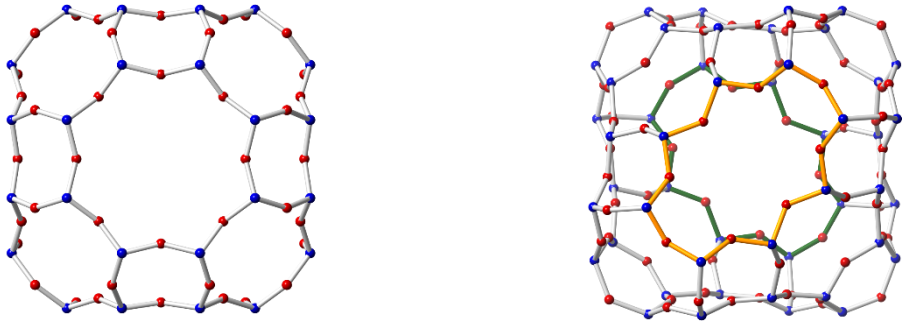

centric ($Im\bar{3}m$) acentric ($I\bar{4}3m$)

Figure 2.3 centric and acentric forms of RHO with highlighted 8MR rings in the acentric form (yellow ring in front of the green ring)

A quantitative measure of the distortion, Δ, was introduced by Parise et al. [14] when looking at the structural changes in RHO at increasing temperature. This Δ parameter describes the difference between the length and width of an 8MR. In the strictest definition, a zeolite is only in the centric form when all the 8MRs have Δ = 0. Using the time and ring averaged expression in Equation (2.1), it is also possible to describe the phase on a continuum. Experimentally, a given sample of RHO zeolite will be described by the space group that gives the strongest fit during refinement.

$$\Delta_8 = \frac{1}{2}\langle |\boldsymbol{r_{AE}} - \boldsymbol{r_{CG}}| \rangle \tag{2.1}$$

where the oxygen atoms in a ring are defined sequentially from A to H and the separation distance *r* between two atoms, *i* and *j* is given by Equation (2.2).

$$\boldsymbol{r_{ij}} = |\boldsymbol{r_i} - \boldsymbol{r_j}| \tag{2.2}$$

The same idea has been extended to describe the distortion of four and six membered rings (Figure 2.4) [16]:

$$\Delta_4 = \frac{1}{2}|\boldsymbol{r_{AC}} - \boldsymbol{r_{BD}}| \tag{2.3}$$

$$\Delta_6 = \frac{1}{2}[\max(r_{AD}, r_{BE}, r_{CF}) - \min(r_{AD}, r_{BE}, r_{CF})] \quad (2.4)$$

For the 4MR, only one value of Δ can be calculated (AC-BD), for the 6MR there are three alternatives (AD-BE/AD-CF/BE-CF) and for the 8MR, there are two alternatives (AE-CG/BF-DH). In the latter two cases, the option which maximises Δ is used.

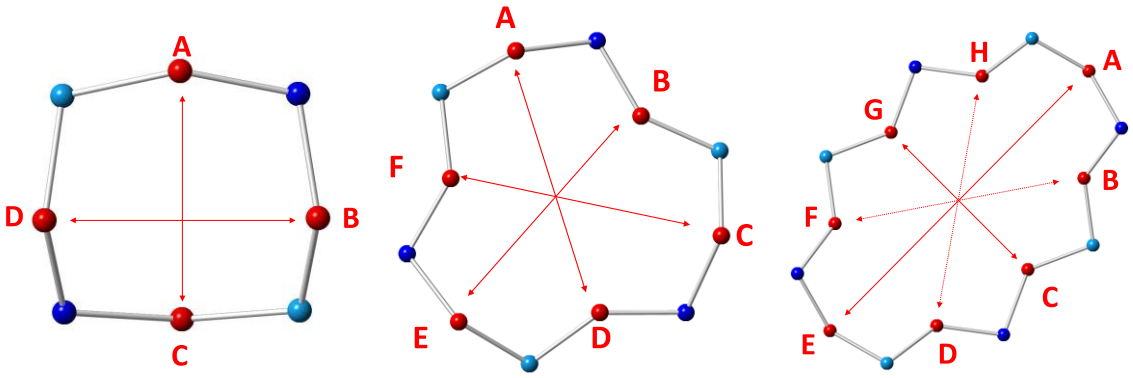

4MR distortion 6MR distortion 8MR distortion

Figure 2.4: Distortion in 4MRs, 6MRs and 8MRs.

2.3. Aluminium distribution in zeolite RHO

The distribution of silicon and aluminium atoms within a zeolite is disordered and difficult to determine experimentally [17]. In a select few cases, e.g. ferrierite (FER) [18] and ZSM-5 [19], a full (FER) and partial (ZSM-5) refinement of the aluminium locations is possible by combining ^{27}Al 3Q MAS NMR spectroscopy with DFT calculations, although this is very unusual. The aluminium distribution is also dependent on the synthesis conditions [17] [20] so is not necessarily fixed for a given zeolite.

In zeolite science, Löwenstein's rule [21] states that Al-O-Al linkages are forbidden. It is thought that this Al-O-Al avoidance rule arises at the synthesis stage where lower energy Si-O-Al rings and clusters, which form the secondary building units, are preferentially formed over their Al-O-Al counterparts [13].

Dempsey's rule [22] is sometimes applied in addition to Löwenstein's rule. This states that Al atoms will try to distribute themselves as far apart from one another as possible. The origins of Dempsey's rule likely arise from electrostatics where, at the synthesis stage, $[AlO_4]^-$ clusters repel each other [23]. This has the effect of making Al-O-Si-O-Al linkages less favourable than Al-O-Si-O-Si-O-Al linkages [24].

For simulations, Dempsey's rule is often ignored and a random Löwensteinian configuration is chosen. However, partial incorporation of Dempsey's rule can be attempted. Starting from the limiting case of Si/Al=1 where the Si and Al atoms alternate to obey Löwenstein's rule, Al-O-Si-O-Al linkages are identified at random and a terminal Al atom is exchanged for Si to form an Al-O-Si-O-Si linkage. Al-O-Si-O-Al linkages then continue to be identified and replaced until the desired Al ratio is obtained. This reduces the number of unfavourable Al-O-Si-O-Al linkages.

2.4. Computer simulation techniques

Two main simulation techniques are used in this work:

i) Monte Carlo, which is used to study the equilibrium properties of a system,

ii) Molecular Dynamics, which is used to study the time-evolution of a system.

Both techniques form an integral part of the work presented here and so the following subsections provide an introduction to the underlying statistical mechanics.

2.4.1. Monte Carlo (MC)

Monte Carlo is a stochastic tool where a low energy state is approached by doing a random walk through configurational space. In a Monte Carlo simulation a series of trial moves are proposed and either accepted or rejected based on the probability of finding the new configuration relative to the old configuration. A key principle of any Monte Carlo simulation is that as the number of iterations goes to infinity, every configuration (microstate) is examined.

For an ergodic system, i.e. a system where the final configuration is independent of the initial configuration, the average of all equilibrium microstates is identical to the macroscopic property of interest:

$$M_{observed} = \langle M_{ensemble} \rangle = \sum M_i P_i \qquad (2.5)$$

where $M_{observed}$ is the macroscopic property, $\langle M_{ensemble} \rangle$ is the average of the ensemble, M_i is the quantity of interest for microstate i and P_i is the probability of finding that microstate.

There are two ensembles used in the MC simulations in this work: the canonical (NVT) ensemble in which the number of molecules (N), the volume of the system (V) and the temperature (T) are kept constant and the grand-canonical (μVT)

ensemble in which the chemical potential (μ), volume (V) and temperature (T) are kept constant. The NVT ensemble is used when the equilibrium positions of a constant number of cations is required and the μVT ensemble is used for adsorption simulations.

2.4.1.a. The ensemble average

This section develops an expression for the ensemble average in the grand canonical ensemble based on summaries provided by Selinger [25], Shell [26] Tuckerman [27] and Frenkel & Smit [28]. A similar expression can be derived for the canonical ensemble by changing the sum over all particles to the sum from N to N molecules (i.e. a constant number of N particles).

In the grand-canonical ensemble, the chemical potential, volume and temperature are fixed and the total energy (E) and number of molecules (N) is allowed to vary. The partition function, the sum over all possible microstates with a given energy and number of particles (Ξ) is given by Equation (2.6)

$$\Xi(\mu, V, T) = \sum_{N=0}^{N=\infty} \left[\left(e^{\beta \mu N} \right) \sum_{i=0}^{i=\infty} e^{-\beta E_i} \right] \tag{2.6}$$

where the thermodynamics beta value is given by Equation (2.7) and k_B is the Boltzmann constant.

$$\beta = \frac{1}{\mathrm{k_B} T} \tag{2.7}$$

In the quantum mechanical approach above, every microstate is known and accounted for. This quickly becomes impractical to calculate for real systems and so instead, a switch to classical mechanics is made. In this approach, Equation (2.6) is integrated over all microstates to give Equation (2.8), an expression in terms of the positions $\boldsymbol{r}$ and momenta $\boldsymbol{p}$ of all particles.

$$\Xi = \sum_{N=0}^{N=\infty} \left[\left(e^{\beta \mu N} \right) \int e^{-\beta E_i} \; d^3\boldsymbol{r}_1 d^3\boldsymbol{p}_1 d^3\boldsymbol{r}_2 d^3\boldsymbol{p}_2 \dots \dots d^3\boldsymbol{r}_N d^3\boldsymbol{p}_N \right] \tag{2.8}$$

As it stands, Equation (2.8) is only partially correct and two modifications must be made.

i) The first is that the partition function is dimensionless but the expression on the RHS has units of (momentum·volume)^N. A sensible quantity to divide the RHS by is Planck's constant raised to the power 3N (i.e. for each molecule divide by an additional h in each of the three spatial directions). This also accounts for Heisenberg's uncertainty principle, which states that the position and momentum of a particle can never both be known exactly.

$$\Xi = \sum_{N=0}^{N=\infty} \left[\left(e^{\beta\mu N}\right) \cdot \frac{1}{h^{3N}} \int e^{-\beta E_i} \; d^3\boldsymbol{r}_1 d^3\boldsymbol{p}_1 d^3\boldsymbol{r}_2 d^3\boldsymbol{p}_2 \dots \dots d^3\boldsymbol{r}_N d^3\boldsymbol{p}_N \right] \tag{2.9}$$

ii) The second correction accounts for indistinguishability of the particles. If particle 1 and particle 2 can be exchanged such that the overall position and momentum of all particles the system remain unchanged, the microstates are considered identical. As there are N! identical configurations, dividing by N! prevents counting the same microstate more than once.

$$\Xi = \sum_{N=0}^{N=\infty} \left[\left(e^{\beta\mu N}\right) \frac{1}{N!\, h^{3N}} \int e^{-\beta E_i} \; d^3\boldsymbol{r}_1 d^3\boldsymbol{p}_1 d^3\boldsymbol{r}_2 d^3\boldsymbol{p}_2 \dots \dots d^3\boldsymbol{r}_N d^3\boldsymbol{p}_N \right] \tag{2.10}$$

Equation (2.10) can also be written with the total energy (E) expressed as the sum of the kinetic (E_k) and potential energy (U):

$$\Xi = \sum_{N=0}^{N=\infty} \left[\left(e^{\beta\mu N}\right) \frac{1}{N!\, h^{3N}} \int e^{[-\beta E_{k,i}]+[-\beta U]} \; d^3\boldsymbol{r}_1 d^3\boldsymbol{p}_1 d^3\boldsymbol{r}_2 d^3\boldsymbol{p}_2 \dots \dots d^3\boldsymbol{r}_N d^3\boldsymbol{p}_N \right] \tag{2.11}$$

The kinetic energy is then rewritten in terms of momentum:

$$\Xi = \sum_{N=0}^{N=\infty} \left[\left(e^{\beta\mu N}\right) \frac{1}{N!\, h^{3N}} \int e^{\left[-\beta \sum \frac{\boldsymbol{p}_i^2}{2m}\right]+[-\beta U]} \; d^3\boldsymbol{r}_1 d^3\boldsymbol{p}_1 d^3\boldsymbol{r}_2 d^3\boldsymbol{p}_2 \dots \dots d^3\boldsymbol{r}_N d^3\boldsymbol{p}_N \right] \tag{2.12}$$

This can be factorised [25] [26] [27] to give:

$$\Xi = \sum_{N=0}^{N=\infty} \left[\left(e^{\beta\mu N}\right) \frac{1}{N!\, h^{3N}} \int e^{\left[-\beta \frac{\boldsymbol{p}^2}{2m}\right]+[-\beta U]} \; d^3\boldsymbol{r}^N d^3\boldsymbol{p}^N \right] \tag{2.13}$$

The potential energy is a function of position only and the kinetic energy is a function of the momentum only so it is possible to write:

$$\Xi = \sum_{N=0}^{N=\infty} \left[\left(e^{\beta\mu N}\right) \frac{1}{N!\, h^{3N}} \int e^{\left(-\beta \frac{\boldsymbol{p}^2}{2m}\right)}\, d^3\boldsymbol{p}^N \int \left(e^{-\beta U}\right) d^3\boldsymbol{r}^N \right] \tag{2.14}$$

The momentum differential can be rewritten in spherical coordinates:

$$d^3\boldsymbol{p} = 4\pi \boldsymbol{p}^2 d\boldsymbol{p} \tag{2.15}$$

Equivalently, N sets of Equation (2.15) can be expressed as:

$$d^3\boldsymbol{p}^N = (4\pi)^N \boldsymbol{p}^{2\mathrm{N}} d\boldsymbol{p}^N \tag{2.16}$$

Substituting Equation (2.16) into (2.14) gives:

$$\Xi = \sum_{N=0}^{N=\infty} \left[\left(e^{\beta\mu N}\right) \frac{1}{N!\, h^{3N}} \int e^{\left(-\beta \frac{\boldsymbol{p}^2}{2m}\right)}\, (4\pi)^N \boldsymbol{p}^{2\mathrm{N}} d\boldsymbol{p}^N \int \left(e^{-\beta U}\right) d^3\boldsymbol{r}^N \right] \tag{2.17}$$

The first integral in Equation (2.14) is in the standard form of a Gaussian integral (albeit repeated N times):

$$\int \exp(-ax^2) x^n dx = \begin{cases} \dfrac{(n-1)!!}{2^{\frac{n}{2}+1} a^{\frac{n}{2}}} \sqrt{\dfrac{\pi}{a}} & for\ n\ is\ even \\ \dfrac{\left[\frac{1}{2}(n-1)\right]!}{2a^{\frac{n+1}{2}}} & for\ n\ is\ odd \end{cases} \tag{2.18}$$

Using Equation (2.18) to integrate Equation (2.17)

$$\int e^{\left(-\beta \frac{\boldsymbol{p}^2}{2m}\right)}\, 4\pi \boldsymbol{p}^2 d\boldsymbol{p} = \frac{4\pi}{4\left(\frac{\beta}{2m}\right)} \frac{\sqrt{\pi}}{\sqrt{\left(\frac{\beta}{2m}\right)}} = \left(\frac{2\mathrm{m}\pi}{\beta}\right)^{\frac{3}{2}} \tag{2.19}$$

N repeats gives

$$\int e^{\left(-\beta \frac{\boldsymbol{p}^2}{2m}\right)}\, (4\pi)^N \boldsymbol{p}^{2\mathrm{N}} d\boldsymbol{p}^N = \left(\frac{2\mathrm{m}\pi}{\beta}\right)^{\frac{3\mathrm{N}}{2}} \tag{2.20}$$

Substituting Equation (2.20) into Equation (2.17) gives

$$\Xi = \sum_{\mathrm{N}=0}^{\mathrm{N}=\infty} \left[\left(\mathrm{e}^{\beta\mu\mathrm{N}}\right) \frac{1}{N!\, h^{3N}} \left(\frac{2\mathrm{m}\pi}{\beta}\right)^{\frac{3\mathrm{N}}{2}} \int \left(e^{-\beta U}\right) d^3\boldsymbol{r}^N \right] \tag{2.21}$$

Equation (2.21) can be simplified further by substituting for the de Broglie wavelength, Λ.

$$\Lambda = \mathrm{h}\left(\frac{\beta}{2\mathrm{m}\pi}\right)^{\frac{1}{2}} \tag{2.22}$$

Substituting Equation (2.22) into Equation (2.21) gives Equation (2.23).

$$\Xi = \sum_{\mathrm{N}=0}^{\mathrm{N}=\infty}\left[\left(\mathrm{e}^{\beta\mu\mathrm{N}}\right)\cdot\frac{1}{\mathrm{N}!}\frac{1}{\Lambda^{3\mathrm{N}}}\int\left(e^{-\beta U}\right)d^3\boldsymbol{r}^N\right] \tag{2.23}$$

For any given property M of interest, the ensemble average is given by:

$$<\mathrm{M}>=\frac{1}{\Xi}\sum_{\mathrm{N}=0}^{\mathrm{N}=\infty}\left[\left(\mathrm{e}^{\beta\mu\mathrm{N}}\right)\cdot\frac{1}{\mathrm{N}!\,\Lambda^{3\mathrm{N}}}\int M(N,\boldsymbol{r})\left(\mathrm{e}^{-\beta\mathrm{U}}\right)d^3\boldsymbol{r}^N\right] \tag{2.24}$$

It is more common to see Equation (2.24) in the form of scaled coordinates (**s**) rather than Cartesian coordinates (**r**).

$$\mathrm{d}\mathbf{r} = \mathrm{L}\,\mathrm{d}\mathbf{s} \tag{2.25}$$

Substituting Equation (2.25) into Equation (2.24) gives Equation (2.26).

$$<\mathrm{M}>=\frac{1}{\Xi}\sum_{\mathrm{N}=0}^{\mathrm{N}=\infty}\left[\left(\mathrm{e}^{\beta\mu\mathrm{N}}\right)\cdot\frac{\mathrm{L}^{3\mathrm{N}}}{\mathrm{N}!\,\Lambda^{3\mathrm{N}}}\int M(N,\boldsymbol{r})\left(\mathrm{e}^{-\beta\mathrm{U}}\right)d^3\boldsymbol{s}^N\right] \tag{2.26}$$

From the definition for the volume of a cube ($V=L^3$), Equation (2.26) may be further simplified to Equation (2.27) to give a final expression for the ensemble average.

$$<\mathrm{M}>=\frac{1}{\Xi}\sum_{\mathrm{N}=0}^{\mathrm{N}=\infty}\left[\left(\mathrm{e}^{\beta\mu\mathrm{N}}\right)\cdot\frac{\mathrm{V}^{\mathrm{N}}}{\mathrm{N}!\,\Lambda^{3\mathrm{N}}}\int M(N,\boldsymbol{r})\left(\mathrm{e}^{-\beta\mathrm{U}}\right)d^3\boldsymbol{s}^N\right] \tag{2.27}$$

Critically, developing an expression for the ensemble average yields Equations (2.24) and (2.25) from which a classical expression can be obtained for the probability of finding any particular configuration of N particles:

$$\rho(interest) = \frac{1}{\Xi}\left(\mathrm{e}^{\beta\mu\mathrm{N}}\right)\cdot\frac{\mathrm{V}^{\mathrm{N}}}{\mathrm{N}!\,\Lambda^{3\mathrm{N}}}\,\mathrm{e}^{-\beta\mathrm{U}} \tag{2.28}$$

2.4.1.b. Importance sampling

An important feature of Monte Carlo simulation is importance sampling. This is key to moving from the initial configuration to a set of equilibrium configurations with the minimal computational effort. The importance sampling scheme employed in this work is the Metropolis scheme [29].

At the heart of the Metropolis Monte Carlo scheme are the acceptance criteria. Starting from an old configuration (o), a small change is made to the system using one of five trial moves: an insertion, a deletion, a translation, a rotation or for a multicomponent system, an identity swap. This gives a new configuration/ microstate (n). The probability of moving from the old state to the new state $\pi(o \to n)$ is the combined probability of attempting a move $\alpha(o \to n)$ and the probability of the move being accepted $acc(o \to n)$.

In the Metropolis scheme, each move must fulfil the principle of microscopic reversibility (Equation (2.29)). This relates the probability, ρ, of finding a set of particles in a given state (Equation (2.28)) with the probability of transitioning between the old and new states.

$$\rho(o)\pi(o \to n) = \rho(n)\pi(n \to o) \tag{2.29}$$

Equation (2.29) imposes an equilibrium condition which allows configurations to move towards a low energy configuration but also provides the potential to move away from a local minimum over a probability barrier and towards a new lower minimum.

As each of the moves has an equal chance of being selected in the simulations run, Equation (2.29) may be simplified to:

$$\rho(o)acc(o \to n) = \rho(n)acc(n \to o) \tag{2.30}$$

The criteria for accepting a new move is then defined as:

$$acc(o \to n) = \min\left(1, \frac{\rho(n)}{\rho(o)}\right) \tag{2.31}$$

If $\rho(n) > \rho(o)$ then the new state is lower in energy than the old state and the move is always accepted. If $\rho(n) < \rho(o)$ then the new state is higher in energy and the move is accepted only if $\frac{\rho(n)}{\rho(o)}$ is greater than a randomly generated number between 0 and 1.

Before calculating the acceptance criteria it is first helpful to express the chemical potential in Equation (2.28) in terms of the fugacity using Equation (2.32). This equation (2.32) is often presented as is [28] but can be formed by substituting Equation (2.40) into Equation (2.39).

$$\mu = \ln(f\beta\Lambda^3)/\beta \tag{2.32}$$

To calculate the acceptance criteria, Equations (2.28) and (2.32) are substituted into Equation (2.31).

For an insertion move, the acceptance rule is given by:

$$acc(o \to n) = \min\left(1, \frac{\beta f V}{N+1} e^{-\beta\left(U(N+1)-U(N)\right)}\right) \tag{2.33}$$

For a deletion move, the acceptance rule is given by:

$$acc(o \to n) = \min\left(1, \frac{N}{\beta f V} e^{-\beta\left(U(N)-U(N+1)\right)}\right) \tag{2.34}$$

For a rotation or translation move, the acceptance rule is given by:

$$acc(o \to n) = \min\left(1, e^{-\beta\left(U(new)-U(old)\right)}\right) \tag{2.35}$$

An identity swap move can be considered as the combined deletion of species A and insertion of species B:

$$acc(o \to n) = \min\left(1, \frac{f_B N_A}{f_A(N_B+1)} e^{-\beta\left(U(N+1)-U(N)\right)}\right) \tag{2.36}$$

A particular useful feature of the acceptance rules used here is that in contrast to Equation (2.27), it is not necessary to calculate the partition function (and hence know every possible microstate) in order to determine a set of equilibrium configurations.

2.4.2. Replica exchange methods

The movement of charged particles (for example cations) in a system with strong electrostatic interactions (such as a zeolite) is problematic with standard Monte Carlo moves. The energy landscape contains many deep wells and so translation moves that move the cations away from their initial location have only a small chance of being accepted at the temperature of interest (300 K).

Replica exchange is an advanced sampling tool that aims to overcome this difficulty. Instead of running Monte Carlo in a single box at one temperature, many separate Monte Carlo simulations are run together each at different temperatures. Periodically, a temperature swap move is proposed and accepted based on the criteria below:

$$acc(o \rightarrow n) = \min\left(1, e^{-\Delta\beta\Delta U}\right) \tag{2.37}$$

where $\Delta\beta$ is equal to β_2-β_1 and ΔU is equal to U_2-U_1. For the two β values, T_2>T_1.

The principle behind replica exchange is that at higher temperatures, the potential energy landscape becomes flat enough that substantial translation moves can occur. If a lower energy state is reached at a higher temperature, it is then passed back down the temperature ladder. As at higher temperatures the energy barrier to translation is reduced, this allows a more complete exploration of phase space.

Replica Exchange Monte Carlo (REMC) is comparable to a simulated annealing process in molecular dynamics. In simulated annealing, a system is heated to a high temperature and then cooled slowly. If the simulation is long enough and the rate of cooling sufficiently slow, the system can explore phase space such that, as the temperature cools, particles have just enough energy to cross any local minima but not enough energy to escape the global minimum.

2.4.3. Pressure, Fugacity, Fugacity Coefficients and the Chemical Potential in the Grand Canonical Ensemble

The grand-canonical ensemble is used in simulations to represent an open system where there is accumulation within the control volume. It is analogous to an adsorption column where an initially empty solid becomes filled with gas molecules.

In a Grand Canonical Monte Carlo (GCMC) simulation, insertion and deletion moves are attempted in addition to the regular translation moves. This simulates adsorption (or desorption) in a porous structure. The equilibrium condition is satisfied when the chemical potential of the system is equal to the chemical potential of the bulk gas (2.38) :

$$\mu_{sys} = \mu_{gas} \tag{2.38}$$

The chemical potential of a real gas (2.39) can be defined by calculating the fugacity of a gas, *f*, using an Equation of State (EoS). Fugacity is a temperature dependent quantity that can be thought of as the pressure required to model a real gas at a given temperature and density as an ideal gas [28] (i.e. fV=nRT).

$$\mu_{gas} = \mu_0 + kT \ln(\beta f) \tag{2.39}$$

The reference chemical potential [28] for an ideal gas, μ_0, is defined by:

$$\mu_0 = kT \ln(\Lambda^3) \tag{2.40}$$

The fugacity, *f*, can be calculated by finding the fugacity coefficient, ϕ, in Equation (2.41).

$$\phi = \frac{f}{P} \tag{2.41}$$

The fugacity coefficient can be calculated from a cubic EoS through the following sets of Equations [30]:

$$\ln \phi = Z - 1 \ln(Z - B) - qI \tag{2.42}$$

where Z is the compressibility factor.

$$q = \frac{a}{bRT} \tag{2.43}$$

$$B = \frac{bP}{RT} \tag{2.44}$$

$$I = \frac{1}{(\sigma_T - \varepsilon_T)} \ln\left(\frac{Z + \sigma_T B}{Z + \varepsilon_T B}\right) \tag{2.45}$$

In Equations (2.43) and (2.44), a and b represent the van der Waals parameters specific to a given gas. They can be calculated from Equations (2.46) and (2.47), where T_c and P_c correspond to the critical temperature and pressure of a gas.

$$a = \Psi\alpha \frac{R^2 T_c^2}{P_c} \tag{2.46}$$

$$b = \Omega \frac{RT_c}{P_c} \tag{2.47}$$

The σ_T and ε_T parameters in Equation (2.45) are subscripted T for thermodynamic to differentiate them from the Lennard-Jones parameters in Equation (3.6). Their values are reproduced in Table 2.3 for the Soave-Redlich-Kwong (SRK) Equation of State.

Table 2.3: Thermodynamic parameters for SRK Equation of State [30]

Equation of state	α	σ_T	ε_T	Ω	Ψ
SRK	α_{SRK}	1	0	0.08664	0.42748

The α parameter in Table 2.3 is given in terms of the acentric factor, ω, and reduced temperature, T_r, in Equation (2.48).

$$\alpha_{\mathrm{SRK}} = [1 + (0.48 + 1.574\omega - 0.176\omega^2)(1 - T_r^{0.5})]^2 \tag{2.48}$$

Finally, the compressibility factor can be found by solving the cubic equation of state for Z:

$$Z^3 - (1 - B)Z^2 + (A - 2B - 3b^2)Z - (AB - B^2 - B^3) = 0 \tag{2.49}$$

Where A is defined by (2.50) and B is defined as per (2.44)

$$A = \frac{a}{bRT}\alpha \tag{2.50}$$

With Z known, it is possible to solve Equation (2.42) for the fugacity coefficient and hence the fugacity (2.41) and chemical potential (2.39).

2.4.4. Molecular dynamics (MD)

Molecular dynamics is a technique used to study the time-evolution of a system. In MD simulations, the forces acting on each particle are calculated from the derivative of the energy (Equation (2.61)). From Newton's second law, it is then possible to calculate the acceleration of a particle and therefore over a small timestep, a velocity and new position. By repeating this cycle, a trajectory is generated which allows the dynamics of a system to be studied.

The integration algorithm used in this work, the velocity-Verlet scheme, is derived below [27] [28] [31].

The general definition of a second order Taylor series is given by Equation (2.51).

$$\mathrm{f}(x+h) = \mathrm{f}(x) + hf'(x) + \frac{h^2}{2}f''(x) \ldots \tag{2.51}$$

If the system is allowed to move forward by a small time step, δt, the new position can be expressed as:

$$\mathrm{r}(\mathrm{t}+\delta\mathrm{t}) = \mathrm{r}(\mathrm{t}) + \frac{\delta \mathrm{r}(\mathrm{t})}{\delta \mathrm{t}}\delta\mathrm{t} + \frac{1}{2}\frac{\delta^2 \mathrm{r}(\mathrm{t})}{\delta \mathrm{t}^2}\delta\mathrm{t}^2 \tag{2.52}$$

Replacing the first derivative with the velocity and substituting for acceleration using Newton's second law:

$$\mathrm{r}(\mathrm{t}+\delta\mathrm{t}) = \mathrm{r}(\mathrm{t}) + \mathrm{v}(\mathrm{t})\,\delta\mathrm{t} + \frac{1}{2}\frac{\mathrm{F}(\mathrm{t})}{\mathrm{m}}\delta\mathrm{t}^2 \tag{2.53}$$

where v is the velocity of a particle, F the force acting on the particle and m the mass of the particle.

Similarly, from a Taylor expansion for the previous location of a particle:

$$\mathrm{r}(\mathrm{t}-\delta\mathrm{t}) = \mathrm{r}(\mathrm{t}) - \mathrm{v}(\mathrm{t})\delta\mathrm{t} + \frac{1}{2}\frac{\mathrm{F}(\mathrm{t})}{\mathrm{m}}\delta\mathrm{t}^2 \tag{2.54}$$

Applying Equation (2.54) to time t = t + δt [27]

$$\mathrm{r}(\mathrm{t}) = \mathrm{r}(\mathrm{t}+\delta\mathrm{t}) - \mathrm{v}(\mathrm{t}+\delta\mathrm{t})\delta\mathrm{t} + \frac{1}{2}\frac{\mathrm{F}(\mathrm{t}+\delta\mathrm{t})}{\mathrm{m}}\delta\mathrm{t}^2 \tag{2.55}$$

Substituting Equation (2.55) into Equation (2.53)

$$r(t+\delta t) = r(t+\delta t) - v(t+\delta t)\delta t + \frac{1}{2}\frac{F(t+\delta t)}{m}\delta t^2 + v(t)\delta t + \frac{1}{2}\frac{F(t)}{m}\delta t^2 \quad (2.56)$$

Rearranging (2.56), it is possible to express the new velocity of a particle as:

$$v(t+\delta t) = v(t) + \frac{1}{2}\frac{F(t)}{m}\delta t + \frac{1}{2}\frac{F(t+\delta t)}{m}\delta t \quad (2.57)$$

Equations (2.53) and (2.57) are the velocity Verlet equations originally proposed by Swope [32] et al.

Equation (2.57) requires that the forces are stored at both the current and previous positions in order to calculate the velocity of the particles at the new position [31]. For a large system, this is an unnecessary use of computer memory. These equations are therefore manipulated further when implemented in MD packages so that only one set of positions, forces and velocities need to be stored at any one time.

Equation (2.57) can be split into two parts to give Equations (2.58) and (2.59)

$$v(t+\delta t) = \underbrace{v(t) + \frac{1}{2}\frac{F(t)}{m}\delta t} + \underbrace{\frac{1}{2}\frac{F(t+\delta t)}{m}\delta t} \quad (2.57)$$

$$v(t+\delta t) = v\left(t+\frac{1}{2}\delta t\right) + \frac{1}{2}\frac{F(t+\delta t)}{m}\delta t \quad (2.58)$$

where:

$$v\left(t+\frac{1}{2}\delta t\right) = v(t) + \frac{1}{2}\frac{F(t)}{m}\delta t \quad (2.59)$$

If equation (2.59) is multiplied by δt, Equation (2.53) can be rewritten as Equation (2.60)

$$r(t+\delta t) = r(t) + v(t)\,\delta t + \frac{1}{2}\frac{F(t)}{m}\delta t^2 \quad (2.53)$$

$$r(t+\delta t) = r(t) + v\left(t+\frac{1}{2}\delta t\right)\delta t \quad (2.60)$$

To calculate the force acting on each atom in Equations (2.58) and (2.59), the derivative of the potential energy acting on that atom is calculated.

$$\boldsymbol{F} = -\frac{dU(r)}{dr} \tag{2.61}$$

where the expression *U(r)* describes the overall potential energy arising from the sum of all pairwise interactions.

Figure 2.5 shows the scheme followed to advance an MD system forward in time using the velocity Verlet integration scheme. If the velocities of the particles at the start are unknown, then each particle is assigned a random velocity drawn from a Maxwell-Boltzmann distribution at the simulation temperature. At the same time, it is possible to calculate the forces acting on each atom using Equation (2.61). With the velocity and net force on each particle known, it is then possible to solve Equation (2.59) over a small time step δt. The new position of each particle is then calculated using Equation (2.60). Next, a new set of forces is calculated corresponding to the position of the atoms at t + δt. Finally, it is possible to calculate the velocity of each particle at t + δt. To advance to further times this loop is repeated.

In summary, the main equations are:

$$v(t + \delta t) = v\left(t + \frac{1}{2}\delta t\right) + \frac{1}{2}\frac{F(t + \delta t)}{m}\delta t \tag{2.58}$$

$$v\left(t + \frac{1}{2}\delta t\right) = v(t) + \frac{1}{2}\frac{F(t)}{m}\delta t \tag{2.59}$$

$$r(t + \delta t) = r(t) + v\left(t + \frac{1}{2}\delta t\right)\delta t \tag{2.60}$$

$$\boldsymbol{F} = -\frac{dU(r)}{dr} \tag{2.61}$$

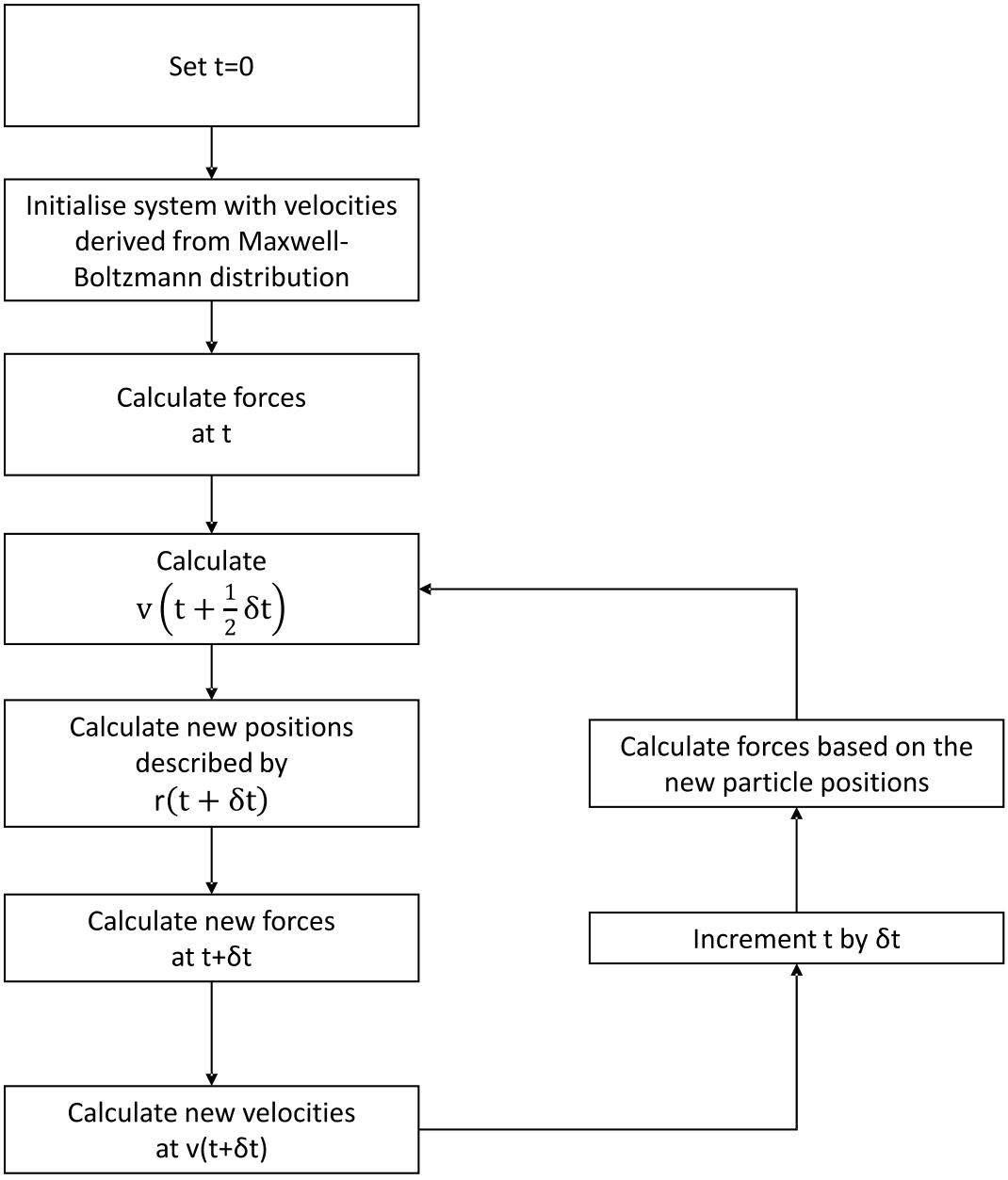

Figure 2.5: Velocity Verlet integration scheme

2.4.5. Calculation of self-diffusion coefficient

The self-diffusion coefficient describes, for an isotropic system at equilibrium, the rate of travel of a tagged particle (or particles). Under these conditions, diffusion is due to random thermal motion and there is no concentration gradient with which to measure the transport diffusivity. The diffusion of a given molecule, D, is then given by Einstein's equation [28] (2.62):

$$\frac{\delta\langle r^2(t)\rangle}{\delta t} = 2dD \tag{2.62}$$

Where d represents the dimensionality of the system (d=1 for one dimension, d=2 for two dimensions and d=3 for three dimensions).

The mean squared distance molecule has moved, $\langle r^2(t)\rangle$ is given by:

$$\langle r^2(t)\rangle = \frac{1}{N}\sum_{i=1}^{N}[(r_i(t) - r_{i0})^2] \tag{2.63}$$

Where N is the number of molecules of interest, $r_i(t)$ represents the position at time t and r_{i0} represents the original position of molecule i.

Substituting Equation (2.63) into (2.62) gives the diffusion coefficient (2.64).

$$D = \frac{1}{6N}\frac{\delta}{\delta t}\left(\left[\sum_{i=1}^{N}[(r_i(t) - r_{i0})^2]\right]\right) \tag{2.64}$$

The derivative term in (2.64) is obtained most easily by plotting the mean squared displacement (the quantity in brackets) against time to give a line with gradient 6ND.

Where it is feasible, the reliability of Equation (2.64) can be improved by calculating the diffusion coefficient for independent trajectories [33]. In this case, the overall diffusion coefficient for a 3D system is given by:

$$D = \frac{1}{6N}\langle\frac{\delta}{\delta t}\left(\left[\sum_{i=1}^{N}[(r_i(t) - r_{i0})^2]\right]\right)\rangle \tag{2.65}$$

2.5. Periodic boundary conditions

In most conceivable classical MC or MD simulations, the number of atoms modelled represents only a fraction of the molecules studied in an experimental system. The largest systems typically consist of up to a few million atoms [34] although the largest MD simulation to date contained just over 4 x 10^{12} atoms [35]. Systems of this size are by far the exception but demonstrate clearly that any simulated system will be much smaller than an experimental system (which would likely have in excess of 10^{23} atoms). With this comparatively small number of atoms, surface effects are significant and require the use of periodic boundary conditions.

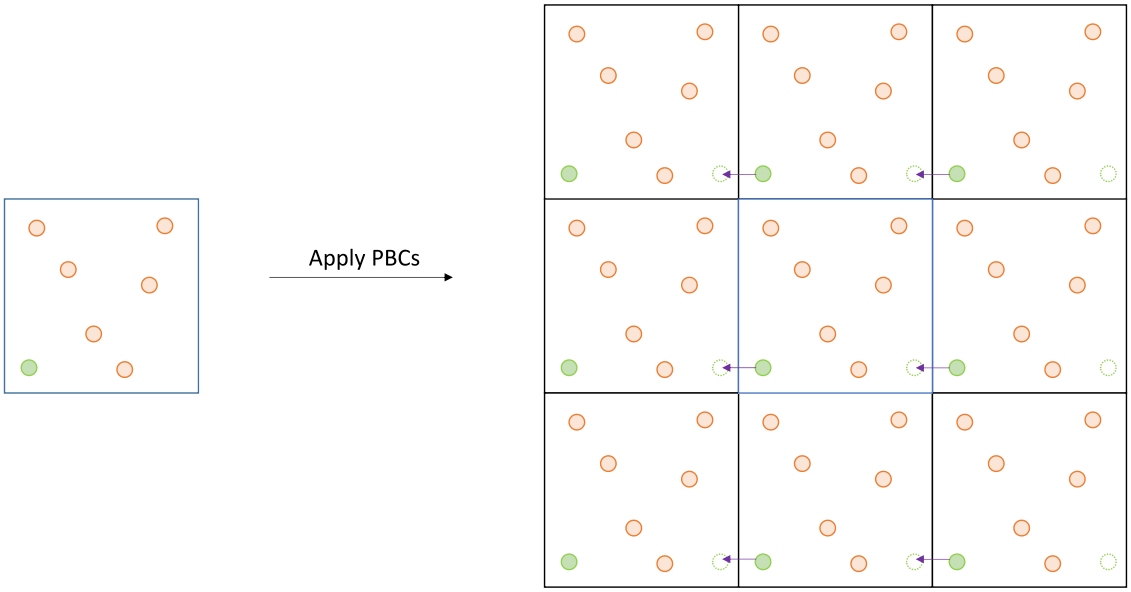

Figure 2.6: Periodic boundary conditions applied to a single unit cell

Periodic boundary conditions (Figure 2.6) work by neglecting the surface effects and simulating only the bulk phase. If the central cell is replicated in each spatial direction, an infinite lattice is formed. This gives an effect whereby an atom leaving the central box always re-enters the central box on the other side.

To avoid a situation where an atom interacts with its copy in another box, periodic boundary conditions are combined with the minimum image convention. This states that an atom can interact only with the nearest copy of other atoms and never itself. This convention is enforced by the introduction of a cut-off radius. A

cut-off radius is a truncation or shifting of the intermolecular potential such that beyond the cut-off it is assumed that the intermolecular attraction is zero. To ensure that the minimum image convention is obeyed, the cut-off must be selected so that it is less than half the size of the simulation box in the narrowest direction.

2.6. Previous work on RHO zeolite in literature

In this section, a general overview of both experimental and computational work into zeolite RHO is provided. In addition, in the main body of the thesis relevant literature is often introduced at the start of each chapter.

The structure of zeolite RHO was first predicted in 1967 [36] and first synthesised in 1973 [9]. The first structural study [9] was on H-RHO and it was later refined in a Na-Cs form [37]. The Na-Cs study [37] showed that RHO was particularly flexible, undergoing changes in unit cell length between 14.4 Å and 15.1 Å with varying hydration, temperature and cation compositions. One important finding from this study [37] was that as the unit cell decreases, the ellipticity (Δ_8 in Equation (2.1)) increases. These variations were later quantified with changes in temperature for both deuterated D-RHO and Cs-RHO [14].

Particularly interesting in early experimental work was the behaviour of RHO on adsorption of Xe [38]. For partially exchanged Cs systems, uptake of Xe with 2 cations/uc is reduced to one-third of that with 0.75 Cs^+/unit cell, despite the presence of unblocked 8MR channels. Adsorption of ethanol, propanol and pentane also reduce rapidly with increasing Cs^+ content [38].

Studies of Xe adsorption in Cd-exchanged RHO [39] [40] showed for the first time, a trapdoor effect. When Cd-RHO is heated to 300 °C, cations migrate from the 8MR to the 6MR, allowing Xe to diffuse into the structure. When the structure cools, the Cd^{2+} returns to the 8MR, trapping the Xe in the pore. Cd-RHO is therefore an example of the inclusion/entrapment phenomenon whereby the zeolite undergoes a structural change (on cooling) which prevents desorption of the adsorbed species.

The movement of Cd^{2+} from the 8MR to the 6MR produces a cell expansion from ≈14.5 Å to ≈15.0 Å. This differs from many other divalent cations (e.g. Sr^{2+}, Ca^{2+} and Ba^{2+}) which move only within the D8R unit and contract on heating [39].

A renewed interest in RHO, beyond encapsulation of Xe, came with its identification as a highly selective adsorbent for the CO_2/CH_4 separation [8] [41]. At atmospheric pressure and ambient temperature, the CO_2/CH_4 selectivity for a $Na_{7.3}Cs_{3.2}$-RHO zeolite was found to be 75 [41]. This is in stark contrast to most zeolites which rarely exceed a selectivity of 10 [41] and includes other zeolites with similarly sized pore windows such as SAPO-34 (CHA zeolite) and deca-dodecasil 3R (DDR zeolite) [41]. This enhanced selectivity was the first sign of an additional mechanism at play and led to the identification of the cation-gating phenomenon in RHO.

As well as exhibiting cation-gating, one of the advantages of zeolite RHO over other cation-exchanged zeolites is its high accessible pore volume [8]. Unlike the more commonly used zeolites A, X and Y, RHO does not contain a sodalite cage [8]. (Sodalite cages are built up of 4 and 6 secondary building units which are too small for CO_2 to diffuse through). In the case of RHO therefore, a higher proportion of the structure is accessible to CO_2. RHO also has advantages over CHA zeolite (another gating zeolite [6] [42]) in that cations are generally located in the centre of the rings rather than within the main cage. This provides a greater pore volume for adsorption of CO_2 molecules [8].

XRD measurements [8] show that in both Na-RHO and Cs-RHO, cations are present in all 8MRs. For CO_2 diffusion to occur, there must therefore be some form of cation motion (explored further in Chapter 4). In Li-RHO, cations predominantly sit in the 6MR, leaving most of the 8MRs unblocked (Chapter 6). The Li-RHO structure is also highly distorted, with a window diameter too small for CO_2 diffusion. However, CO_2 is strongly adsorbed in Li-RHO, suggesting that the windows are flexible at 298 K.

In structural studies [8] of K-RHO and Cs-RHO, the two structural phases ($I\bar{4}3m$ and $Im\bar{3}m$) introduced in Section 2.3 (Figure 2.3) were found to coexist on loading with CO_2. For K-RHO, both phases have $I\bar{4}3m$ symmetry but with independent

unit cell lengths. For Cs-RHO, the two phases can coexist independently in $I\bar{4}3m$ and $Im\bar{3}m$ symmetry. In both K-RHO and Cs-RHO, there is significant cation rearrangement on CO_2 loading. In K-RHO, 2.5 K^+ move from the 8MR to the 6MR and in Cs-RHO, the D8R cations relocate from the centre of a D8R to a S8R site on one side of the D8R unit. In Na-RHO, only the $I\bar{4}3m$ phase is found up to pressures of 9 bar and there is little cation rearrangement (see Table 3.9 in the next section for more details).

Recently, the flexible nature of mixed Li^+, Na^+ and Cs^+ systems has also been studied experimentally [43]. In the study [43], the structures of mixed cation systems were refined and the kinetics and adsorption isotherms on CO_2 loading measured. The larger ionic radius of heavier cations leads to larger unit cells (and hence larger windows) and this leads to the possibility of controlling the diffusion rate of different gases through a framework by adjusting the cation content.

The flexibility seen in RHO (phase changes, window distortion and change in unit cell length) is particularly challenging to model computationally. To date, computational studies have therefore focussed on modelling RHO with no gas present [15] [16] or where gas has been included, the framework has been held rigid [44]. An alternative has been to turn to much more computationally demanding *ab initio* methods, which describe the intermolecular interactions accurately but can only be used to look at very short timescales (tens of picoseconds) [45].

For the first time, this work applies classical simulations to fully flexible simulations of RHO zeolites with a variety of gases present. A range of cation compositions and Si/Al ratios are examined and simulations are run for extended periods (up to ≈1 μs) to study the dynamic behaviour of RHO. The effect of different force field parameters within the model are examined in detail and the limitations of the methods used are documented throughout with suggestions made for future work where appropriate.

3. **Forcefield selection and optimisation**

I would like to acknowledge the work of Dr Claire Hobday at the University of Bath for running the DFT simulations in this section and Elliott Bruce at the University of St Andrews for the practical XRD work.

3.1. Preface

This chapter begins by providing a background to forcefield approaches in molecular simulation. It then describes how the forcefield used in this work, developed by Gabrieli et al. [46], was derived. The internal flexibility seen in zeolite RHO is substantial and represents a significant challenge to represent accurately. The remaining sections in this chapter are used to assess where the limitations of the model lie and to what extent key physical properties of RHO can be reproduced.

3.2. Background

In classical forcefield simulations, the interactions between atoms are expressed by well-defined functions known as potentials (described in Section 3.4). During parameterisation of these potentials, the developer seeks to reproduce certain physical characteristics, often measured by experiment or derived through quantum mechanical simulations. These include reproducing vapour-liquid equilibrium curves [47], radial distribution functions [48], hydration energies [48], adsorption isotherms [49], elastic constants/Young's modulus [50] or bond lengths, bond angles and unit cell parameters [51].

It is not uncommon to find several forcefields that describe the same material but which have been optimised to investigate different physical properties. For zeolites, various forcefields exist in the literature. These include a core-shell model [50] [52] [53] to capture the polarizability of the oxygen atom in vibrational and structural studies of silicates and aluminosilicates (Sanders/Catlow potentials); a forcefield [54] optimised to reproduce the size of eight membered rings in pure

silica zeolites (adapted Hill-Sauer force field); and another to study adsorption and diffusion in LTA, FAU and MFI [55].

When choosing a forcefield, the purpose for which it was developed is therefore an important consideration. To study the diffusion of small gas molecules through zeolite RHO and gain some insight into the trapdoor behaviour, the key physical properties of interest are:

a) Reproduction of the correct crystallographic phase (centric or acentric) to capture the internal framework structure correctly
b) Reproduction of experimental unit cell lengths to ensure that the zeolite windows are the correct size
c) Siting of the cations to capture the correct cation-framework interactions
d) On adsorption of CO_2, a match to the experimental CO_2 isotherm and cell expansion to capture the correct gas-framework interactions.

Preliminary investigations into the most suitable for forcefield indicated that the most promising force field for this work was that by Gabrieli et al [46].

3.3. Overview of CO_2 model used for testing

To study cation gating, it is important to have a suitable model for CO_2 as well as the zeolite. Table 3.1 gives the non-bonded parameters [56] [57] used to describe the CO_2-CO_2 and CO_2-zeolite interactions. These are very similar to the Elementary Physical Model (EPM2) model from Harris and Yung [58] and those developed explicitly to model uptake of CO_2 in LTA zeolite [59]. They are also similar to the TraPPE forcefield parameterisation [60]. The advantage of the model chosen is the fully flexible parameters used to describe the internal CO_2 bond bending and bond stretching (Table 3.2). In particular, the Urey-Bradley bond stretch keeps the molecule stable [61] at an angle of 180° where, as a result of the algorithms used within most MD codes, fluctuations in the angle-bend forces can lead to instabilities [62]. The Urey-Bradley stretch also improves the behaviour of the O-O interaction. This is weakly coupled to the angle oscillations and so is best modelled with both a bond stretching and bond bending term [46].

Table 3.1: CO_2 Lennard-Jones parameters and atomic charges

atom	sigma (Å)	Epsilon (kcal/mol)	Charge (e^-)
C	2.757	0.05584	0.6512
O	3.033	0.15982	-0.3256

Table 3.2: CO_2 bond stretching and bond bending parameters

Bond stretch	bond length (Å)	k_r (kcal/mol/Å^2)	Use with equation
C-O	1.178	979.46	(3.3)

Bond Bend	Equilibrium angle (degrees)	k_θ (kcal/mol/rad^2)	Use with equation
O-C-O	180	52.76	(3.4)

Urey Bradley	bond length (Å)	k_{UB} (kcal/mol/Å^2)	Use with equation
O-(C)-O	2.353	86.77	(3.3)

3.4. Overview of forcefield used to describe the zeolite

3.4.1. Functional form of forcefield

The Gabrieli et al. forcefield [46] is a replacement to an earlier forcefield developed within the same group [63]. The new forcefield [46] is based on a CHARMM [64] functional form[3] and includes terms to describe both bonded and non-bonded interactions:

$$\mathrm{U(r)} = \mathrm{U_{coul}} + \mathrm{U_{bond}} + \mathrm{U_{bend}} + \mathrm{U_{UB}} + \mathrm{U_{VdW}} \tag{3.1}$$

The forcefield includes Coulombic interactions between charged atoms (U_{Coul}), bond stretching between atoms which are 1-2 connected (U_{bond}), bond bending between atoms which are 1-3 connected (U_{bend}), Urey-Bradley bond stretching between atoms which are 1-3 connected (U_{UB}) and van der Waals interactions (U_{VdW}).

$$\mathrm{U_{Coul}} = k_{Coul}\frac{Q_1 \mathrm{Q_2}}{\mathrm{r}} \tag{3.2}$$

where k_{Coul} is Coulomb's constant ($k_{Coul} = 1$ in atomic units), Q_1 and Q_2 are charges on atom 1 and atom 2 and r is the interatomic separation.

$$\mathrm{U_{bond}} = \frac{1}{2}\mathrm{k_r}(\mathrm{r} - \mathrm{r_0})^2 \tag{3.3}$$

where k_r is the stretching spring constant, r is the instantaneous interatomic separation and r_0 is the equilibrium interatomic separation.

$$\mathrm{U_{bend}} = \frac{1}{2}\mathrm{k_\theta}(\theta - \theta_0)^2 \tag{3.4}$$

where k_θ is the bending spring constant, r is the instantaneous angle between atoms 1, 2 and 3 and θ_0 is the equilibrium angle.

[3] The CHARMM [54] forcefield does not include the 1/2 factor shown in Equations (3.3), (3.4) and (3.5) but GULP [55], DLPOLY4 [56] and GROMACS [51] do. The spring constants used are doubled accordingly when implemented in these MD packages.

$$U_{UB} = \frac{1}{2} k_{UB}(u - u_0)^2 \tag{3.5}$$

where k_{UB} is the stretching spring constant formed by a fictional 1-3 bond, u is the instantaneous interatomic separation between atom 1 and atom 3 and u_0 is the equilibrium value.

$$U_{VdW} = 4\varepsilon\left[\left(\frac{\sigma}{r}\right)^{12} - \left(\frac{\sigma}{r}\right)^{6}\right] \tag{3.6}$$

where ε is the depth of the potential energy well, σ is the collision diameter between two atoms and r is the internuclear separation.

3.4.2. Development of Gabrieli et al. [46] forcefield

To derive the forcefield, the developers [46] initially set all values equal to those of the earlier Demontis forcefield [63] and then reoptimised in stages. First, the bond lengths and atomic angles were adjusted to reproduce the structure of zeolite NaA, with high spring constants used to prevent crystal collapse. The force constants were then reduced trying to match the potential energies of the original Demontis forcefield.

All Coulombic and van der Waals (Lennard-Jones) interactions on bond stretches (1-2 interactions) and bond bends (1-3 interactions) are excluded. For 1-4 interactions, the van der Waals interactions are left unscaled but the Coulombic interactions are reduced by a factor that has to be found through trial and error. For the LTA and MFI systems studied by the developers [46], a factor of 50% was used.

$$U_{Coul\,(1-4),reduced} = (1 - k_{scale})U_{Coul(1-4)} \tag{3.7}$$

Implementation of Equation (3.7) varies in different software packages. For GULP [65], the value k_{scale} is specified but in DLPOLY [66] and GROMACS [61], the value (1-k_{scale}) is used. In this work, the value k_{scale} is reported throughout.

The Coulombic charges on the atoms were obtained from the variation in the total dipole fluctuation (TDF) seen within an NVT MD simulation run in the CP2k [67] package. To simplify the problem, cations are given a +1 charge and oxygen atoms a -1 charge. A least squares optimisation is then performed using the InfiniCharges [68] program to give the charge of the silicon and aluminium atoms (Table 3.3).

Table 3.3: Charges on five zeolite structures given by Gabrieli et al. [46]

	NaA	NaY	NaX	CaA	Silicalite
Si	1.85	1.89	1.76	1.85	2
Al	1.27	1.274	1.288	1.27	0
M^+	1	1	1	2	0
O	-1.03	-1.001	-1.001	-1.03	-1
Si/Al	1	2.43	1.18	3	Infinite

With an initial set of forcefield parameters now derived, Gabrieli et al. [46] optimised the forcefield more rigorously to reproduce IR spectra of MFI silicalite, LTA type zeolites (Na A and Ca A) and FAU type zeolites (Na Y and Na X). This included fitting of new Urey-Bradley bond stretches between 1-3 neighbours. The bonded parameters are summarised

Table 3.4: Published bonded forcefield parameters in the Gabrieli et al. [46] forcefield

Bond	DFT (Å)	Spring constant (kcal/mol/Å^2)	Use* with equation
Si-O	1.61	300	(3.3)
Al-O	1.73	222	(3.3)
Si-Si (Urey-Bradley)	3.12	30	(3.5)
Si-Al (Urey-Bradley)	3.18	30	(3.5)
Bend	**DFT (degrees)**	**Spring constant (kcal/mol/rad^2)**	**Source**
O-Si-O	109.5	75	(3.4)
O-Al-O	109.5	65	(3.4)
Si-O-Si	149.5	30	(3.4)
Si-O-Al	149.5	30	(3.4)

*The bonded parameters given here refer to the combined k/2 spring constant i.e. the full coefficient in front of the harmonic term. It is important to check that this is consistent with the implementation in the MD package used (e.g. for GROMACS, these terms must be doubled).

3.5. Validation of model

To test the forcefield, results are compared against experimental data [7] [8] for Na-RHO (Si/Al = 3.9). A 2 x 2 x 2 supercell is set up starting from the experimental structure [7]. In a simulated unit cell of finite size, the Si/Al ratio available is discretised. In the case of the supercell above, a Si/Al ratio of 3.92 is achievable if 78 silicon atoms are swapped for aluminium atoms.

3.5.1. Charges used to model RHO (Si/Al = 3.92)

As the charges in Table 3.3 do not vary greatly, a reasonable approximation of the correct charge can be obtained from interpolation of the charge on the Si atom based on the number of cations/aluminium atoms in a RHO supercell (Figure 3.1). Theoretically, either the charge on the aluminium or the silicon could be calculated from a line of best fit. However, the charge on the aluminium is generally less sensitive than the charge on the silicon so to obtain reliable results, it is preferable to do the interpolation based on the silicon.

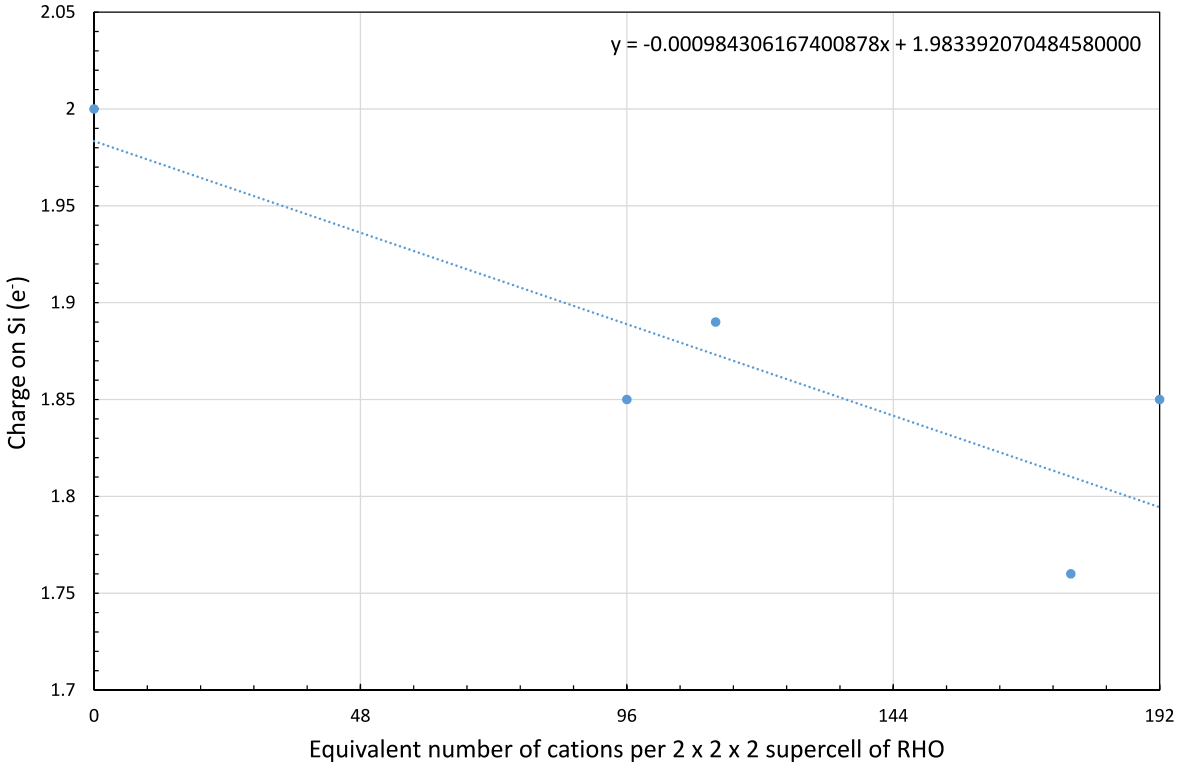

Figure 3.1: Variation of charge on Si atoms with increasing cation number (decimal places shown are needed to ensure charge balance within MD simulations). Line of best fit shows interpolated values used for simulations (other than for the case of no cations where the charge on the silicon is taken as +2).

The charge on the aluminium atoms is then calculated from a charge balance:

$$Q_{Al} = \frac{Q_{Na}N_{Na} + Q_{Si}N_{Si} + Q_O N_O}{N_{Al}} \quad (3.8)$$

where Q_i is the charge on atom i and N_i is the number of atoms of species i.

In the original paper [46], a 50% scale factor is applied to the Coulombic 1-4 interactions, leaving the van der Waals 1-4 interactions unchanged. This differs from the typical CHARMM [54] implementation where the van der Waals interactions are divided by a factor of 1.2 ($k_{scale(VdW)} = 0.8$) and the Coulombic interactions are divided by 2 ($k_{scale} = 0.5$). For zeolite RHO, a reduction to the Coulombic 1-4 interaction between 30% and 40% is found to be most appropriate (Table 3.5).

3.5.2. Choice of exclusion policy and Lennard-Jones parameters

One aim of this work is to study mixed Li/Na systems. However, no Li^+ parameters were derived for use with the force field [46]. Ideally, a consistent Coulombic scale factor would be used across Li-RHO, Na-RHO and mixed Li/Na-RHO systems. To this end, a variety of Na^+ parameters are trialled to find a compatible pair of Li^+ and Na^+ interactions. Comparing the adsorption isotherms and unit cell parameters obtained with different Na^+ parameters also allows a search through parameter space to yield a good match with experimental data.

Reproduction of the framework-framework interactions is of particular interest in this study due to the flexibility of the structure (the size and shape of the windows). Realistic modelling of the baseline behaviour of the framework structure, without gas present, is particularly important as the underlying framework behaviour controls the dimensions of the 8MRs (the phase of the material) when gas is loaded. In addition, for intercage CO_2 diffusion to occur a molecule must cross the D8R. The limiting window dimension/distortion of the 8MR will therefore effect the gas diffusivity.

The unit cell length is correlated strongly with the distortion of the ring. At 14.2 Å the rings are strongly acentric and by 14.9 Å, the rings are fully centric. When samples of Li-RHO, Na-RHO and Cs-RHO are refined experimentally at 298 K, the unit cell lengths are found to be 14.24 Å, 14.41 Å and 14.62 Å respectively [7] [8]. The unit cell length is also sensitive to temperature with XRD experiments of a NaCs-RHO system showing that the unit cell length increases by approximately 0.05 Å per 100 K [14].

The narrow range in unit cell length over which the transition between centric and acentric phases occurs, combined with the increase in unit cell length seen with higher temperature and heavier group 1 cations requires careful calibration of the forcefield to ensure accurate modelling. Difficulties in modelling Na-RHO are compounded by the expansion in unit cell length from 14.4 Å to 14.6 Å on CO_2 loading.

In any NPT simulation, the volume fluctuates. In the simulations presented here, a 2 x 2 x 2 supercell is used and the cell is constrained so that it remains cubic. Typical oscillations in the length of a single unit cell are ±0.05 Å. This represents the limit to which it is possible to know the unit cell length without moving to a larger supercell (where the deviations per unit cell would be smaller).

Table 3.5 gives the average unit cell size from an NPT molecular dynamics simulation with the Coulombic scale factor that reproduces the experimental unit cell to within an accuracy of ±0.05 Å.

Table 3.5: Lennard-Jones parameters tested in NPT simulations for this work and their corresponding k_{scale} value. For the parameters by Garcia-Sanchez et al.[69], Na^+ parameters are derived from the Na-C and Na-O interactions with CO_2, assuming the Lorentz-Berthelot mixing rules in Equation (3.11) and (3.12)

Source of parameters	sigma	epsilon/k_B	k_{scale}	unit cell average over final 400 ps (600 ps - 1000 ps)	standard deviation
(-)	(Å)	(K)	(-)	(Å)	(Å)
Akten et al. [49]	2.85	8	0.37	14.42	0.02
Aqvist et al. [48]	1.83	13.25	0.34	14.36	0.02
Beerdsen et al. [70]	2.33	46.8	0.37	14.37	0.02
CVFF [71]	1.90	808.8	0.38	14.42	0.02
Cygan et al. [72]	2.35	65.47	0.37	14.37	0.01
Gabrieli et al. [46]	2.43	80.01	0.37	14.41	0.01
DREIDING [73]	2.80	251.6	0.34	14.41	0.01
Garcia-Sanchez et al. (based on $\underline{C}O_2$) [69]	3.90	4385	0.37	14.40	0.01
Garcia-Sanchez et al. (based on $C\underline{O}_2$) [69]	2.50	470.8	0.35	14.39	0.01
Halicioğlu et al. [74]	3.475	1600	0.33	14.44	0.01
Jaramillo et al. [75]	3.20	19.99	0.35	14.43	0.01
Jeffroy et al. [55]	2.59	50.27	0.37	14.43	0.01
Jensen et al. [76]	4.07	0.25	0.36	14.43	0.01
Jensen et al. [76]	3.33	1.39	0.37	14.44	0.02
Lamoureux et al. [77]	2.58	15.86	0.37	14.40	0.02
Larentzos et al. [78]	2.876	62.74	0.35	14.39	0.01
Lee et al. [79]	2.47	442.3	0.36	14.42	0.01
Maurin et al. [80]	1.75	50.36	0.35	14.42	0.02
Rao et al. [81]	1.28	5.03	0.33	14.43	0.02
UFF [47]	2.66	15.1	0.37	14.42	0.02
Vujic et al. [82]	3.23	234.13	0.33	14.41	0.01
Watanabe et al. [83]	1.746	20.63	0.345	14.40	0.02

Figure 3.2 shows the importance of the calibration step to determine the scale factor. Relatively small changes in the 1-4 scale factor, give rise to substantial changes in the unit cell length, particularly in the region of interest (14.41 Å) [7].

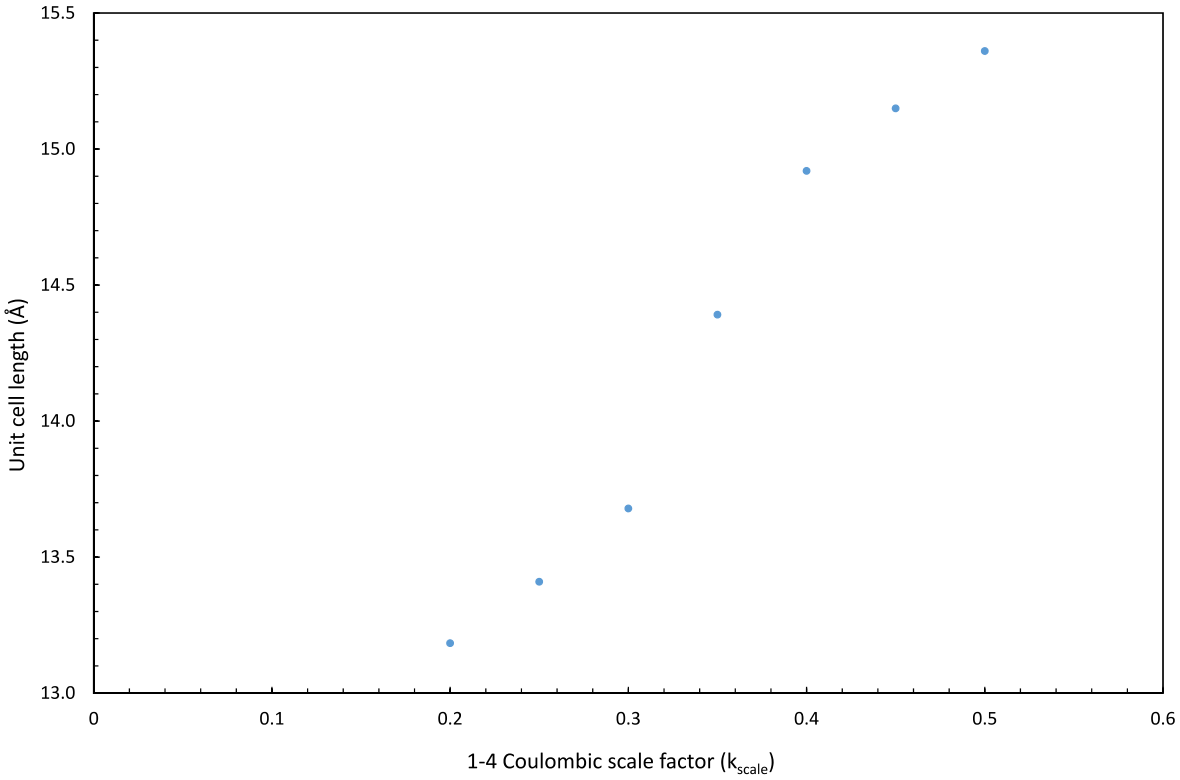

Figure 3.2: Variation of the unit cell parameter with the Coulombic scale factor using the parameters from Maurin et al. [80]

3.5.3. Effect of adsorbed CO_2

As the scale factor can be adjusted to reproduce the cell length of Na-RHO, this does not provide a criterion for evaluating the different cation parameters. To filter further the cation parameters in Table 3.5, the parameters were tested by adsorption with CO_2. Here, two factors are important:

i) the agreement in amount of CO_2 adsorbed between experimental and simulated results,
ii) the expansion of the unit cell with loading.

To simulate the amount of CO_2 adsorbed, GCMC simulations are run with equally weighted CO_2 insertion/deletion and translation moves. In the GCMC simulation, the framework is held rigid but here this is a poor assumption as the unit cell is known to expand on loading with CO_2 [7]. The iterative cycle shown in Figure 3.3 and outlined below is therefore used to allow the unit cell to respond to the presence of CO_2 molecules.

In a standard, rigid GCMC simulation, the cell is loaded with CO_2 until equilibrium is reached. The framework is then allowed to relax, first under NVT conditions to minimise the forces between molecules and then under NPT to allow the cell to expand. Once equilibrium has been reached, the structure then undergoes another GCMC step. This process is repeated until there is no appreciable change in the average amount adsorbed.

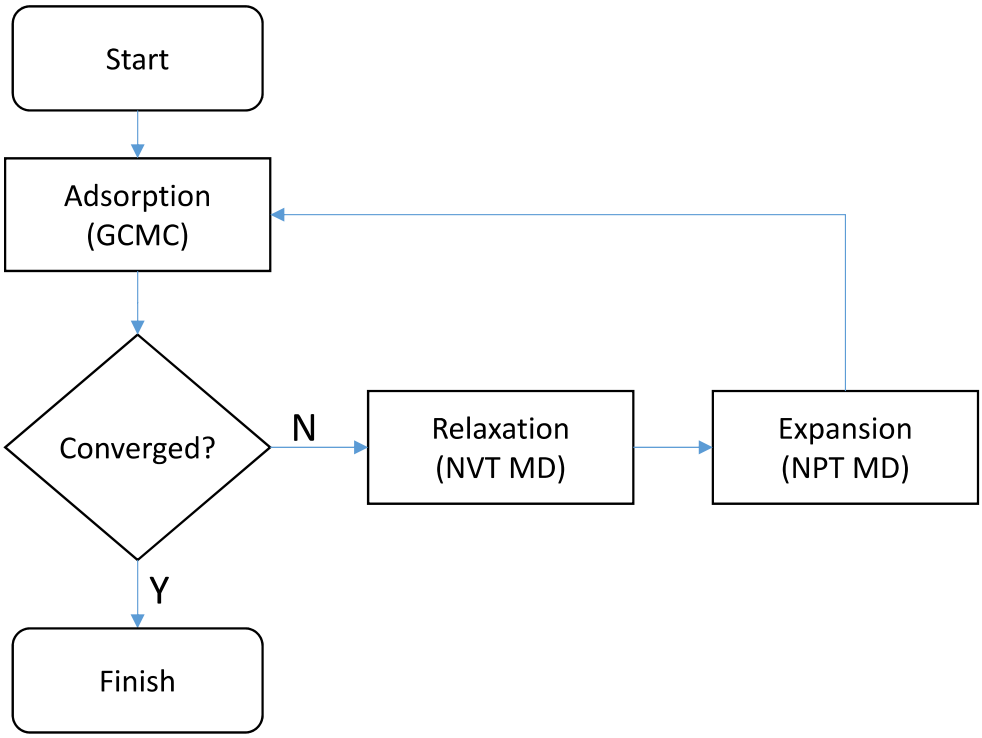

Figure 3.3: MC/MD cycle convergence diagram

To compare quantitatively the effect of the different sodium parameters, the mean square error (MSE) between experimental ($y_{i,exp}$) and simulated values ($y_{i,sim}$) is calculated for both the amount of CO_2 adsorbed and the unit cell length. This leads to a ranking that can be used to identify the most promising sets of LJ parameters.

$$\mathrm{MSE} = \frac{1}{\mathrm{N}}\sum_{i=1}^{i=N}\left(y_{i,sim} - y_{i,exp}\right)^2 \tag{3.9}$$

For the two quantities, each parameter is assigned a rank where the smallest deviation from experimental results is given a rank of 1 and the highest deviation a rank of 22.

For the expansion in unit cell length on CO_2 loading, the LJ parameters are ranked against the experimental data points in Table 3.6.

Table 3.6: Experimental measurements of unit cell expansion in Na-RHO on loading with CO_2 [7] at 298 K

Pressure (bar)	Unit cell length (Å)
0.045	14.6219
0.1	14.62823
0.2	14.6348
1	14.6513

For the amount of CO_2 adsorbed, LJ parameters are ranked against the experimental data points in Table 3.7.

Table 3.7: Experimental data points for CO_2 adsorption at 298 K, along with the equivalent loading in a 2 x 2 x 2 supercell [7]

Pressure (Pa)	Pressure (bar)	CO_2 loading (mmol/g)	CO_2 loading (N/supercell)
5262.4	0.05	3.35	83
10226.4	0.1	3.75	93
20024.3	0.2	4.13	103
39914.5	0.4	4.49	112
59914.2	0.6	4.69	116
99879.4	1.0	4.93	122
149848.0	1.5	5.12	127
199837.0	2.0	5.26	131
299856.3	3.0	5.45	135
399841.3	4.0	5.6	139
499771.5	5.0	5.71	142
599715.4	6.0	5.8	144
699899.0	7.0	5.89	146
799733.3	8.0	5.96	148
898684.5	9.0	6.03	150

The most promising parameters identified by the ranking process are those from Maurin et al. [80] and these results are summarised below. The full ranking is given in Table 3.8.

It should be noted that although the parameters by Rao et al. [81] rank highest, the simulated points cross the experimental isotherm, whereas those by Maurin et al. [80] do not. The parameters by Maurin et al. [80] therefore represent a better fit.

Table 3.8: Ranking of parameters after 3 rounds of MC/MD

Forcefield	Cell dimension		Amount adsorbed		Sum of Ranks	Rank of Ranks
	MSE	Rank	MSE	Rank		
	$Å^2$	-	$(mmol/g)^2$	-	-	-
Rao et al. [81]	0.09	6	1	3	9	1
Maurin et al. [80]	0.02	1	8	9	10	2
UFF [47]	0.08	5	2	5	10	3
Akten et al. [49]	0.05	3	7	8	11	4
Jensen-prior et al. [76]	0.04	2	18	11	13	5
Aqvist et al. [48]	0.12	9	2	4	13	6
Lamoureux et al. [77]	0.16	14	0	1	15	7
Watanabe et al. [83]	0.14	11	3	6	17	8
Beerdsen et al. [70]	0.18	15	1	2	17	9
Cygan et al. [72]	0.15	12	5	7	19	10
Demontis et al. [63]	0.11	8	20	12	20	11
Jeffroy et al. [55]	0.13	10	27	13	23	12
Vujic et al. [82]	0.10	7	36	17	24	13
Garcia-Sanchez et al. ($C\underline{C}O_2$ [69])	0.08	4	99	21	25	14
CVFF [71]	0.21	21	8	10	31	15
Jensen et al. [76]	0.15	13	75	19	32	16
Lee et al. [79]	0.18	17	32	16	33	17
DREIDING [73]	0.19	19	32	15	34	18
Jaramillo et al. [75]	0.18	16	85	20	36	19
Garcia-Sanchez et al. ($C\underline{O}_2$) [69]	0.21	22	28	14	36	20
Larentzos et al. [78]	0.20	20	65	18	38	21
Halicioğlu et al. [74]	0.19	18	116	22	40	22

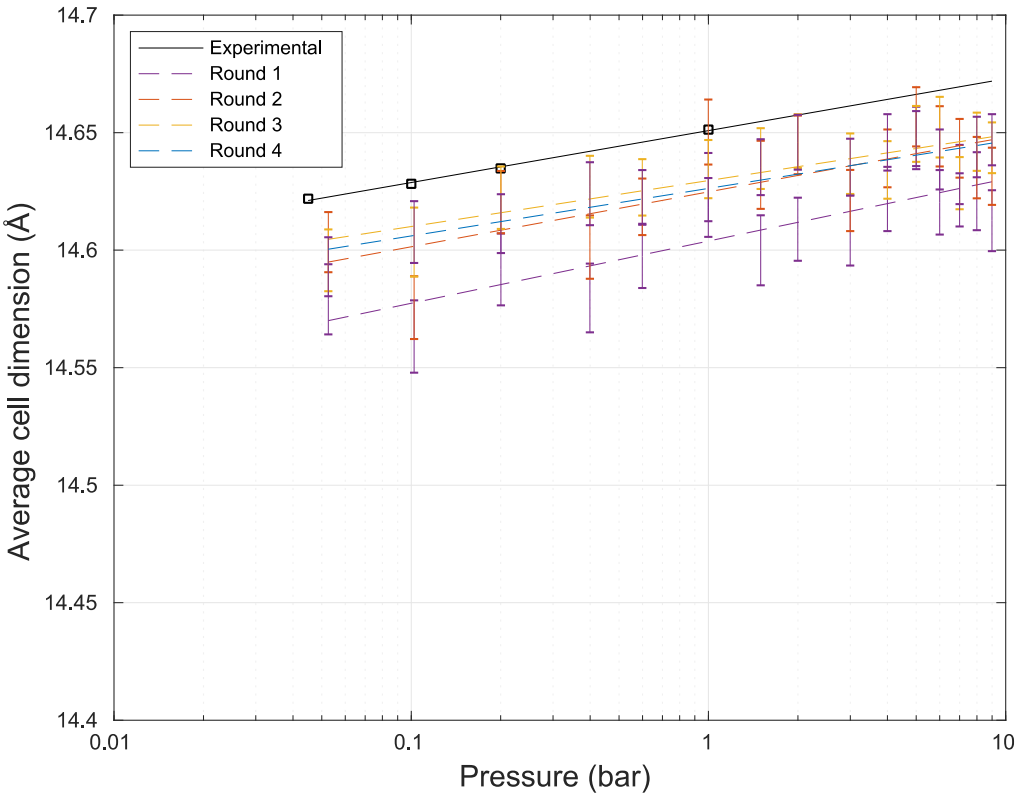

Figure 3.4: Expansion of Na-RHO with CO_2 loading at 298 K with parameters by Maurin et al. [80] Each line corresponds to the average unit cell length measured over the final 400 ps at the NPT stage in Figure 3.3

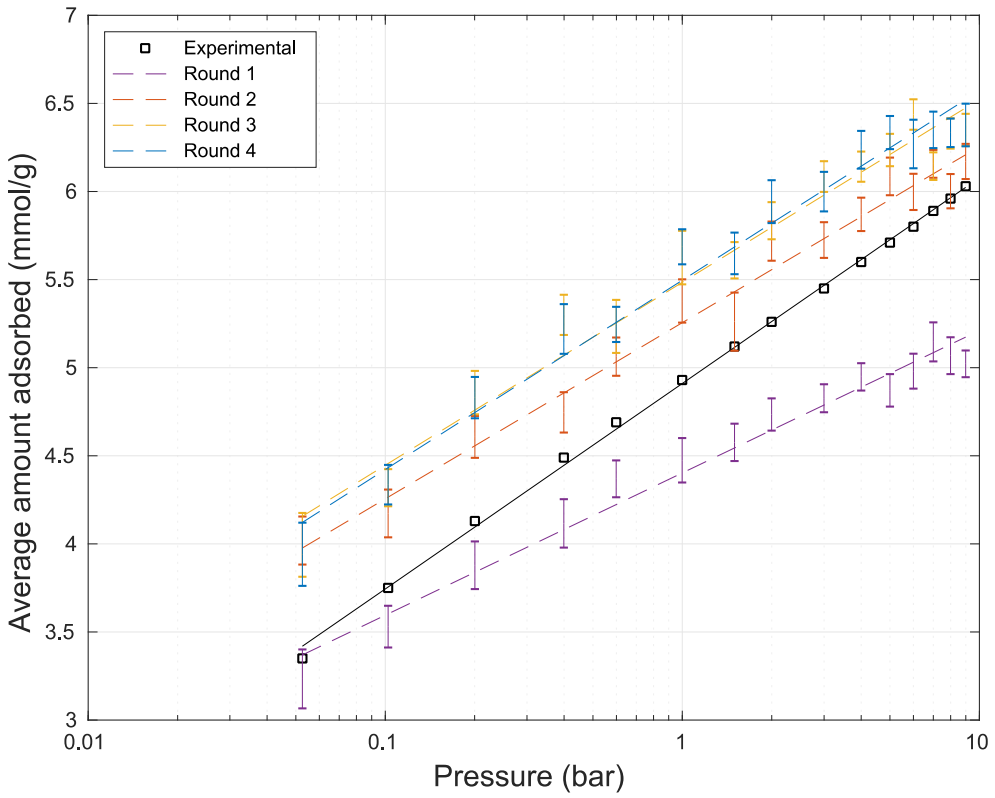

Figure 3.5: Simulated vs experimental isotherms for CO_2 at 298 K for parameters by Maurin et al. [80] (Round 1-4)

Figure 3.4 shows the average unit cell dimension from the final NPT MD cycle. This matches the experimental values to a high degree of accuracy (within ±0.02 Å). Critically, Figure 3.4 shows the importance of running both MC and MD in the cycle proposed in Figure 3.3 in order to obtain the final adsorption isotherm (Figure 3.5).

Figure 3.5 shows that whilst the amount of CO_2 is overpredicted by +0.5 mmol/g, the general trend is matched well with the overprediction consistent across the whole pressure range. The overlapping results between Rounds 3 and 4, show that convergence has been reached.

It should be noted that although neither the cell dimension nor amount of CO_2 adsorbed are matched perfectly, the parameters by Maurin et al. [80] do represent a reasonable compromise between accurate modelling of both the experimental unit cell length and the amount of CO_2 adsorbed.

3.6. Reproduction of experimental sitings

As described in Section 2.4.2, it is difficult to sample the energy landscape without taking account of the deep energy wells. Figure 3.6 shows the sampling observed with and without replica exchange at 300 K. The figure was produced by splitting the 2 x 2 x 2 supercell into cubelets of 0.1988 Å (145 x 145 x 145 cubelets along a cell dimension of 28.8278 Å). Each cubelet is then shaded yellow if it is occupied in any one of the frames output every 100,000 iterations in a 40 million iteration MC simulation. The slight orange background is an interpolation effect between occupied yellow cells and unoccupied clear cells.

At 300 K (Figure 3.6L), sampling is very poor and the cation accesses only the region of space in which it was initially placed. With replica exchange however, a greater degree of exploration is possible (Figure 3.6R).

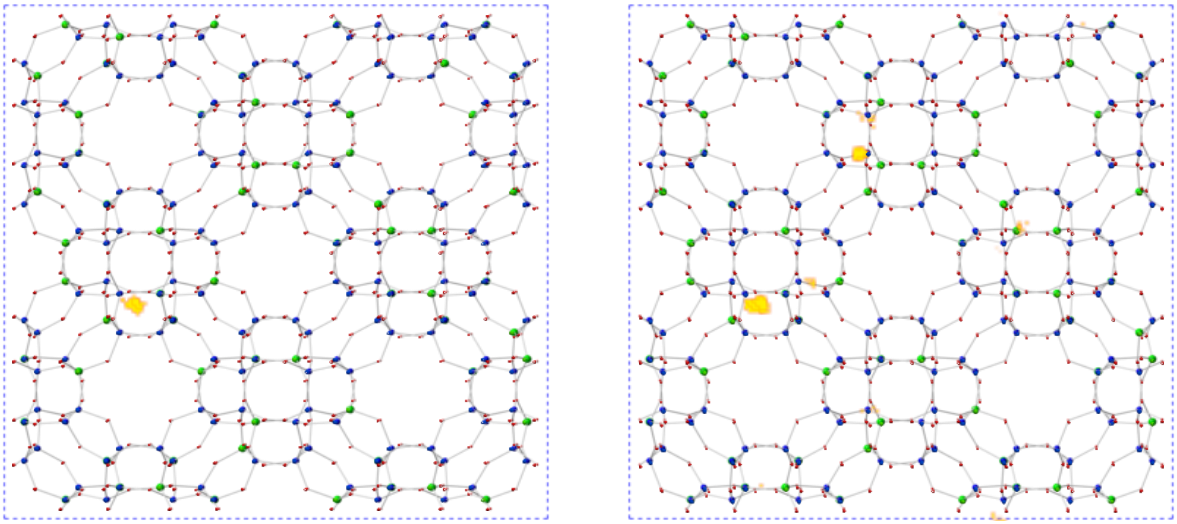

Figure 3.6: Trajectory of a single cation without (L) and with (R) replica exchange Monte Carlo. The 77 other Na^+ cations in the systems are hidden for clarity.

The experimental cation sitings for Na-RHO (Si/Al = 3.9) are summarised in Table 3.9.

Table 3.9: Na-RHO (Si/Al = 3.9) XRD measurements of cation sitings at 298 K

Sample	cations per unit cell	cations per unit cell
	Site II (S8R)	Site III (S6R)
Na-RHO (2014) [7]	6.08	3.46
Na-RHO (2012) [8]	6.47	2.98

Following a MC replica-exchange simulation consisting of 35 million moves, the positions of all atoms are allowed to relax in an MD simulation at 300 K (Figure 3.7). This gives an occupancy of 6.9 cations in the S8R and 2.9 cations in the 6MR. This contrasts markedly from the initial configuration (the output from the MC simulation) and emphasises the need for framework relaxation.

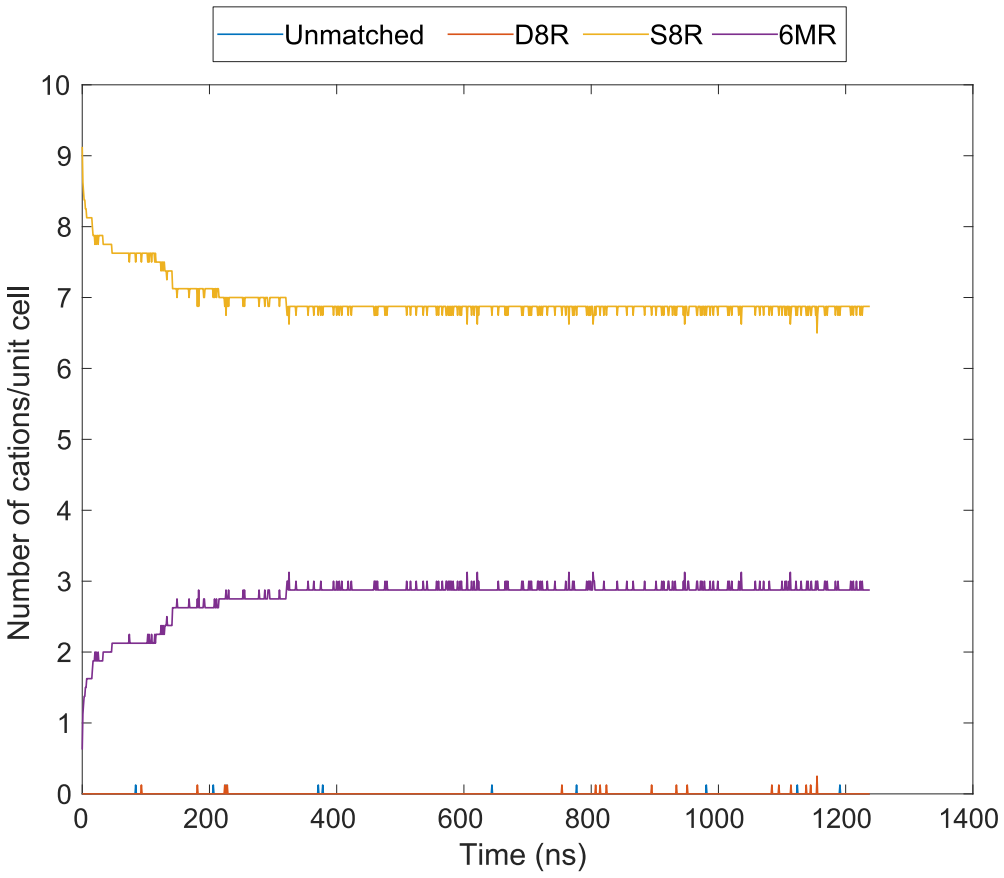

Figure 3.7: Cation positions as function of time from a long NVT MD run of Na-RHO at 300 K.

Figure 3.7 shows a good match with the experimental siting of the cations. It is important to note that long time scales are required to ensure that equilibrium has been reached (>0.5 μs). A simulation run for only 100 ns would appear to have converged when looking at the sitings only. Having to run simulations for timescales on the order of microseconds in order to obtain convergence is highly unusual and points again towards distinct states separated by high energy barriers.

In an attempt to reach equilibrium faster, a replica exchange molecular dynamics approach was used. At higher temperatures, the cations are able to move more freely and so should reach their equilibrium positions more quickly. A simulation was set up so that 16 configurations between 300 and 1200 K (in 100 K increments) were allowed to freely exchange with neighbouring temperature boxes.

This quickly showed a reversal of the expected result (Figure 3.8): 7.1 cations in the 6MR and 2.6 cations in the 8MR. Long MD simulations at temperatures above 300 K showed the same, unexpected distribution of cations.

When these simulations are relaxed back to 300 K, the cations remain in the same position but with a lower energy. This indicates that the 300 K results seen in Figure 3.7 are in a metastable state. At room temperature, there is not enough energy for the system to jump the barriers required to relax fully and so the cations remain trapped in a local energy minimum. Similar results are observed in high temperature MD simulations without replica exchange. When the simulated temperature is raised to 1000 K (Figure 3.9), the cations move quickly to their low energy sites. The disadvantage here is that the simulation box represents a higher temperature where the framework becomes centric. In REMD, the temperature of each box is controlled and the simulation box of interest still corresponds to the correct temperature.

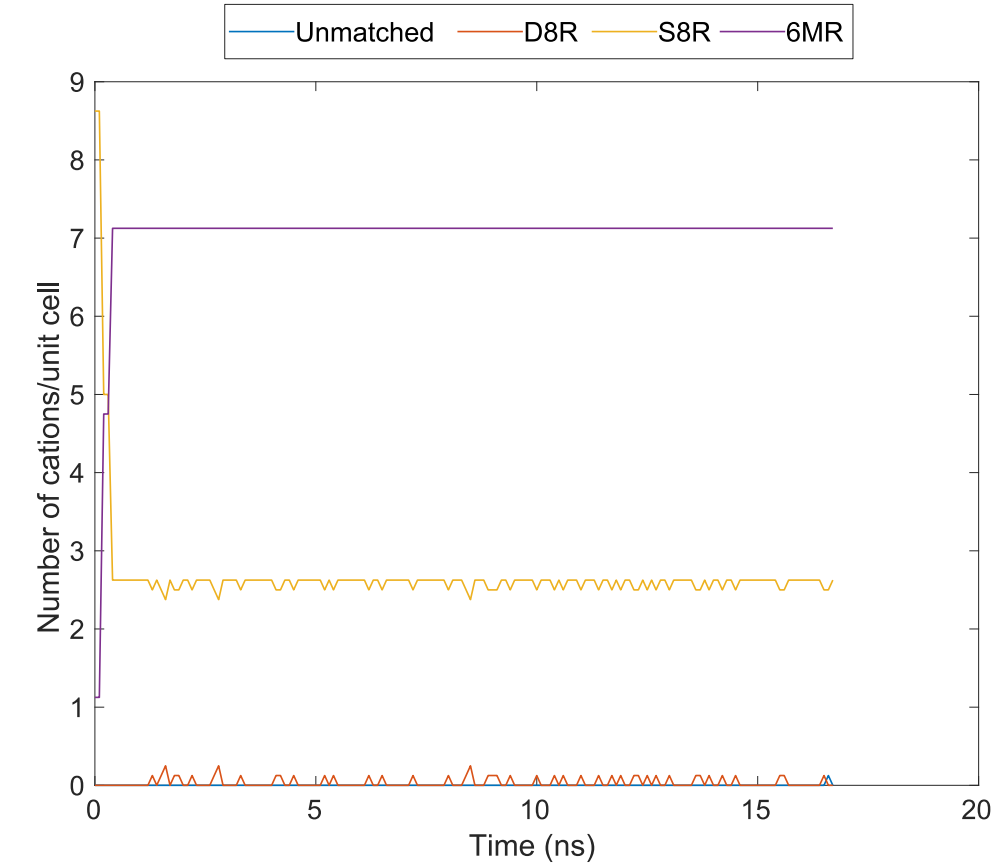

Figure 3.8: Cation distribution during Replica Exchange MD (300 K box) for Na-RHO

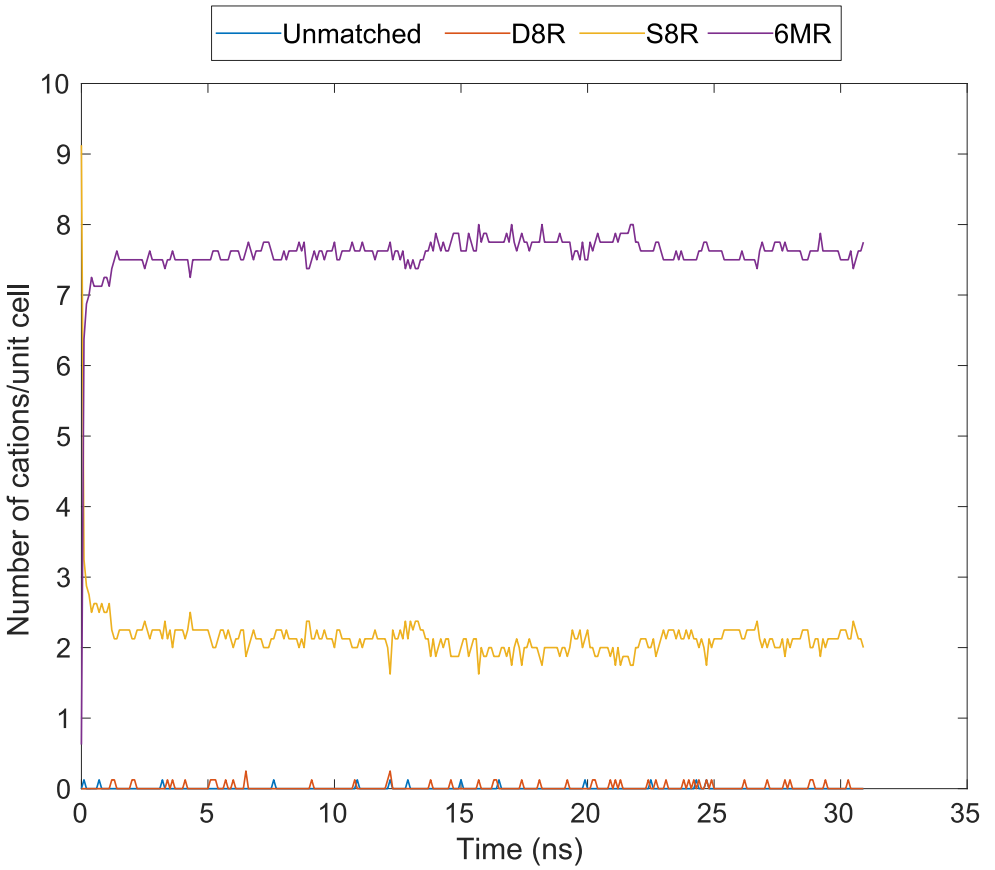

Figure 3.9: Cation sitings during 1000 K NVT MD run for Na-RHO

3.6.1. Metadynamics characterisation of energy wells

To help understand the change in cation site occupancies observed between Figure 3.7 and Figure 3.8, a metadynamics approach is employed using the PLUMED [84] plugin.

In a standard MD simulation, the energy of each atom is given by the sum of all the intramolecular and intermolecular interactions within a given cut-off distance (Equation (3.1)). In a metadynamics simulation, it is possible to attach an additional term U_{bias} to a user-defined set of atoms or molecules. In this case, a single cation. The bias potential is applied to the energy calculation of this cation only, with the energies of all other atoms calculated as normal.

$$U_{\text{total for cation of interest}} = U_{\text{forcefield}} + U_{\text{bias}} \tag{3.10}$$

The bias potential, $U_{bias,}$ is location dependent i.e. the bias potential is felt only when the selected cation is within a previously explored region of space. During the metadynamics simulation, a Gaussian sphere of a given total energy and radius is added to the location of the cation every N steps. Over time the Gaussian spheres provide sufficient energy for the cation to transition from one stable position to another.

To assess the stability of a cation within a 6MR and an 8MR, a single cation located in the 6MR of a central *lta* cage is subjected to an energy bias. The total bias energy required for escape is equivalent to the depth of the local energy well. In this simulation, the energy barrier calculations were performed by adding Gaussian spheres of radius 0.1 Å and energy 1 kJ/mol to the position of the cation every 500th step.

Alongside the regular trajectory, the result of a MD simulation with metadynamics is a file containing the location of each Gaussian sphere added to

the simulation over time. These must be integrated (summed) to provide a description of the energy well.

It is helpful to compare the depth of the energy wells in both a single dimension, as in Figure (3.11), and in all three dimensions, as in Figure 3.12b. When generating the 1D-plot in Figure (3.11), care was taken to ensure that for the points used, there were was only one region of coordinate space that mapped to the axial direction of interest.

If, for example, the axis of interest is defined parallel to the x direction, then the x values must be mapped by only a single region in the y and z directions. An exploration of phase space equivalent to Figure 3.10(L) would therefore be allowed but Figure 3.10 (R) would correspond to merging the energy of a cation in two different environments.

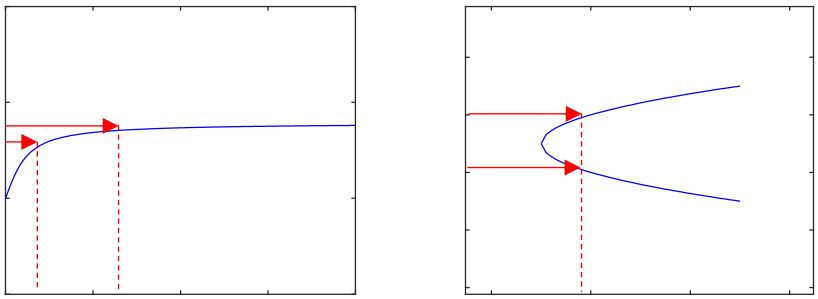

Figure 3.10: When integrating in 1 dimension, the left (L) figure shows an allowed region of phase space and the right (R) a forbidden region

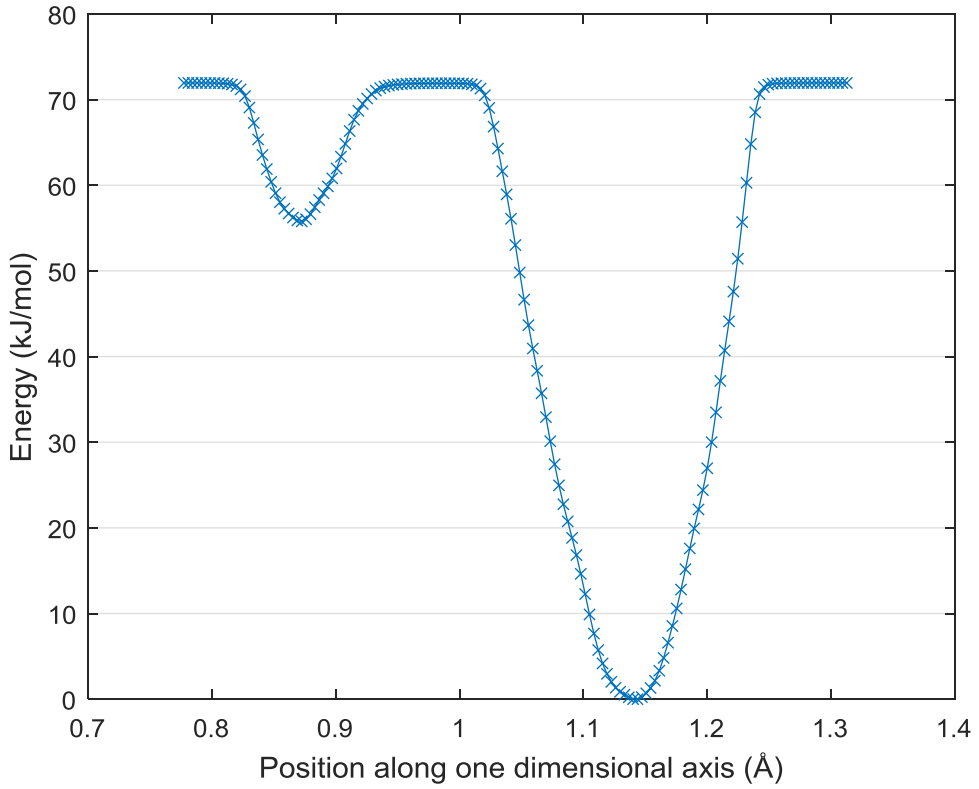

Figure 3.11: Energy profile associated with cation movement seen in Figure 3.12 projected in the x-direction at 300 K

The two wells seen in Figure 3.11 correspond, from left to right, to the energy associated with a cation in the 8MR and 6MR. The energy required to promote a cation from an 8MR to a 6MR is 16.2 kJ/mol, whereas the energy required to move a cation from an 8MR to a 6MR is 71.9 kJ/mol. At a temperature of 300 K, this corresponds to a Boltzmann factor of 1.5×10^{-3} for the 8MR→ 6MR transition and 3×10^{-13} for the 6MR → 8MR transition. At 1200 K, the same transitions corresponds to Boltzmann factors of 0.2 for the 8MR → 6MR transition and 7×10^{-4} for the 6MR to 8MR transition.

The probability of a transition occurring is directly proportional to its Boltzmann factor. The factors above show that the likelihood of a transition from a 6MR to an 8MR is substantially outweighed by that of a transition from an 8MR to a 6MR. However, it is important to remember that biasing was applied to a single cation only and that the energies above correspond to the other cations remaining in their

equilibrium 300 K positions. In the strictest definition, these energies cannot be decoupled entirely from the position of the other cations. Once a 6MR is occupied for example, the energy barrier to move a second cation into the 6MR would be significantly higher. Consequently, once all the 6MRs are occupied, some cations are forced to remain in 8MRs.

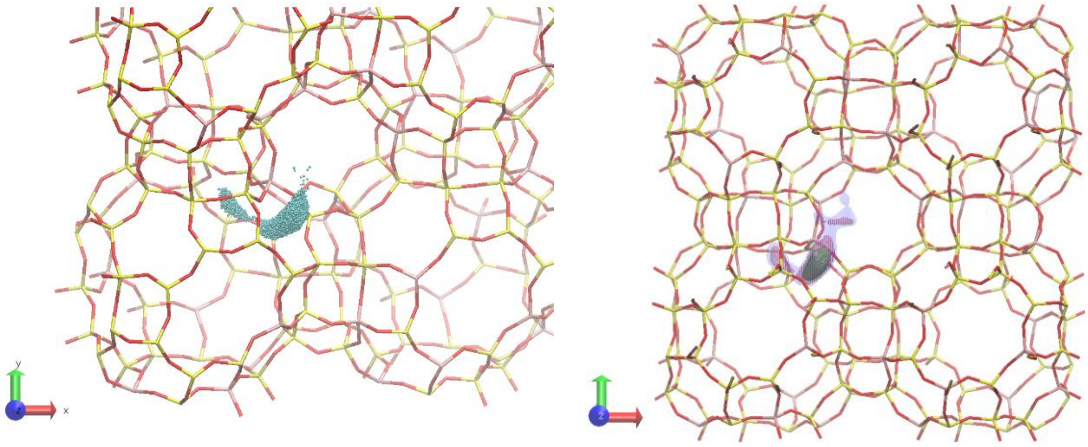

Figure 3.12: Energy biasing metadynamics at 300 K. Left shows all points explored, right energy barriers at 50 kJ/mol (green), 80 kJ/mol (red) and 100 kJ/mol (blue). The left figure is angled slightly to show that the prominent direction which can be integrated over in Figure 3.11. The requirement to angle the snapshot as opposed to the image on the right highlights the difficulty of integrating in one direction only.

Figure 3.12(L) shows all the positions occupied by the cation that was promoted in energy and Figure 3.12(R) shows the corresponding isoenergetic surfaces. The central green surface corresponding to 50 kJ/mol shows that with these forcefield parameters, the energy required to move the cation out of the 6MR is high. At 80 kJ/mol, the cation is almost able to escape the central region but it is not until the energy is raised to 100 kJ/mol that there is a fuller exploration of configurational space. It is this high energy barrier which stops cations transitioning back to an 8MR after moving to a 6MR. The discrepancy with Figure 3.11, i.e. 71.9 kJ/mol for escape compared to just over 80 kJ/mol to escape, can be explained by the approximation introduced in projecting a three dimensional movement between sites into one dimension.

3.6.2. Comparison with DFT calculations

To provide further insight into why the simulations suggest that the cations should sit preferentially in the 6MR ring, when the experimental data suggests preferential occupation of the 8MR, a switch to quantum mechanical (QM) modelling is made. This first principles approach gives a more accurate description of the interactions between atoms so can be used as a tool to help explain the differences seen in the cation distributions.

DFT calculations are more computationally intensive than their classical counterparts so a smaller 1 x 1 x 1 unit cell is used. If 10 of the 48 silicon atoms are exchanged for aluminium atoms, this gives a Si/Al ratio of 3.8 (the closest possible to the experimental value of 3.92 for a single unit cell).

Two initial configurations are prepared for the QM simulations using classical mechanics. The first structure is generated from a 1 μs run (with cation occupancies which match the experimental measurements i.e. 6 cations in the 8MRs) and the second structure from REMD (which have inverted occupancies compared to the experimental measurements i.e. 6 cations in the 6MR). The cut-off for these classical 1 x 1 x 1 simulations is reduced from 14 Å to 7 Å to ensure that the minimum image convention (Section 2.5) is obeyed. The charges are also adjusted slightly to ensure charge neutrality (Figure 3.1). Otherwise the simulation parameters are left unchanged from the standard simulations (see Appendix A-D for sample input files).

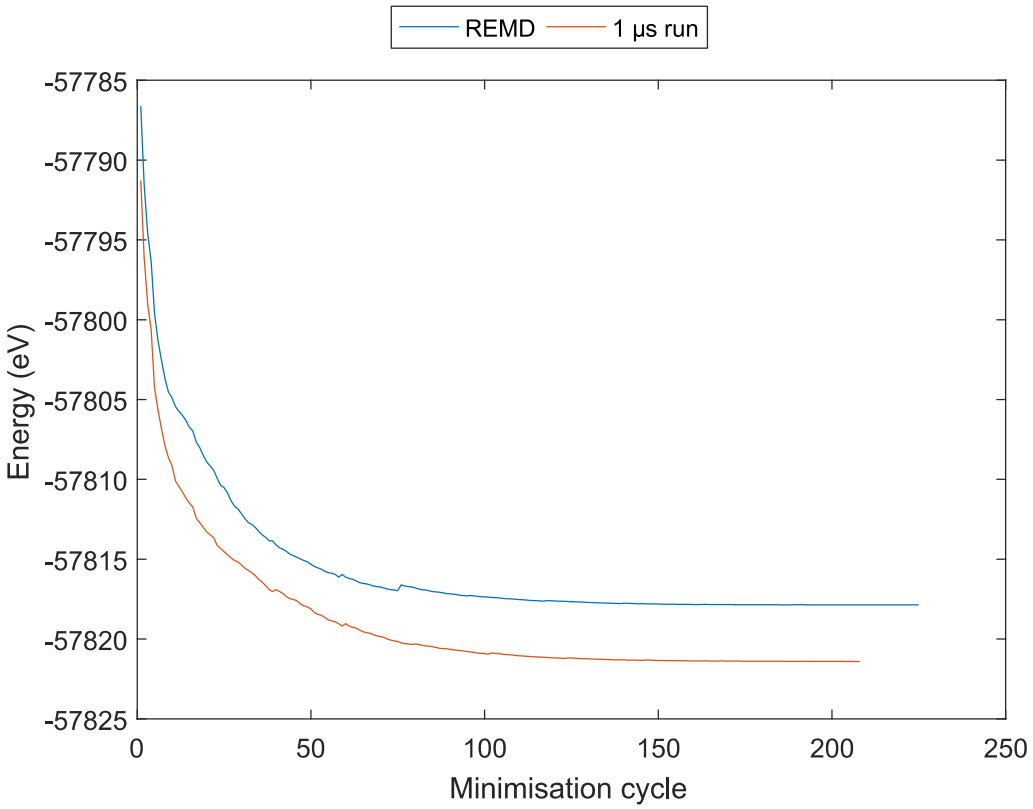

Figure 3.13: Energy during QM geometry optimisation. The starting structure for the orange curve was from the 1 μs MD simulation with 6 cations/uc in the 8MR and the starting structure for the blue curve was from the REMD run with 3 cations/uc in the 8MR.

Following the classical simulations, each structure undergoes a QM geometry optimisation (Figure 3.13). In contrast to the classical modelling (Figure 3.8), this shows that the REMD structure with 6 cations in the 6MR is higher in energy than the 1μs structure with 6 cations in the 8MR. The same trend is found in an *ab initio* molecular dynamics (AIMD) run at 300 K. This agreement with experimental data is the first indication that the classical parameters may require further examination.

3.6.3. Effect of heating and hydration on cation distributions

Before investigating the classical force field parameters in more detail, the Na-RHO sample is checked to see whether heating the sample changed the cation positions. It is known that in Cd-RHO, cations move from the 8MR to the 6MR on heating [85] and in Pb-RHO, cations from the S8R to the D8R [85] on heating. In Cd-

RHO, once all bound water is removed above 400 – 500 K, the cations remain in their new positions on cooling.

To investigate whether the presence of water changes the Na^+ distribution in Na-RHO, a sample is thoroughly heated in a furnace at 400 °C, 500 °C and 600 °C, sealed and then allowed to cool before undergoing X-ray Diffraction (XRD) measurements to determine the cation positions. These show no substantial change in cation position below 500 °C (Figure 3.14). This supports the cation positions obtained with the DFT calculations and indicates a problem with the classical simulations.

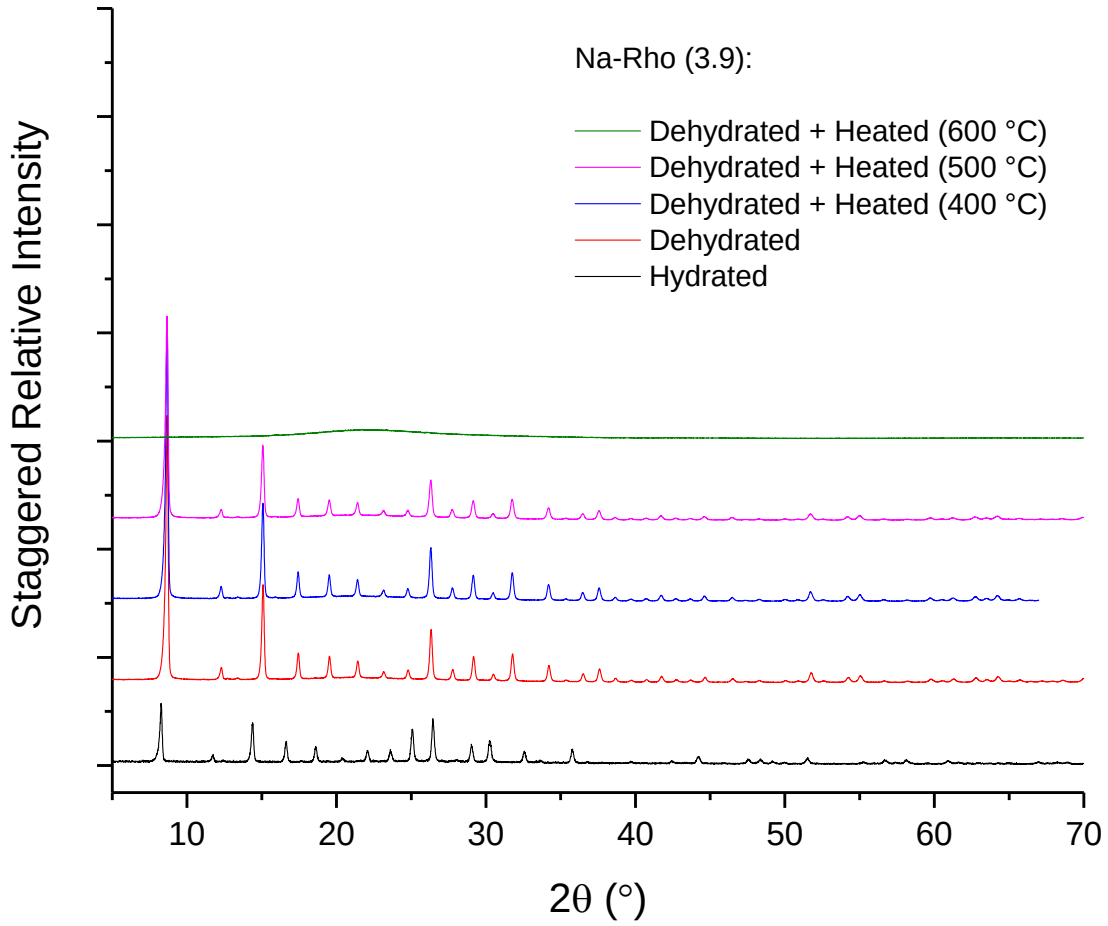

Figure 3.14: XRD measurements of Na-RHO (the dehydrated line in red corresponds to the original sample which was dehydrated at 200 °C). The sample heated to 600 °C becomes amorphous.

3.6.4. Further investigations

It is surprising to see such a marked difference in cation positions between the classical and QM simulation and this led to two branches of further investigation.

a) The bonded interactions may not be adequately modelling the framework - framework interactions. A difference in the framework structure could lead to the 6MRs becoming a more favourable site for the cation to sit in than expected.

b) The fundamental difference in the energies for the two states calls into question the validity of the sodium parameters used. For AIMD to predict the opposite trend to the classical simulations indicates that the sodium parameters may need further adjustment.

3.6.4.a. Framework-framework interactions

From the AIMD trajectory, the average bond lengths and bond angles were calculated (Table 3.10). The trajectory starts from an equilibrated structure (time = 0) run using the classical MD with 6 cations in the 8MR. The evolution of the bond lengths and bond angles can be seen in Figure 3.15 and Figure 3.16. In each subplot, the average based on the final 50% of data points (output every frame) is shown in red.

Table 3.10: Comparison of geometric parameters in Na-RHO using DFT and classical simulations

Bond	Forcefield (Å)	DFT (Å)	Experimental (Å) [7]
Si-O	1.61	1.635	1.65
Al-O	1.73	1.761	
Si-Si (Urey-Bradley)	3.12	3.045	3.046
Si-Al (Urey-Bradley)	3.18	3.073	
Bend	Forcefield (degrees)	DFT (degrees)	Experimental (degrees) [7]
O-Si-O	109.5	109.4	109.43
O-Al-O	109.5	109.3	
Si-O-Si	149.5	131.9	135.07
Si-O-Al	149.5	136.2	

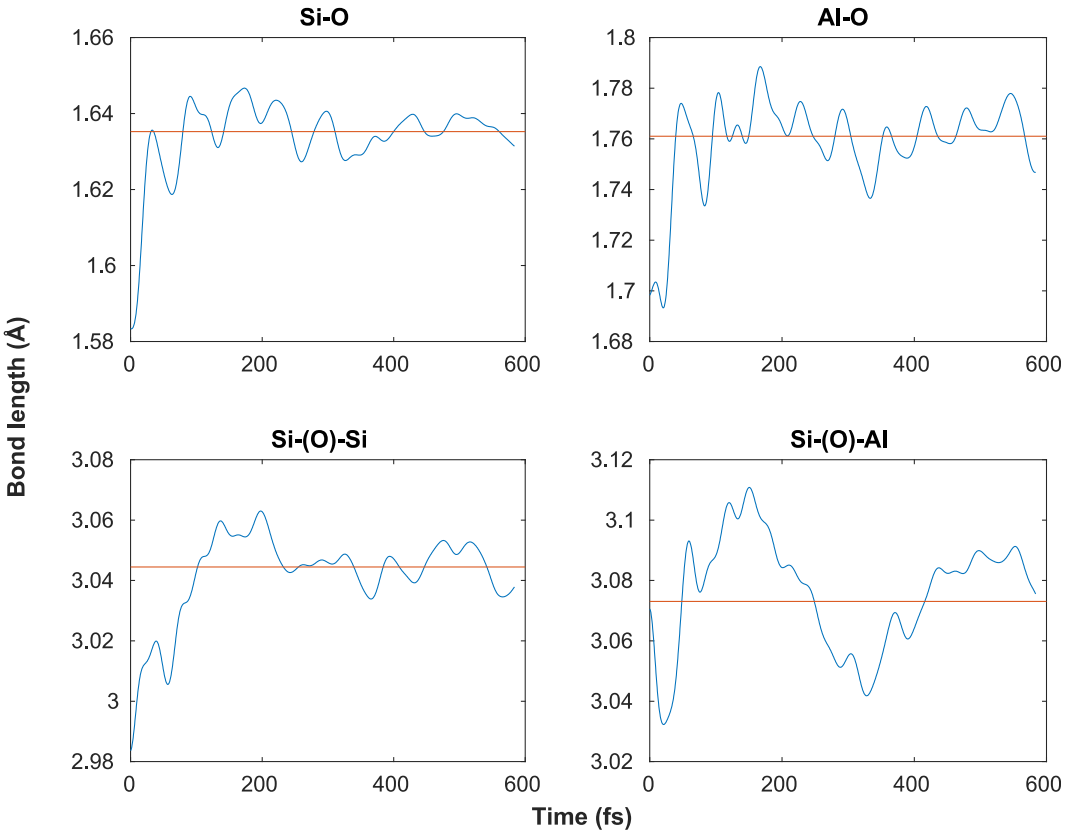

Figure 3.15: Bond lengths in DFT AIMD simulation (average value over the final 50% shown in red)

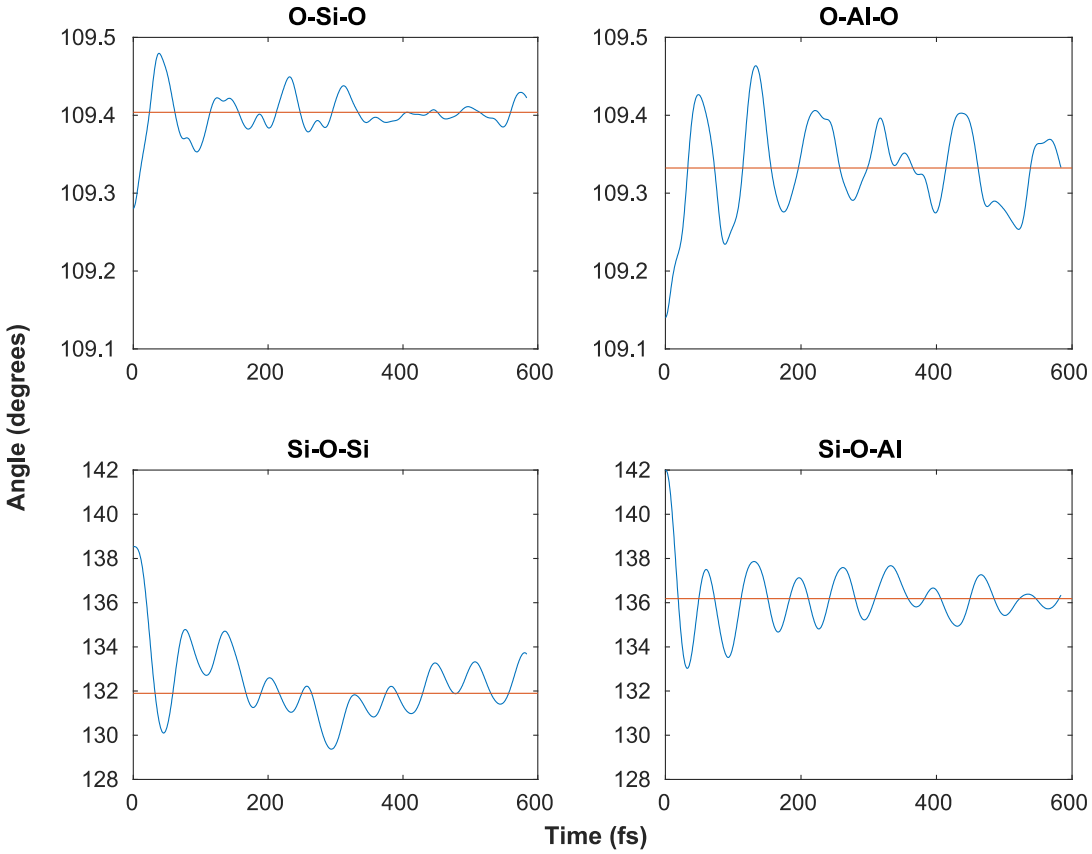

Figure 3.16: Angle bends in DFT AIMD simulation (average value over the final 50% shown in red)

There is a particularly noticeable difference between the classical and DFT values for the T-O-T angle bends in Table 3.10. To investigate how this difference effects the dynamics of the system, the equilibrium bond lengths and bond angles used in the classical simulation were changed to the average value obtained from the DFT simulation. The spring constants were left unchanged (i.e. it was assumed that the present values represented their chemical environments suitably and only the equilibrium values were offset from their correct values). The Coulombic 1-4 scale factor was adjusted from 0.35 to 0.409 in order to reproduce the correct unit cell dimensions with the new parameters. The distortion of the 8MR rings was then calculated (Equation (2.1)).

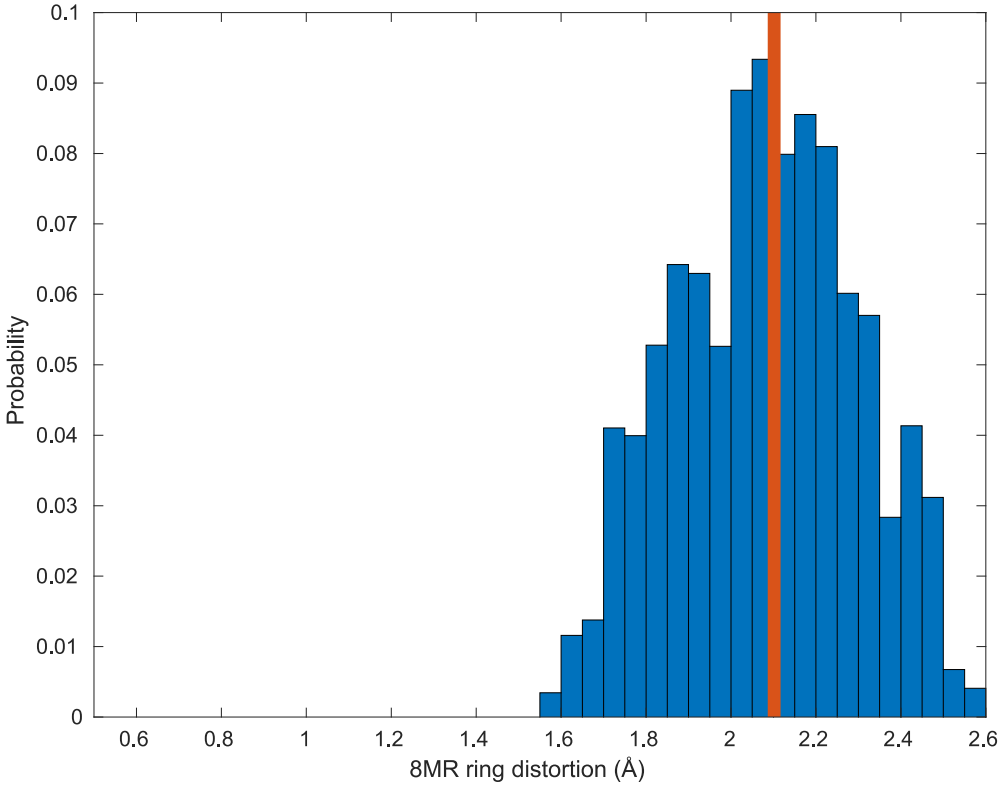

Figure 3.17: 8MR distortion for all rings in a DFT simulation at 298 K (experimental in red)

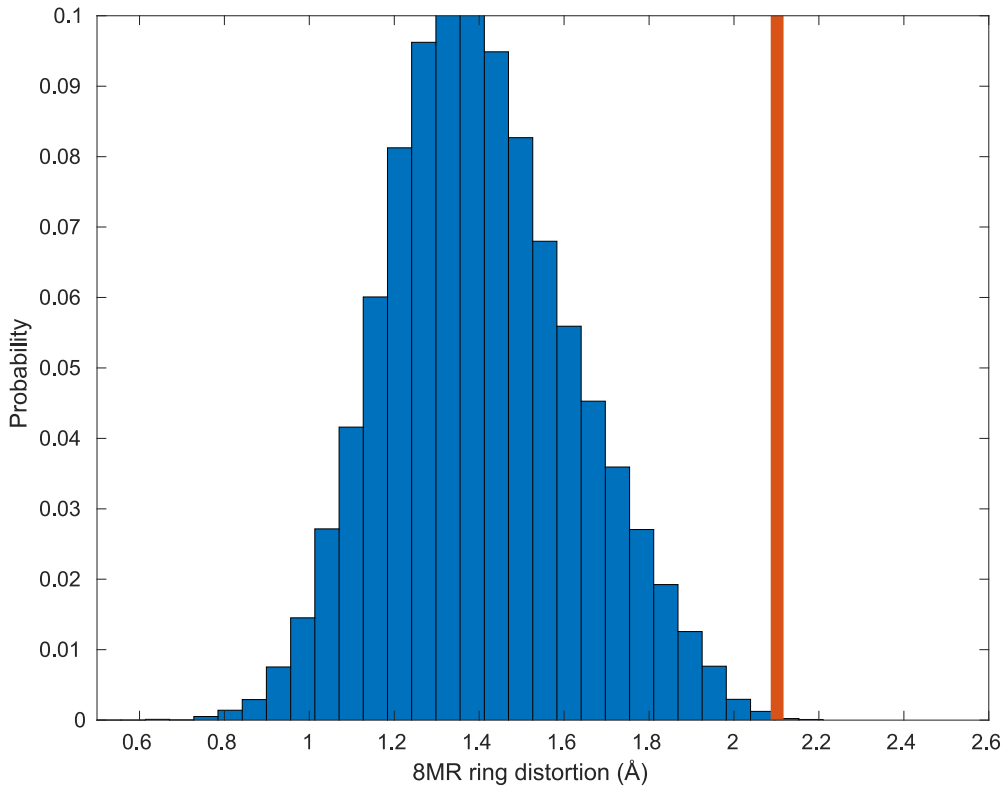

Figure 3.18: 8MR ring distortion for all rings and in a classical MD simulation with the original parameters at 298 K (experimental in red)

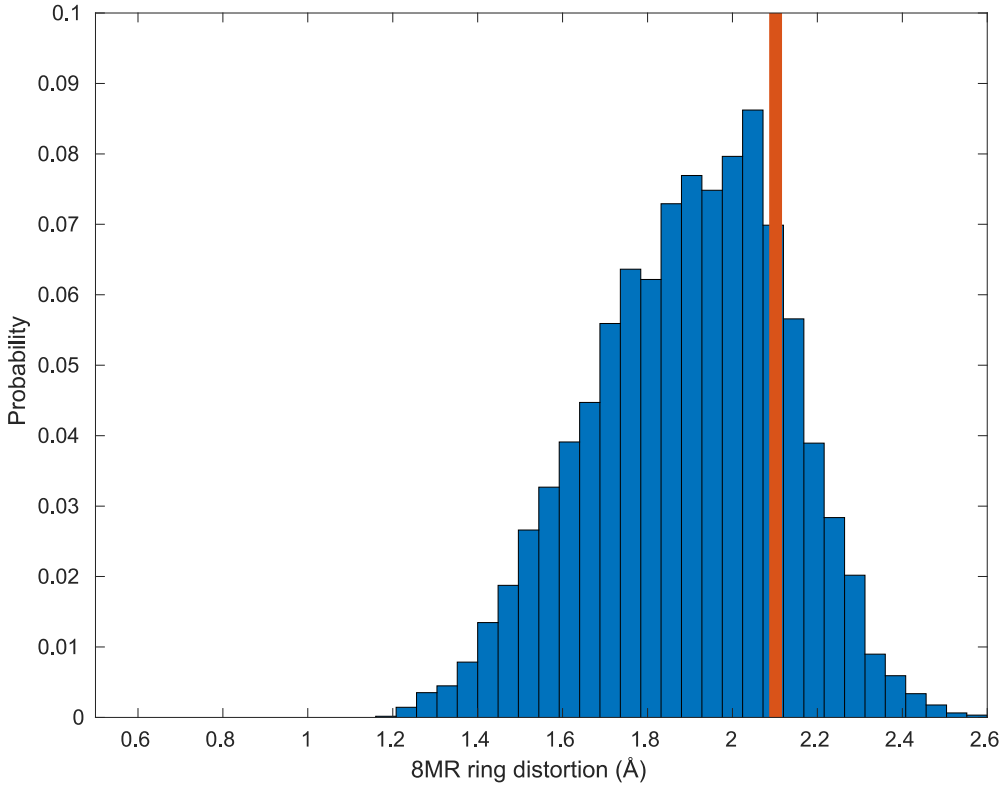

Figure 3.19: 8MR ring distortion for all rings and in a classical MD simulation with the new parameters at 298 K (experimental in red)

The new parameters (Figure 3.19) show a significant improvement in window distortion compared to the original parameters (Figure 3.18). With the original parameters, the peak window distortion is 1.38 Å, whereas for the new parameters the peak is at 2.0 Å - much closer to the experimental value of 2.1 Å.

The remaining difference indicates that the force field is not yet fully optimised. The aim here is to gain an insight into the trapdoor behaviour of RHO, rather than to predict with perfect quantitative agreement, the distortion seen in DFT and experimental work. The new values therefore offer a much more reasonable representation of the Na-RHO structure.

Figure 3.19 shows the cation locations for a REMD simulation with the new, more elliptical 8MRs. Even in this case however, the 6MRs are preferred by the Na^+ cations. This suggests that it is not the bonded parameters (hence the shape of the rings) which dominate the cation distribution.

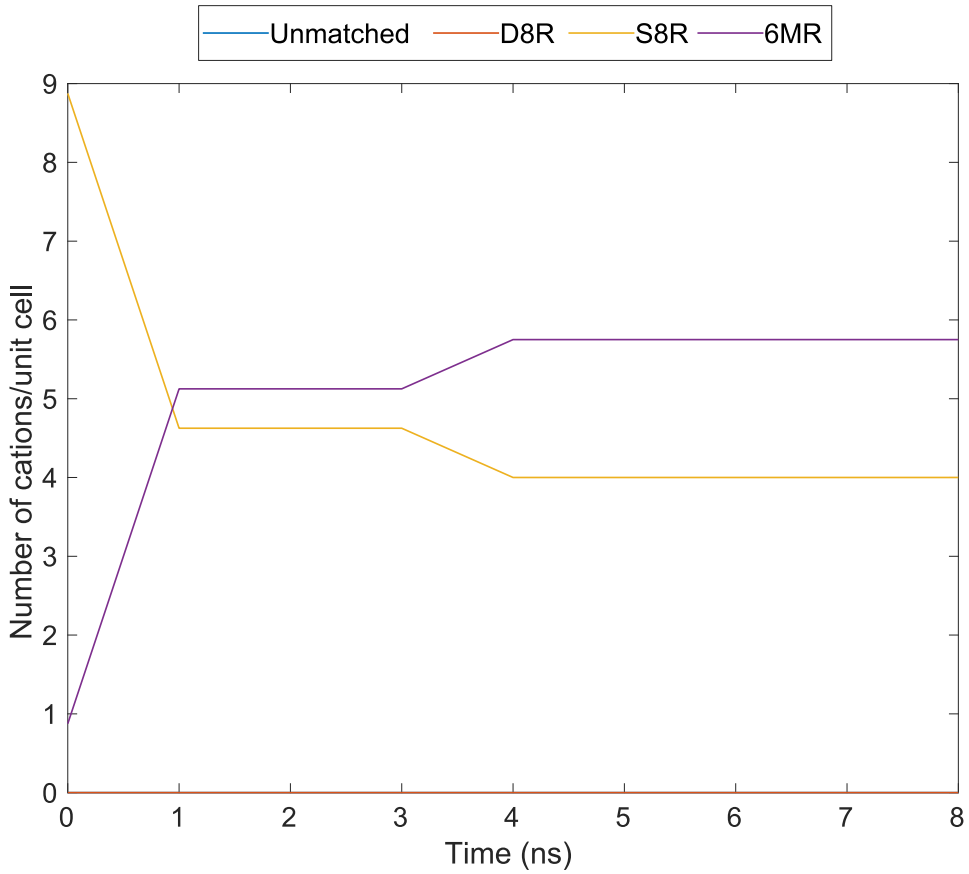

Figure 3.20: REMD using DFT derived bonded parameters (Table 3.10). The expected experimental occupancies are 6 cations in the 8MR and 3 cations in the 6MR (Table 3.9)

3.6.4.b. Lennard-Jones cation parameters

Table 3.11 gives the site occupancies of Na^+ with the DFT adjusted parameters. Highlighted in green/with one asterisk are optimal parameters using the original bonded interactions. In orange/with two asterisks are the optimal parameters with the new bonded interactions. Parameters marked 'isotherm' by Maurin et al. [80] and Aqvist et al. [48] match the experimental isotherm well. The parameters marked 'cation', by Jeffroy et al. and Akten et al. [49], have similar epsilon values to Maurin et al. [80] and Aqvist et al. [48] but their higher sigma values yield the correct cation positions (at the expense of matching the CO_2 isotherm). For this process, the 1-4 factors have been readjusted to reproduce a unit cell length of 14.41 Å [7]. These scale factors, along with their previous values, are provided in Table A.7 (Appendix A).

It is interesting that with both the new and old parameters sets, the sigma parameter to obtain a good match with the isotherm (Figure 3.25) is around 1.8 Å but to obtain a good match with the cation positions requires a larger sigma value of around 2.7 Å. Changing from the old to the new parameter sets, requires a lower epsilon value to obtain a good match to the adsorption isotherm.

A more detailed examination of Table 3.11 (Figure 3.21) shows that the number of cations present in the 6MR is controlled largely by the sigma value. A similar plot against the epsilon value is uninformative. By adjusting the sigma value from 1.5 Å to 4.0 Å, the number of cations in the 6MR changes from six to two cations. It therefore seems to be a size effect that governs the number of cations that can fit into the 6MR.

Table 3.11: LJ parameters for Na^+ and their cation occupancies following REMD. For the parameters by Garcia-Sanchez et al.[69], Na^+ parameters are derived from the Na-C and Na-O interactions with CO_2, assuming the Lorentz-Berthelot mixing rules in Equation (3.11) and (3.12) Parameters marked in green and one asterisk (*) are the optimal parameters with the original forcefield parameters. Parameters marked in orange and with two asterisks (**) are the optimal parameters with the modified forcefield. The keyword "- cation" indicates a good match to the experimental cation sitings. The keyword "- isotherm" indicates a good match to the experimental isotherm.

Top performing parameters	Descriptor	sigma (Å)	epsilon/k_B (K)	D8R	S8R	6MR
	Jaramillo et al. [75]	3.2	19.99	0	9.5	0.25
	Larentzos et al. [78]	2.876	62.74	0	9.4062	0.3125
	Lee et al. [79]	2.47	442.3	0	9.2188	0.5312
	Jensen et al. [76]	4.07	0.25	0.0938	9.0312	0.625
	Garcia-Sanchez et al. (CO_2) [69]	2.5	470.8	0.0312	9.0938	0.625
	DREIDING [73]	2.8	251.6	0.1875	8.4375	1.125
	Vujic et al. [82]	3.23	234.13	3.4375	4.4062	1.9062
	Jensen et al. [76] (prior)	3.33	1.39	0	6.75	3
** - cation	Akten et al. [49]	2.85	8	0.0312	6.6875	3.0312
* - cation	Jeffroy et al. [55]	2.59	50.27	0	6.375	3.375
	Cygan et al. [72]	2.35	65.47	0	6.125	3.625
	Halicioğlu et al. [74]	3.475	1600	5.25	0.5312	3.9688
	Demontis et al. [63]	2.43	80.01	0	5.75	4
	Lamoureux et al. [77]	2.58	15.86	0	5.125	4.625
	Rao et al. [81]	1.28	5.03	0	4.2188	5.5312
	UFF [47]	2.66	15.1	0	4.2188	5.5312
	Beerdsen et al. [70]	2.33	46.8	0	4	5.75
	CVFF [71]	1.9	808.8	0	3.9688	5.7812
	Grootenhuis et al. [86]	1.6	5.03	0	3.375	6.375
	Watanabe et al. [83]	1.746	20.63	0	3.25	6.5
** - isotherm	Aqvist et al. [48]	1.83	13.25	0	3.2188	6.5312
* - isotherm	Maurin et al. [80]	1.75	50.36	0	3.2188	6.5312
	Purton et al. [87]	2	65.46	0	3.125	6.625
	Garcia-Sanchez et al. [69] (CO2)	3.9	4385	0.875	0	8.875

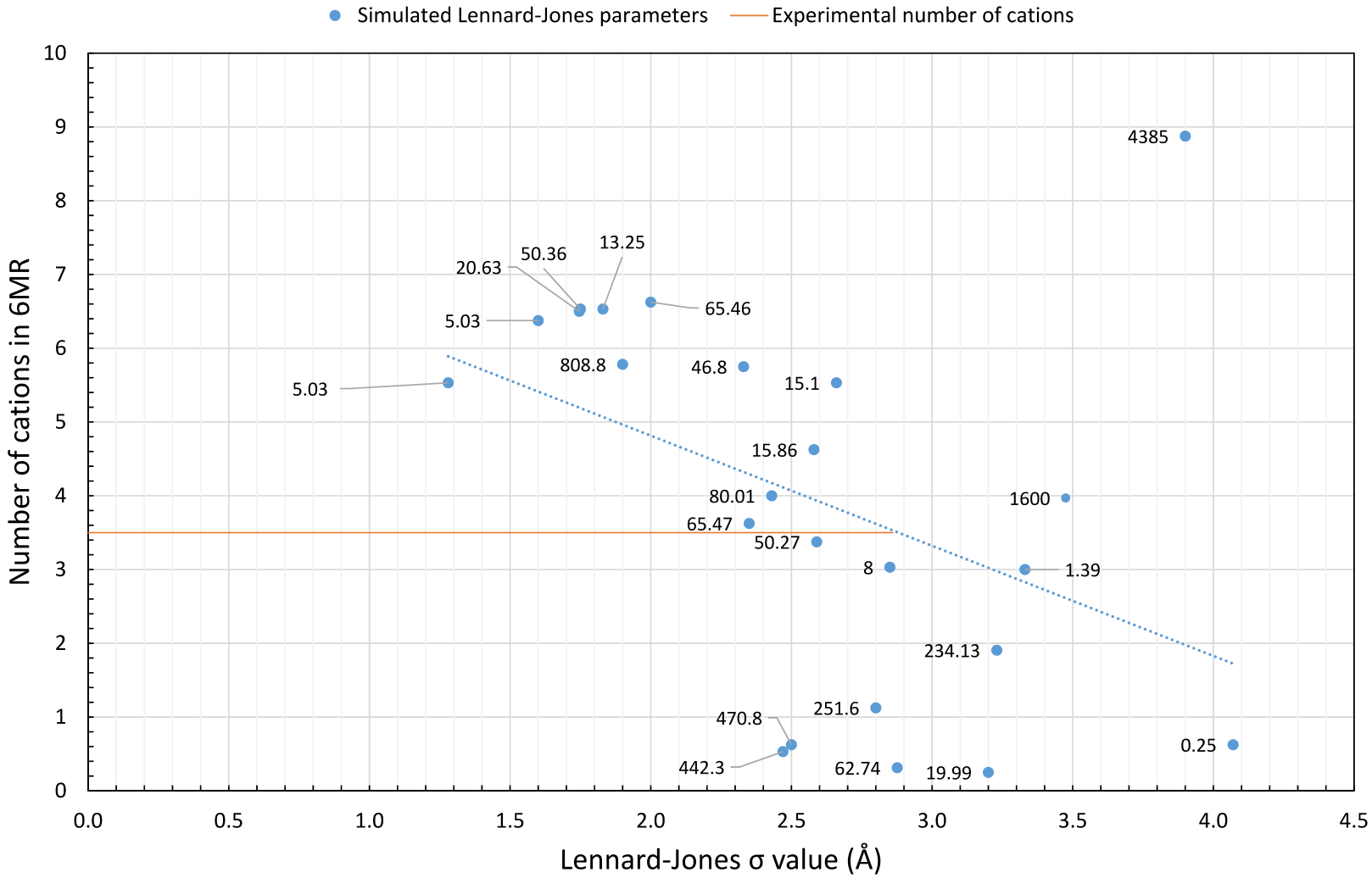

Figure 3.21: Number of cation present in 6MR as LJ parameter is varied. Values attached to data points show the epsilon/k_B value in Kelvin with the experimental number of cation red for reference and a line of best fit added to show the effect of increasing σ on the number of cations in the 6MR

As the number of cations in the 6MR is effectively a function of sigma only (Figure 3.21), one avenue of exploration is to tune the value of sigma to obtain the correct cation distribution and tune the value of epsilon to reproduce the expected cell expansion and adsorption isotherm on uptake of CO_2.

From Figure 3.21, it is likely that the optimal Lennard-Jones sigma parameter for matching the experimental cation occupancy lies somewhere between 2.0 Å and 3.0 Å. This is used as a starting point for a systematic study of sigma and epsilon values.

Sigma values are chosen in 0.2 Å intervals between 2.0 Å and 3.0 Å and the following epsilon values are chosen 10 K, 20 K, 40 K, 60 K and 80 K. This covers the region of phase space where, based on traditional forcefields such as UFF [47], a suitable Lennard-Jones parameter might be expected to lie. (The full range of sigma and epsilon values used to model Na^+ in the wider simulation community, as seen in Figure 3.21, is large.)

The first step in testing the new parameters is to find the 1-4 Coulombic scale factor that reproduces the experimental unit cell length of 14.4139 Å (Table 3.12).

Table 3.12: Sensitivity of 1-4 Coulombic scale factor

Epsilon/k_B (K)	Sigma (Å)					
	2	2.2	2.4	2.6	2.8	3
10	0.405	0.413	0.415	0.405	0.4	0.39
20	0.41	0.413	0.41	0.405	0.395	0.385
40	0.415	0.415	0.41	0.4	0.385	0.375
60	0.415	0.415	0.41	0.395	0.38	0.365
80	0.42	0.413	0.4	0.39	0.375	0.36

Several trends can be identified by examining Table 3.12:

i) At constant epsilon, there is a general decrease in the scale factor with increasing sigma.

ii) At higher sigma values, ($\sigma > 2.2$ Å), the Coulombic scale factor decreases with increasing epsilon. The decrease is more substantial as sigma increases.

iii) At $\sigma = 2.2$ Å, the scale factor is insensitive to the value of epsilon.

iv) At $\sigma = 2.0$ Å, the opposite trend is seen – the scale factor increases with increasing epsilon.

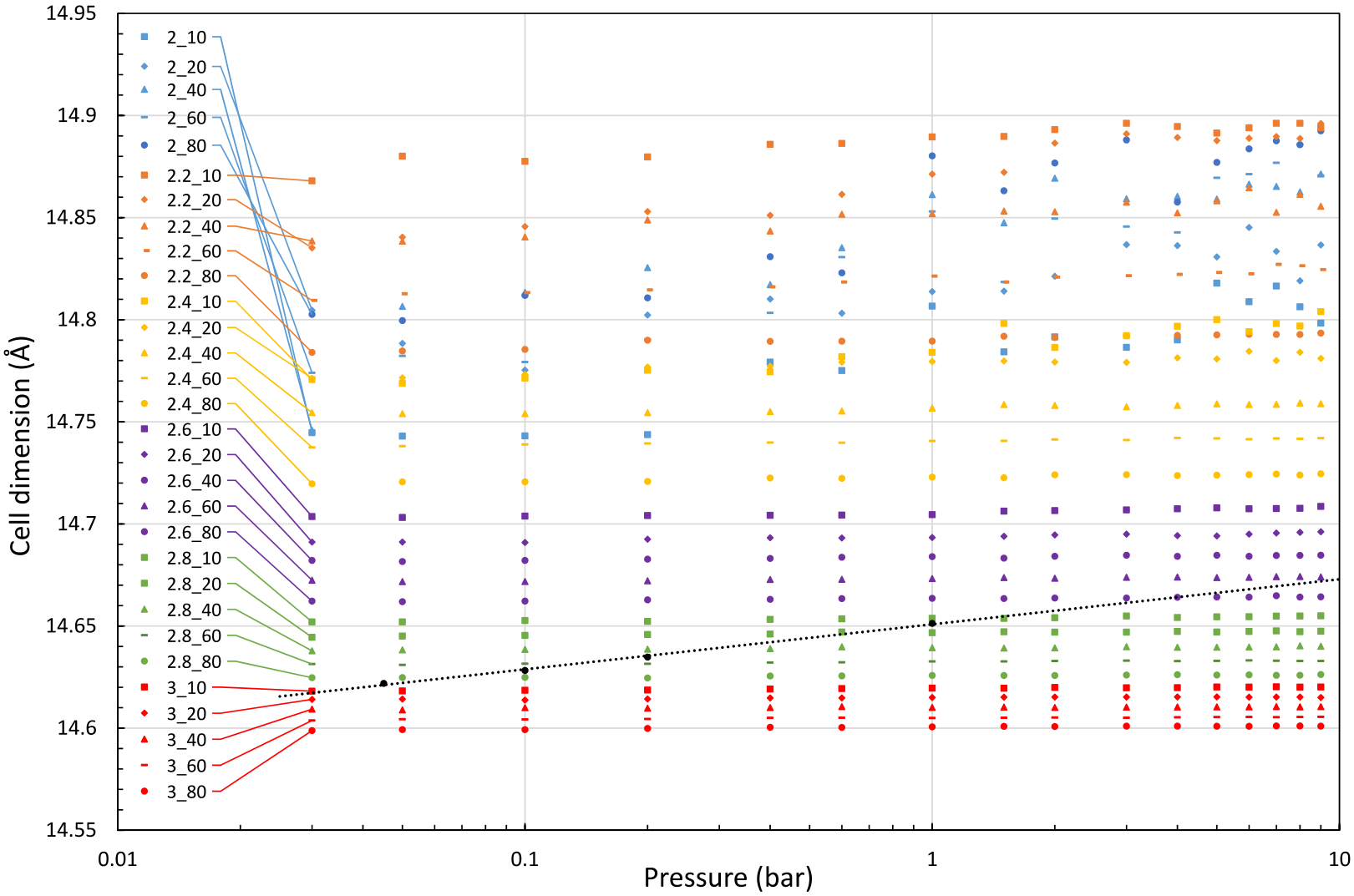

Figure 3.22: Cell expansion as a function of pressure for parameters tested (nomenclature is sigma_epsilon). Experimental points are in black with a line of best fit

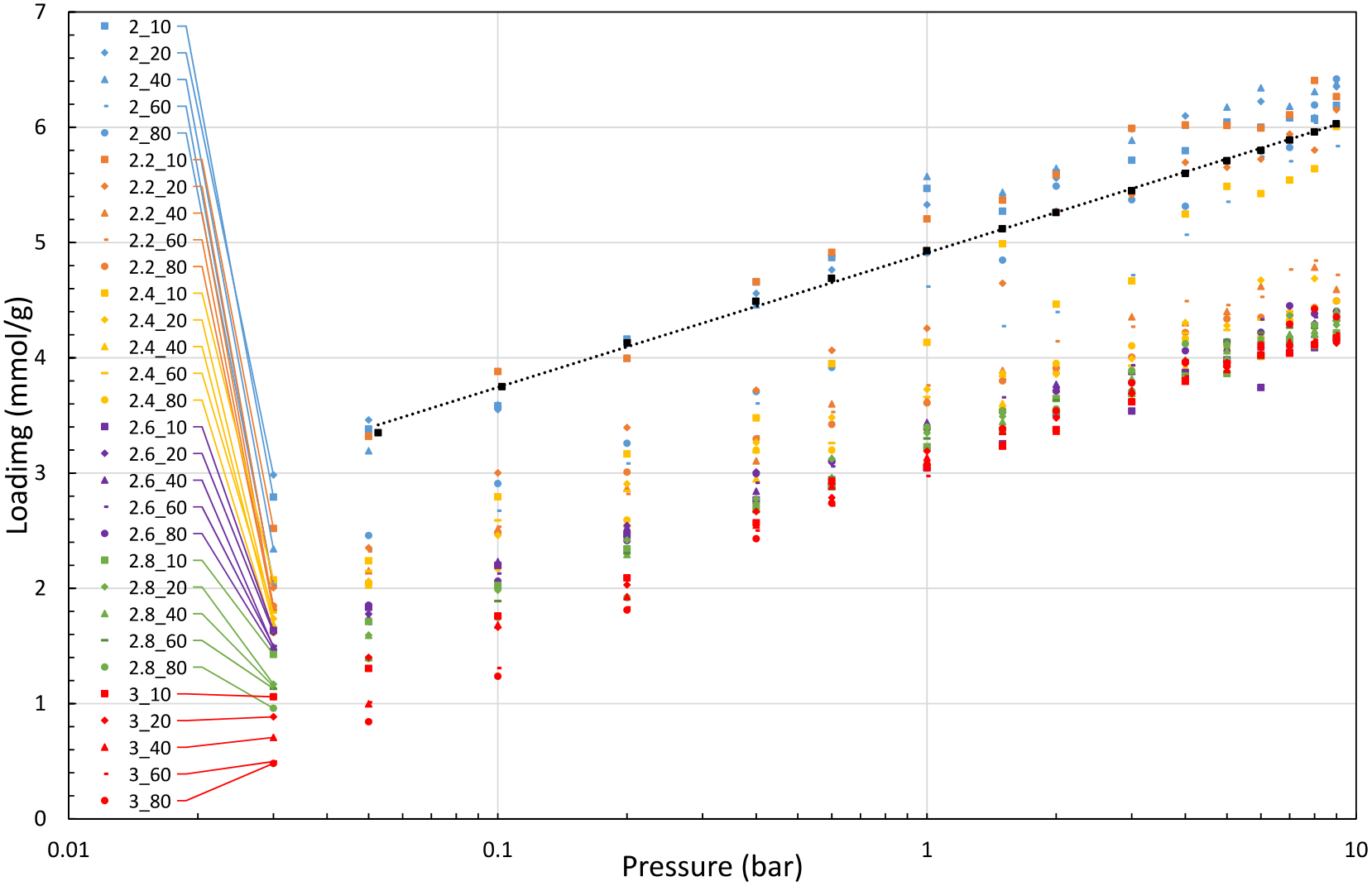

Figure 3.23: Isotherms for parameters tested (nomenclature is sigma_epsilon). Experimental points are in black with a line of best fit

Figure 3.22 and Figure 3.23 show the cell parameters and adsorption isotherms obtained after three rounds of MC and MD. In general, increasing sigma from 2.0 Å to 3.0 Å results in reduced uptake and cell contraction. Increasing epsilon from 10 K to 80 K also shifts both the isotherm and cell expansion downwards but more gradually compared to increases in sigma. An exception to this rule is seen in the cell expansion for sigma parameters at 2.0 Å which show less expansion than parameters which have sigma = 2.2 Å.

The most promising parameters for matching the experimental adsorption isotherm are for sigma = 2.0 Å with an epsilon value between 10 and 40 K. Sigma = 2.2 Å and epsilon = 10 K also shows promise. However, these values show some of the biggest deviations from the experimental measurements of the unit cell length.

Table 3.13 and Table 3.14 show the cation positions obtained following a REMD simulation with no gas present. Shaded cells match the experimental cation position within ± 1 cation. Combinations which match the experimental isotherm well (low sigma and low epsilon) again show a preference a preference for ≈ 6 cations in the 6MR and ≈ 3 cations in the 8MR.

Table 3.13: 6MR occupancy (experimental = 3.5 cations)

Epsilon/k_B (K)	Sigma (Å)					
	2	2.2	2.4	2.6	2.8	3
10	6.75	6.75	4.875	3.625	3.5	2.5
20	6.875	6.75	3.75	3.5	2.25	0.125
40	6.125	4	3.125	2.875	0.125	0.125
60	6.625	3.875	2.625	2.25	0.125	0.125
80	5.375	3.625	2.375	0.125	0.125	0.625

Table 3.14: 8MR occupancy (experimental = 6 cations)

Epsilon/k_B (K)	Sigma (Å)					
	2	2.2	2.4	2.6	2.8	3
10	3	3	4.875	6.125	6.25	7.25
20	2.875	3	6	6.25	7.5	9.625
40	3.625	5.75	6.625	6.875	9.625	9.625
60	3.125	5.875	7.125	7.5	9.625	9.625
80	4.375	6.125	7.375	9.625	9.625	8.75

Inspection of the cation occupancies (Table 3.11/Table 3.13/Table 3.14), the adsorption isotherms (Figure 3.23/ Figure 3.25) and the cell expansion (Figure 3.22 / Figure 3.24) does not produce an ideal set of parameters which match the experimental data. A particular problem arises when investigating the diffusion mechanism of CO_2 if the strength of the cation-framework interactions are not correct. If cations migrate to the 6MRs, leaving 8MRs unoccupied, the diffusion barrier to intercage diffusion is reduced leading to an overprediction in the diffusion rate. A compromise is therefore required, ensuring first and foremost that the cation positions are correct.

3.6.5. Influence of LJ mixing rules

In many zeolite forcefields [52] [55], the Lennard-Jones interactions between Na^+ cations and the Si and Al framework atoms are neglected (due to shielding). Na^+-Na^+ interactions are also neglected (dominated by Coulombic interactions). Table 3.15 shows that there is little effect on the cation positions in removing the Na^+-Na^+, Na^+-Si and Na^+-Al interactions which supports these more general assumptions. Removing the Lennard-Jones interactions entirely causes the system to collapse.

Table 3.15: Effect on cation siting of excluding Lennard-Jones sodium interactions (all Coulombic interactions remain)

Description	Cations in 8MR	Cations in 6MR
All interactions	2.8750	6.8750
Na^+-Si/ Na^+-Al excluded	2.5000	7.2500
Na^+-Na^+/ Na^+-Si/ Na^+-Al excluded	2.8750	6.8750
Na^+-Na^+/ Na^+-Si/ Na^+-Al/Na^+-O excluded	Unstable	Unstable

In the forcefield model, the Lennard-Jones parameters between unlike species have been calculated using the Lorentz-Berthelot mixing rules:

$$\sigma_{mix} = \frac{1}{2}(\sigma_A + \sigma_B) \tag{3.11}$$

$$\varepsilon_{mix} = \sqrt{(\varepsilon_A \varepsilon_B)} \tag{3.12}$$

These mixing rules are commonly used but lack a physical basis [88] and cases where they do not hold are well-documented [88] [89] [90] [91] [92]. As the Na^+-O interaction dominates the behaviour of the system, this is examined more closely. The approach taken in this section is to model the Na^+-O interaction using a different set of Lennard-Jones parameters for the Na^+ than is used for the remaining Na^+-Other Lennard-Jones interactions. There is not altogether unusual, as the cation-oxygen parameter is sometimes modelled as a separate Buckingham potential, independent of the other Lennard-Jones interactions [55].

In addition to as the systematic study of Lennard-Jones parameters in Section 3.6.4, the earlier parameters sets are considered here too (Figure 3.24 and Figure 3.25).

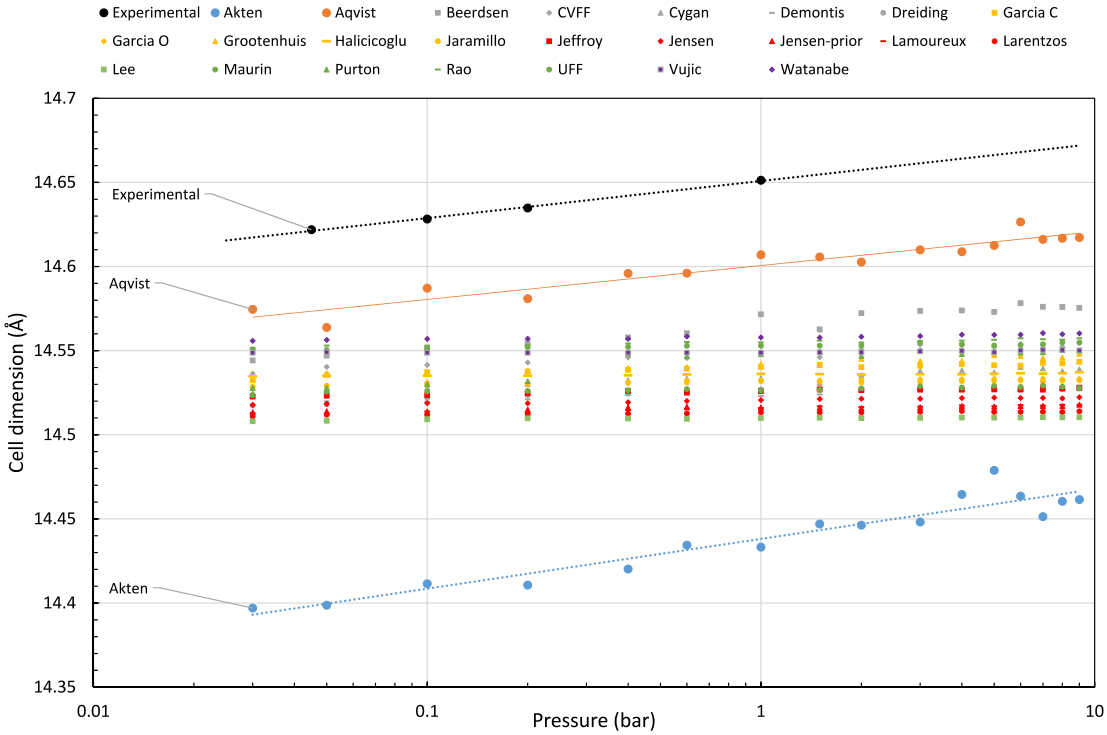

Figure 3.24: Cell dimension obtained testing parameters in Table 3.5 with modified spring constants

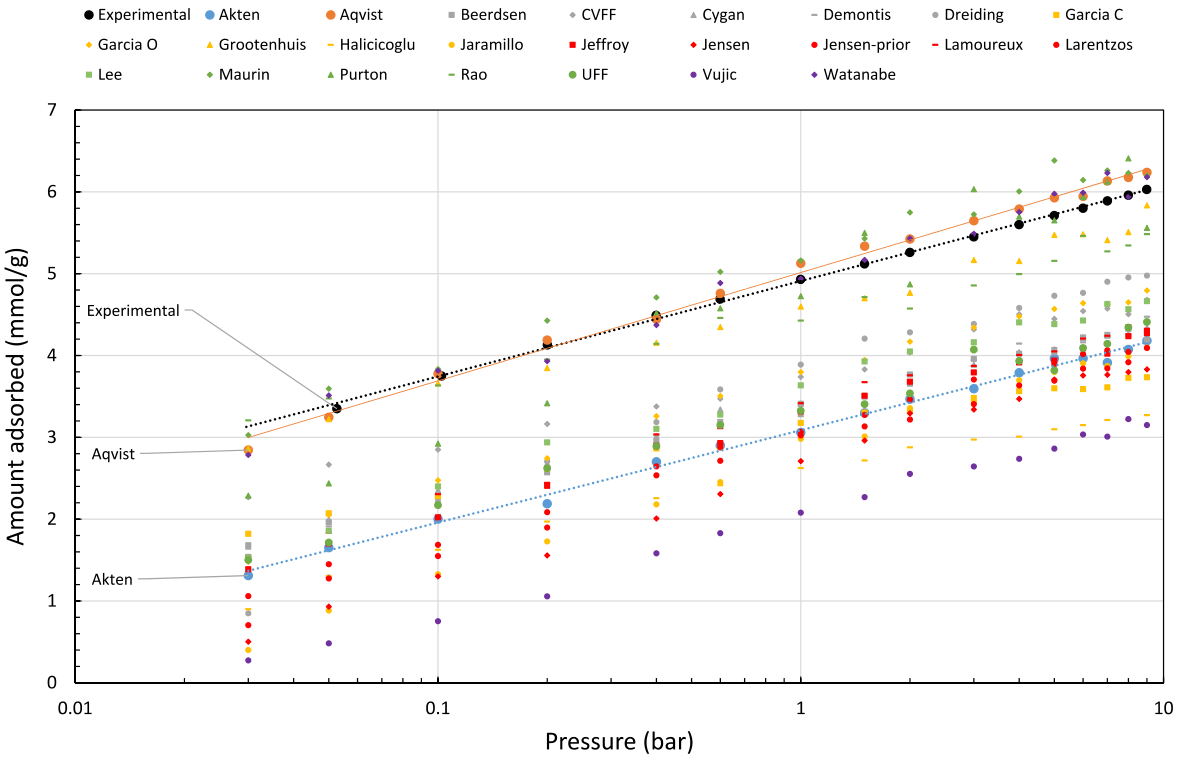

Figure 3.25: Isotherms obtained testing parameters in Table 3.5 with modified spring constants

Of the parameters investigated, the parameters by Aqvist et al. [48], which consider free ions in water, agree well with the experimental isotherm; whilst those by Akten et al. [49], derived from Na^+ interactions in a zeolite, give a good match to the cation positions. This pairing is interesting because the zeolite parameters by Akten et al. [49] are offset from those by Aqvist et al. [48]. The sigma values for the two sets are quite different (2.85 Å and 1.83 Å respectively), especially with regard to Figure 3.21. When considering the range of ε values used to model Na^+ (0.25 K to 1600 K in Table 3.11) however, the values of ε are almost the same (8 K and 13.25 K).

A final set of parameters are therefore trialled. The Aqvist et al. [48] parameters are used to capture the majority of the desired behaviour, but the cation-controlling Na^+-O parameter from Akten et al. [49] is used.

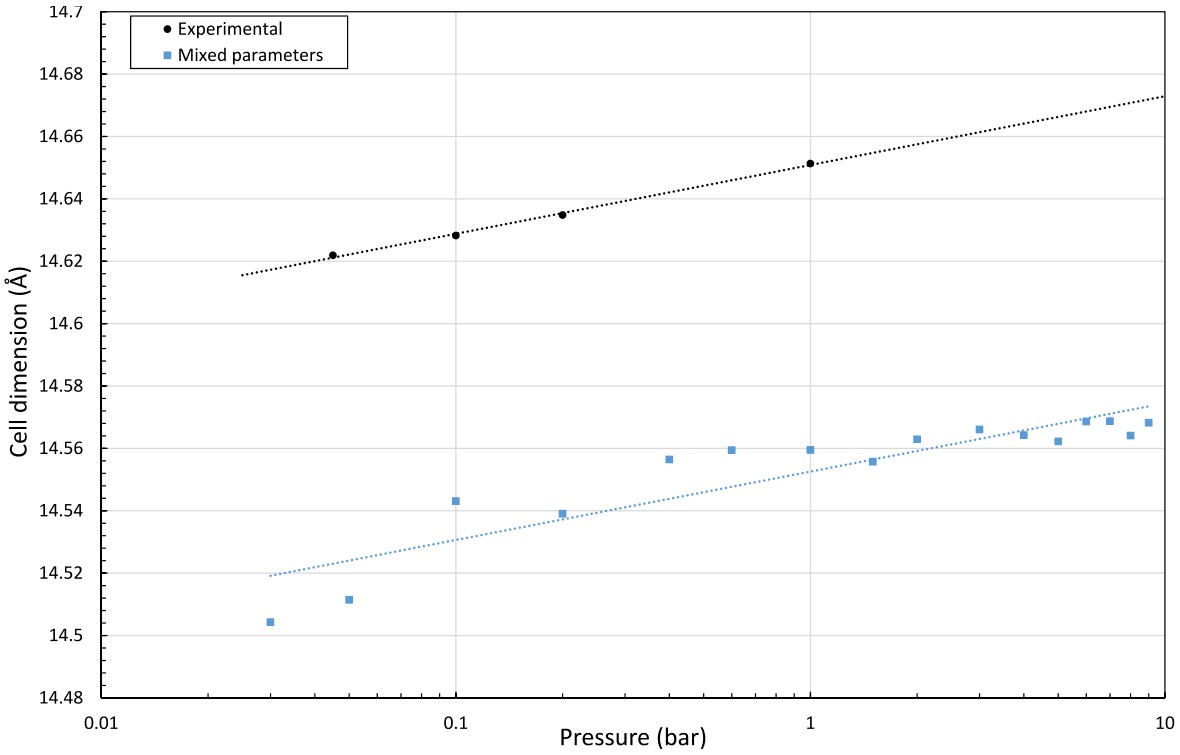

Figure 3.26: Cell expansion for Na-RHO with mixed Akten/Aqvist parameters

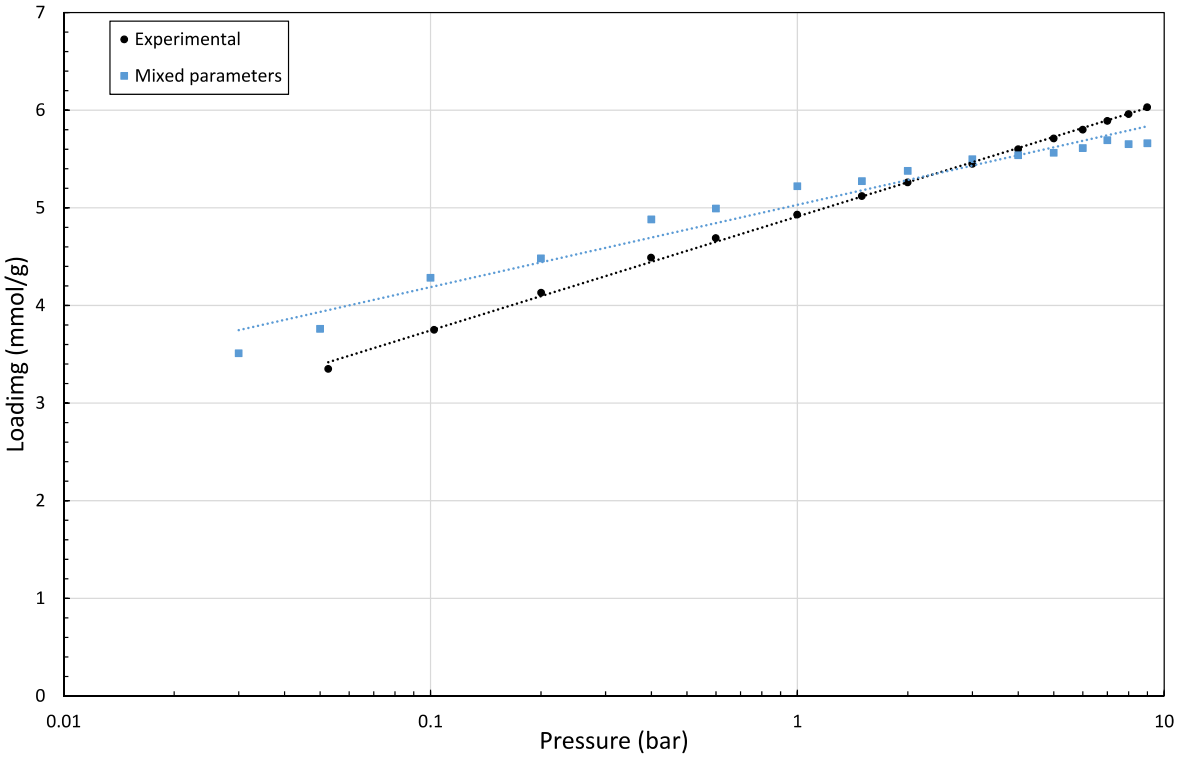

Figure 3.27: Adsorption isotherm for Na-RHO with mixed Akten/Aqvist parameters

These mixed parameters do not satisfy perfectly the cell expansion or the isotherm but capture all the main trends successfully. Most importantly, there is a close

match to the experimental cation positions (Table 3.16) both with and without CO_2 present. The unit cell length on CO_2 loading is offset by -0.1 Å but expands with the same gradient as the available experimental data (Figure 3.26). This does introduce a slight difference in the isotherm (Figure 3.27), particularly at higher loadings where the simulated data plateaus earlier (due both to the smaller cell and the choice of Lennard-Jones parameters).

Table 3.16: Cation sitings for Na-RHO with mixed Akten/Aqvist parameters

Sample	Type	cations per unit cell Site II (S8R)	cations per unit cell Site III (S6R)
Na-RHO	Experimental [7]	6.08	3.46
Na-RHO (1 bar CO_2)	Experimental [7]	6.00	3.92
Na-RHO	Simulated	5.625	4.125
Na-RHO (1 bar CO_2)	Simulated	5.125	4.625

3.7. Concluding remarks

In this chapter, the flexible zeolite forcefield by Gabrieli et al. [46] has been adjusted to reproduce key physical parameters of Na-RHO. In particular, a comparison between classical MD simulations and experimental/DFT simulations showed a difference in the Si-O-Si and Si-O-Al angles of around 15°. At room temperature, Na-RHO is acentric ($I\bar{4}3m$ symmetry), a feature that is markedly different from the centric LTA zeolites for which the forcefield is optimised. As a particular interest of this work is the behaviour of the windows, the parameters were adjusted to match more closely the window distortion of Na-RHO seen in DFT simulations at 300 K (Table 3.10).

Several important findings have arisen from a thorough investigation of the choice of cation parameters. Of particular note is the use of replica exchange molecular dynamics in predicting the cation positions. Both traditional NVT Monte Carlo and replica exchange Monte Carlo are insufficient to sample configuration space (Figure 3.6). In the case of traditional (single temperature) MC, the assumption of system ergodicity breaks down - the final cation positions are dependent on the starting position due to the high energy barriers that must be overcome for cation translation. This is partially overcome with REMC but sampling remains poor as the framework is held rigid. The relaxation that occurs between the cation and the framework, which is only captured in REMD (e.g. Figure 3.8) is particularly important for RHO type systems and even here, the cation transitions occur on the nanosecond scale. The following conditions are recommended as a minimum to check for cation convergence: 1 fs time step with replica exchange attempted every 1000 steps; a simulation length of at least 5 ns; and the use of a minimum of 96 replicas with temperatures clustered at lower temperatures [93]. Whilst computationally more demanding than standard molecular dynamics, these simulations are important to obtain the correct cation distribution and take only ≈4

hours to finish (simulations were run with GROMACS v2018.1, using 96 Intel Skylake 2.6 GHz cores and Intel 18.0.128 compilers).

A common approach to forcefield fitting is to adjust the Lennard-Jones parameters to reproduce an experimental isotherm [88]. Particular care must be taken with this approach in this case. Important to the modelling of RHO is the combined MC/MD scheme shown in Figure 3.3. If a set of Lennard-Jones parameters are fitted to a single RHO structure, no account is made for swelling of the framework on loading. Ideally, all GCMC simulations in flexible materials such as RHO would use a single software package utilising a hybrid MC/MD approach, although alternating between MC and MD packages is a reasonable compromise. This work has shown that at least three consecutive rounds of MC and MD are required to reach convergence.

When fitting a forcefield, the equilibrium cation sites will change if the Lennard-Jones parameters are adjusted. This is particularly true for the σ parameter (Figure 3.21). It is then necessary to run a new REMD simulation to ensure that the cations are again in a low energy configuration.

Another key concept identified here, which perhaps has been overlooked in the literature, is the importance of the 1-4 Coulombic exclusion policy. Most forcefields exclude completely the 1-2 (bond stretch) and 1-3 (bond bend) Coulombic interactions. The most commonly implemented 1-4 exclusion policies include complete exclusion of the Coulombic interactions in the CHARMM [64] forcefield, scaling the Coulombic interaction by 50% in OPLS-AA [94] or dividing the Coulombic interaction by 1.2 in AMBER [95]. This work has shown not only that the cell volume is sensitive to the 1-4 parameter but that even moderate adjustments of the scale factor can be used to control the unit cell dimension in an NPT simulation (Figure 3.2).

Some of this sensitivity could, potentially, be removed by adding bonded torsional terms to the forcefield. In a recent study [54], the simulated window distortion seen in pure silica 8MR zeolites was improved by adjusting the torsional terms in the Hill-Sauer forcefield [51]. The aim there was similar to that in Section 3.6.2 where the T-O-T angles (amongst others) were adjusted to improve the window distortion.

Overall, a reasonable compromise has been reached between the three main factors of interest: cell expansion, isotherm prediction and cation positioning. The parameters here are not fully optimised but provide a reasonable starting point to gain an understanding into the trapdoor mechanism. Additional steps that could be taken to optimise the forcefield are discussed in the Future Work section (Chapter 7).

4. CO_2 diffusion mechanism in Na-RHO.

4.1. Preface

This chapter focusses on the underlying trapdoor mechanism seen for CO_2 in Na-RHO. In Chapter 3, it was shown that cations lie in a deep energy well (Figure 3.11) and once in place, the cations do not readily move from these positions. As intercage diffusion of CO_2 is observed experimentally however, it is anticipated that CO_2 molecules must flatten this energy well allowing cations to move slightly away from their sentry position so that periodically a CO_2 molecule can pass through the D8R. In this section, the energy barrier required for intercage CO_2 diffusion (both with and without a cation present) is found and then, the underlying diffusion mechanism is examined.

In this chapter, the forcefield parameters from the final part of Chapter 3 are used with the resulting mechanism for CO_2 diffusion uncovered from 1 μs classical MD runs.

4.2. Background

There are two mechanisms proposed for the trapdoor motion in the literature, cation gating [8] and swinging doors [45] but neither have been tested via classical simulation methods. The cation-gating [8] mechanism is suggested from experimental observations and the swinging doors [45] mechanism via QM calculations (therefore only on very short timescales).

In the cation gating mechanism [8] (Figure 4.1), CO_2 is thought to diffuse via the following pathway:

1. A CO_2 molecule approaches a cation occupied S8R (diagram 1).
2. The CO_2 molecule pushes the S8R cation through the D8R to the next S8R (diagram 2).

3. As the CO_2 passes into the D8R, a cation from an adjacent 6MR is pulled along with the CO_2. The cation which has just moved into a new S8R is pushed out to an empty 6MR (diagram 3).
4. The final result is similar to diagram 1, one cation has moved from a 6MR to a S8R and one cation in a S8R has moved to a 6MR (diagram 4).

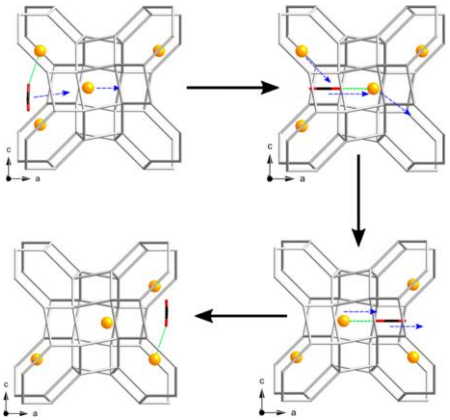

Figure 4.1: Cation gating mechanism [8] Reprinted with permission from Journal of the American Chemical Society. Copyright 2012. American Chemical Society.

The cation gating mechanism [8] in Figure 4.1 is based on two key concepts. The first is that CO_2 cannot diffuse through a S8R if a cation is present in the ring. The cation must therefore move away from its equilibrium site for CO_2 diffusion to occur. The second concept is that the cation occupancies do not change substantially before and after adsorption of CO_2 (Table 3.16). There should not therefore be a net change in cation occupancies.

The swinging door mechanism [45] proposes an alternative mechanism for the selective uptake of CO_2. Instead of the CO_2 having a direct interaction with the cation, selective uptake is attributed to random thermal motion of the cations. This thermal motion allows small, polar molecules to creep through the D8R when the cation leaves the immediate vicinity of the S8R. Larger, non-polar molecules (e.g. methane) are unable to take advantage of this relatively small change in cation position and do not transition into the D8R.

In the swinging door study [45], *ab initio* molecular dynamics (AIMD) was used to show that Na^+ cations in RHO are typically found within a 1 Å radius of their average position. As a result of thermally induced lattice vibrations, the 8MR cations periodically move beyond their equilibrium position and it is suggested that the diffusion of CO_2 through a D8R occurs only when a cation undergoes one of these movements.

In the study [45] this was investigated further by using constrained AIMD (Figure 4.2b). In these simulations, the x-coordinate of a cation is held constant but the cation is allowed to move in the y-z plane.

First, the cation is placed at points along a path between two coordinates, one in the S8R and the other in line with a neighbouring 6MR (Figure 4.2a). The energy to keep the cation constrained at points along this path is then found (Figure 4.2b). The energy pathway is found not to change substantially in the presence of CO_2 (6.7 kcal/mol without CO_2 vs 7 kcal/mol with CO_2).

The study [45] is then extended fixing the cation in turn at the start and end point along the path. The energy required to keep the cation in position is then calculated as a CO_2 molecule passes through the D8R. Here, the energy required for CO_2 diffusion is reduced by one half when a cation is located just outside of the ring (Figure 4.2c). From these findings, the gating mechanism is likened to a swinging saloon door where once the cation moves just away from the ring (the saloon door is open), the energy barrier is reduced and a CO_2 molecule can diffuse through. When the cation is firmly in the S8R (the saloon door is closed), no diffusion occurs.

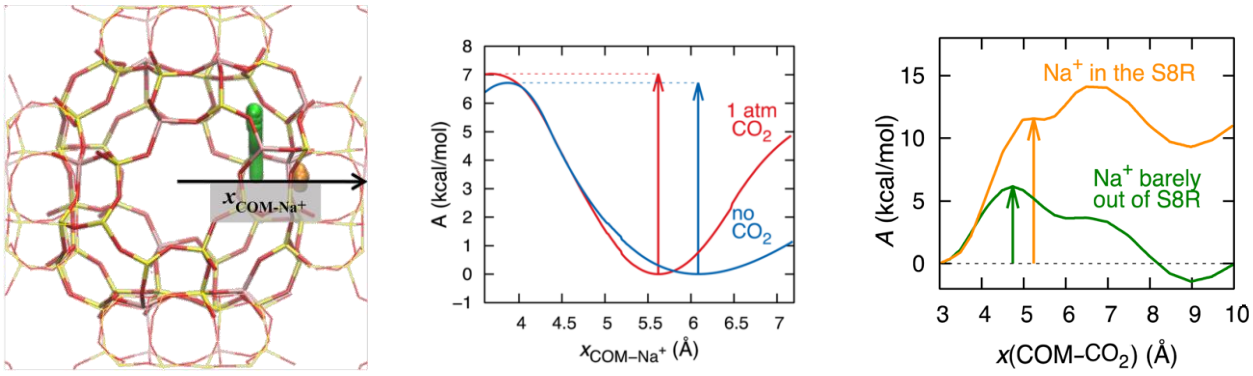

a) Green cation at x = 4.68 Å, orange cation at x =5.76 Å

b) Energy barriers for cation movement

c) Energy barriers for CO_2 movement with constrained cation position

Figure 4.2: Free energy work by [45] Reprinted/Adapted with permission from Chemistry of Materials. Copyright 2017. American Chemical Society.

4.3. Free energy calculation

To characterise the energy barrier for CO_2 diffusion between two *lta* cages in this work, a free energy approach is chosen which does not perturb the dynamics of the system. This is possible due to the longer timescales examined in classical simulations and is based on similar work studying the diffusion of ethene in 8-ring zeolites [96].

Equation (4.1) links the microscopic probability of finding a particle at a given position, p, with the macroscopic free energy F.

$$F = - kT \ln p \qquad (4.1)$$

The free energy at every point in space can be calculated by dividing the simulation box into small cubelets and then calculating the probability of finding a molecule of CO_2 in each cubelet. If the centre of mass of a molecule (the carbon atom in the case of CO_2) is within a given cubelet, the value associated with that cubelet is incremented by unity. If a long MD run is performed, lasting several hundred nanoseconds, the probability of finding a molecule at any given point in space can be found by dividing the value of each cubelet by the sum of all cubelets.

To evaluate the change in free energy for a move across a D8R, each point in the ring is projected onto a 1D ξ-axis (Figure 4.3). CO_2 molecules are only projected onto the ξ-axis if they lie within a critical distance - chosen arbitrarily as 7 Å between the carbon atom and the D8R centre of mass to cover both the D8R and the approach of a CO_2 molecule to the D8R.

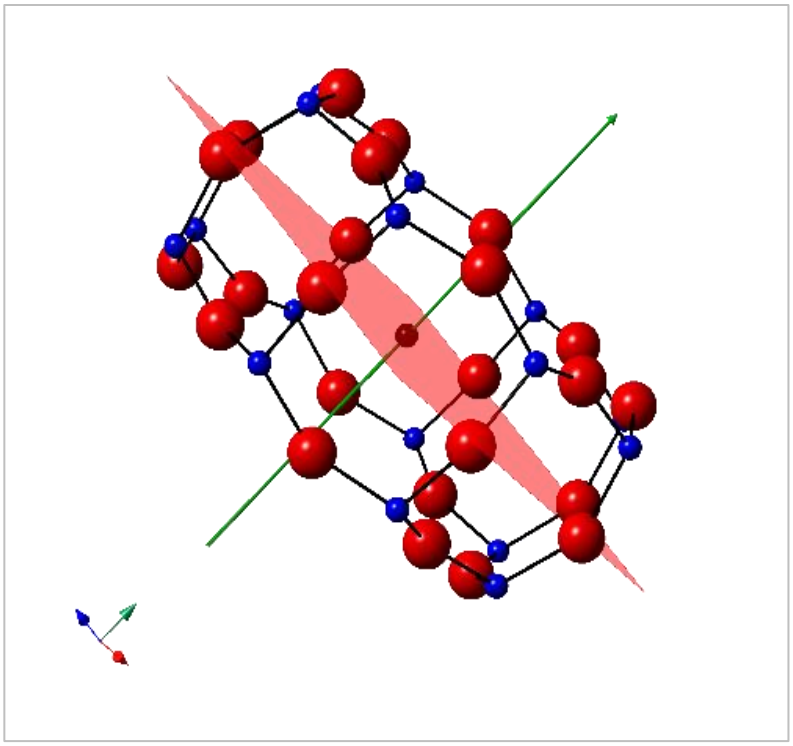

Figure 4.3: D8R with plane (red), 1D ξ-axis (green) and origin (black). The entry and exit points of the green axis with the D8R correspond to approximately -1.9 Å and +1.9 Å respectively

The ξ-axis is found by finding the normal to a plane of best fit calculated from all of the atoms inside the D8R. The plane chosen represents the (001) Miller index in the standard $Im\bar{3}m$ or $I\bar{4}3m$ crystallographic representation of RHO.

As the plane of best fit through a D8R will always be similar to the xy, xz, or yz planes, additional care must be taken when fitting the plane. When the plane lies in one of these coordinate planes, one of the first three coefficients (a, b or c) in Equation (4.2) will be zero.

$$ax + by + cz + d = 0 \tag{4.2}$$

The general form of a plane may be expressed in Equation (4.2). If this is rearranged to a form, such as that used during fitting, where the coefficient in the denominator becomes very small (e.g. Equation (4.3)), the system becomes ill conditioned.

$$x = \frac{-(by + cz + d)}{a} \tag{4.3}$$

For this reason principal component analysis is used to determine which two directions show the greatest change and the corresponding coefficients in these directions are fitted first [97]. The problem overcome here is related only to computational difficulties in handling very small numbers with high precision.

The origin on the axis is defined as the intersection of the normal to the plane of best fit with the average of all D8R coordinates (the D8R centre of mass). Where it is necessary to distinguish between the positive and negative ξ directions, the positive direction is taken as the side on which a cation sits. For an empty ring, the normal to the ring points predominantly in the direction of one of the principal axes and the positive direction is aligned accordingly with that of the simulation box.

Figure 4.4 shows an estimate of the energy barriers required for a CO_2 molecule to diffuse both past a Na^+ cation and through an unoccupied ring. The energy barrier that must be overcome for diffusion through an unoccupied ring is ≈4 kT, whereas diffusion through a ring with a cation is ≈9 kT. At 300 K, this corresponds to a Boltzmann factor of 0.05 and 0.0025 respectively. This is in good agreement with Figure 4.2c [45] which showed that the energy barrier for CO_2 diffusion was reduced by half when the cation was displaced from its equilibrium S8R position.

There is a substantial change in the energy barrier when the cation is present. In the unoccupied D8R, the energy barrier is symmetrical, with the two energy wells at ≈ ±2.0 Å corresponding to the edge of the D8R. The higher ≈4 kT barrier which

must be overcome here is required to push the CO_2 into/out of the D8R. Once the CO_2 molecule is in the D8R, it exists in a higher energy state (≈3 kT) due to interactions with the nearby framework atoms.

In the occupied state, the energy barrier is raised substantially when the cation is placed at +2.0 Å (≈9 kT). The presence of the cation also increases the energy barrier on approach to the D8R from –ξ (from ≈4 kT to ≈6 kT).

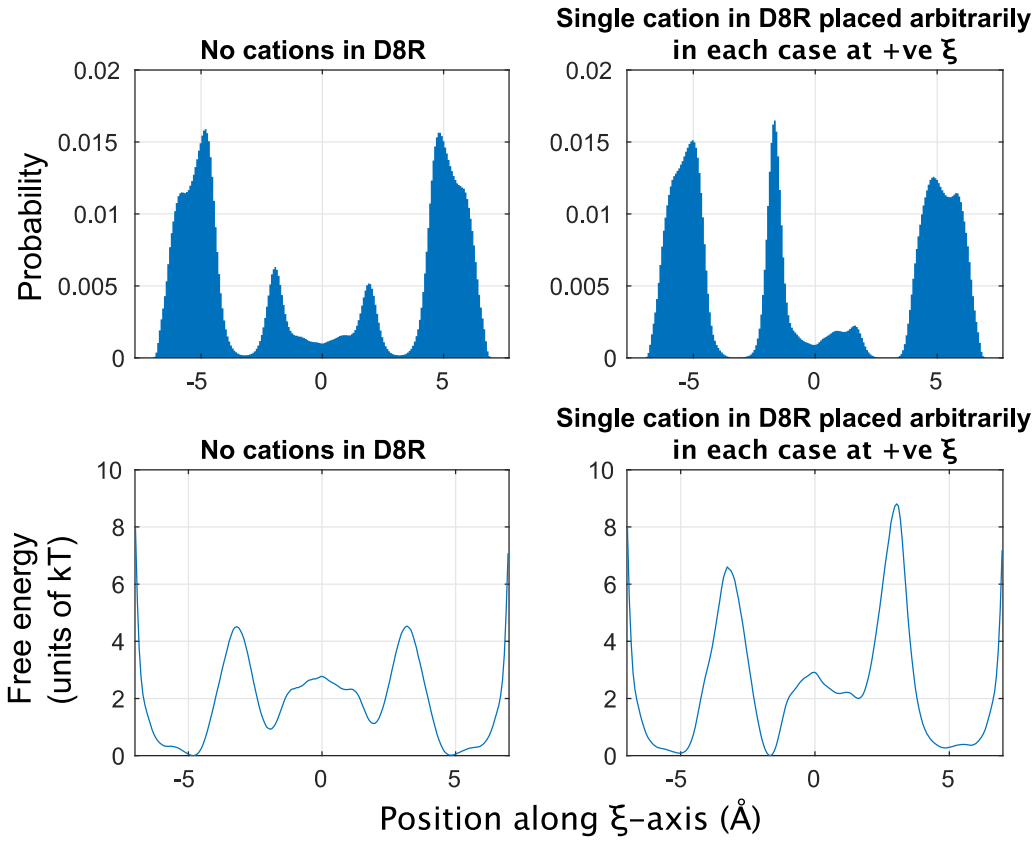

Figure 4.4: Free energy and probability diagrams for CO_2 diffusion at 600 K.

4.4. CO_2 diffusion mechanism proposed in this work

From 1 μs NVT runs, the diffusion pathway for intercage CO_2 transport is found to closely resemble the cation-gating mechanism [8] shown in Figure 4.1. It should be noted that despite the efforts of Chapter 3 to optimise the forcefield, a discrepancy remains in that unlike the experimental work that was undertaken at 298 K [8], in the MD simulation, a temperature of at least 400 K is required to observe intercage diffusion of CO_2 molecules. For the simulations presented here, a temperature of 600 K is used so that more substantial diffusion rates are observed.

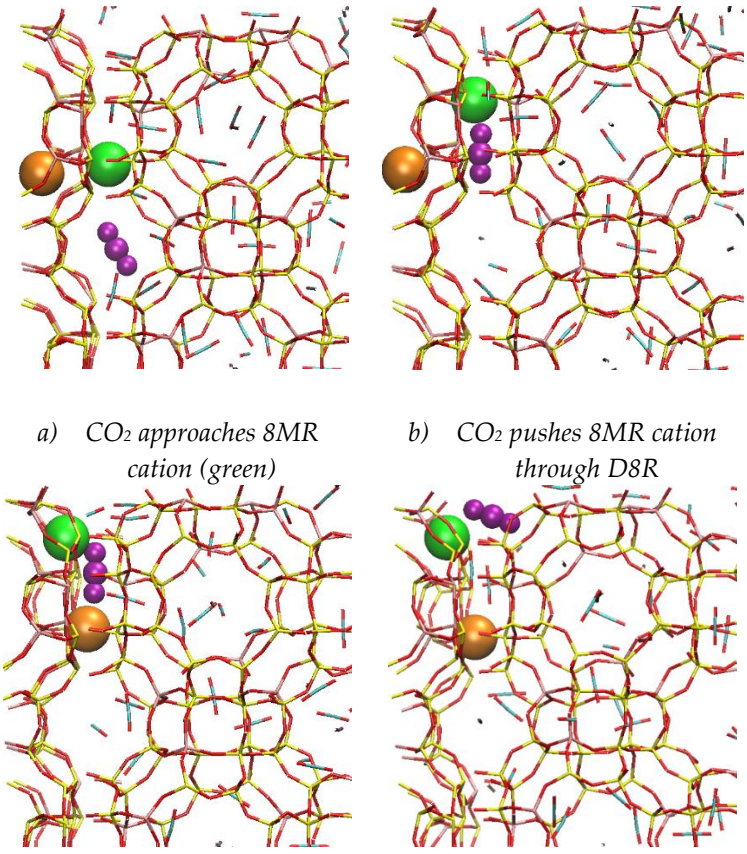

a) CO_2 approaches 8MR cation (green)

b) CO_2 pushes 8MR cation through D8R

c) 6MR cation (orange) snaps into S8R site

d) CO_2 released

Figure 4.5: Snapshots from a NVT MD simulation showing the observed trapdoor mechanism at 600 K. Highlighted in green is a cation which starts in an 8MR, highlighted in orange is a cation which starts in a 6MR and highlighted in purple is a CO_2 molecule which transitions through the D8R. Shown as blue and red sticks are the other CO_2 molecules in the simulation. The remaining 76 cations are hidden for clarity but are present in the simulation.

Figure 4.5 shows excellent agreement with the proposed theoretical mechanism [8] (Figure 4.1). The CO_2 molecule of interest, coloured in purple, approaches an 8MR cation (green) and then the CO_2 molecule pushes the cation through the D8R. As the 8MR cation exits the D8R it fills the space of an empty 6MR.

The vacant D8R is an energetically favourable position for a cation and as the CO_2 passes through the 8MR, it is followed by a 6MR cation (until the cation reaches the 8MR). There is a ≈4 kT barrier which must be overcome for the CO_2 molecule to diffuse from the *lta* cage into the D8R and this cation motion helps hold the CO_2 in place between Figure 4.5b and Figure 4.5c so that the CO_2 molecule proceeds through the D8R (rather than reverse direction).

To quantify the diffusion pathway of CO_2 through the D8R, the angle between each transitioning CO_2 molecule and its corresponding ring is measured. To calculate the line of best fit through the CO_2 molecule, orthogonal regression is used rather than a standard least squares fit (Figure 4.6). In least squares regression, the distance between the points and the line is minimised, typically in the y-direction. In orthogonal regression [98], the shortest distance between the points and the line is considered in all three directions. When fitting a line through a CO_2 molecule where the molecule is flexible and each atom can move in each of the three dimensions, orthogonal regression is therefore most appropriate.

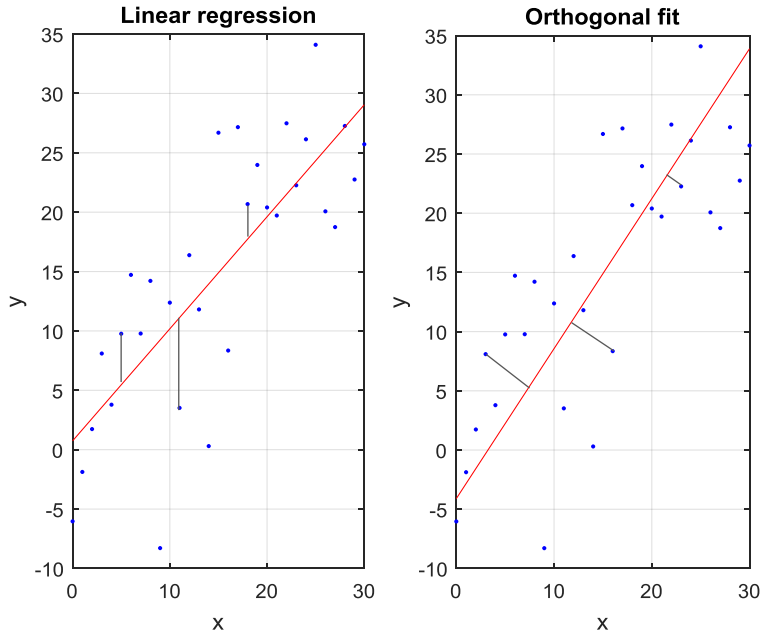

Figure 4.6: Difference between orthogonal and least squares linear regression.

To calculate the angle between the two lines the definition of the dot product is used:

$$\cos\theta = \frac{\boldsymbol{a}\cdot\boldsymbol{b}}{|\boldsymbol{a}||\boldsymbol{b}|} \tag{4.4}$$

where **a** and **b** are defined as vectors describing the normal through the D8R and the line of best fit through a CO_2 molecule of interest.

Figure 4.7 shows the angles made with the D8R normal for all individual CO_2 molecules in a 7 Å radius of the COM of a D8R collated during a 1 μs run with an output frequency of 10 ps.

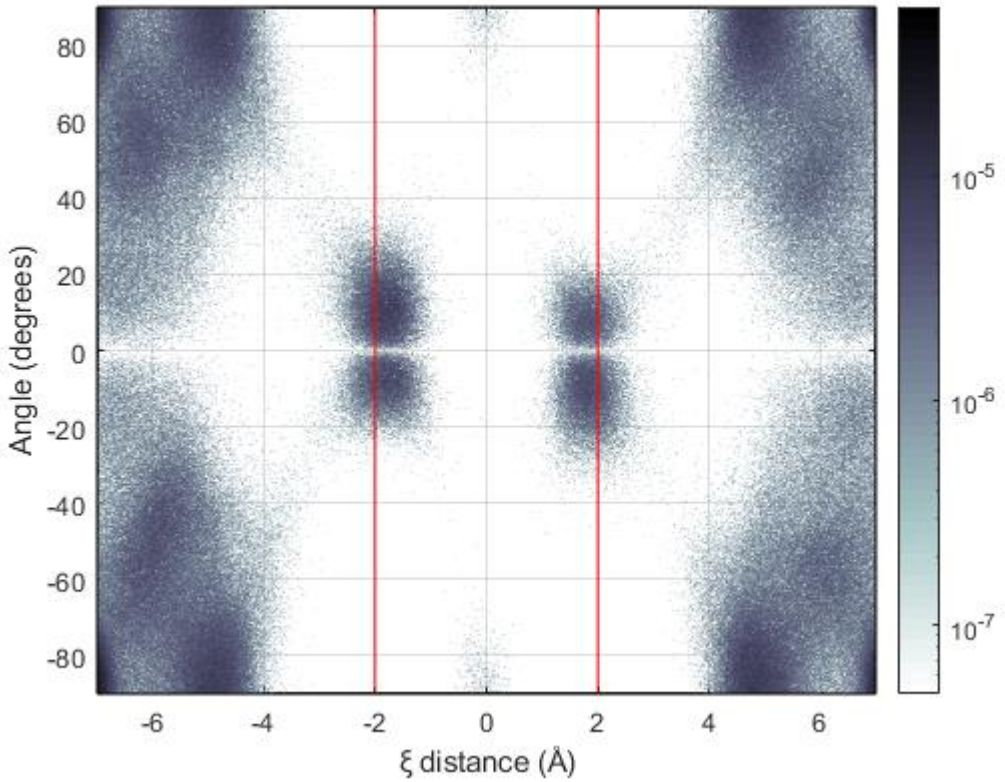

Figure 4.7: Alignment of CO_2 when diffusing through a D8R (D8R marked with solid lines). Data points are obtained by examining frames every 1 ps for 1 μs with the colorbar indicating the probability of finding a molecule at a given position and angle relative to the normal of the D8R plane through which the CO_2 molecule passes.

Figure 4.7 shows two peaks within the D8R. The first set of peaks D8R (at ξ = ±2 Å) is constrained to angles within ± 20° of the normal and indicates the mechanism via which CO_2 enters and exits the D8R. This shows that there is a particular preference for the CO_2 to enter slightly angled rather than at zero degrees. Once past the first S8R, a CO_2 molecule quickly diffuses through to the opposite S8R (in the D8R).

There is a second, albeit much fainter peak between +70 & +90 °and -70 & -90 (at ξ = 0). A closer examination of the trajectories revealed this was related to a second, less frequently observed, diffusion pathway occurring when no gating cation is present in the D8R.

Figure 4.8 and Figure 4.9 show the diffusion mechanism observed with and without a gating cation present in the D8R. When there is no gating cation present

in a D8R, the CO_2 molecule enters normal to the plane (Figure 4.9a and Figure 4.9b). Once all three atoms have crossed the first S8R, the most favourable position for the molecule is perpendicular to the normal (Figure 4.9c). To exit the D8R, the CO_2 molecule returns to an orientation in line with the normal to the plane as soon as the first atom oxygen atom in CO_2 crosses the second S8R.

CO_2 mechanism with cations

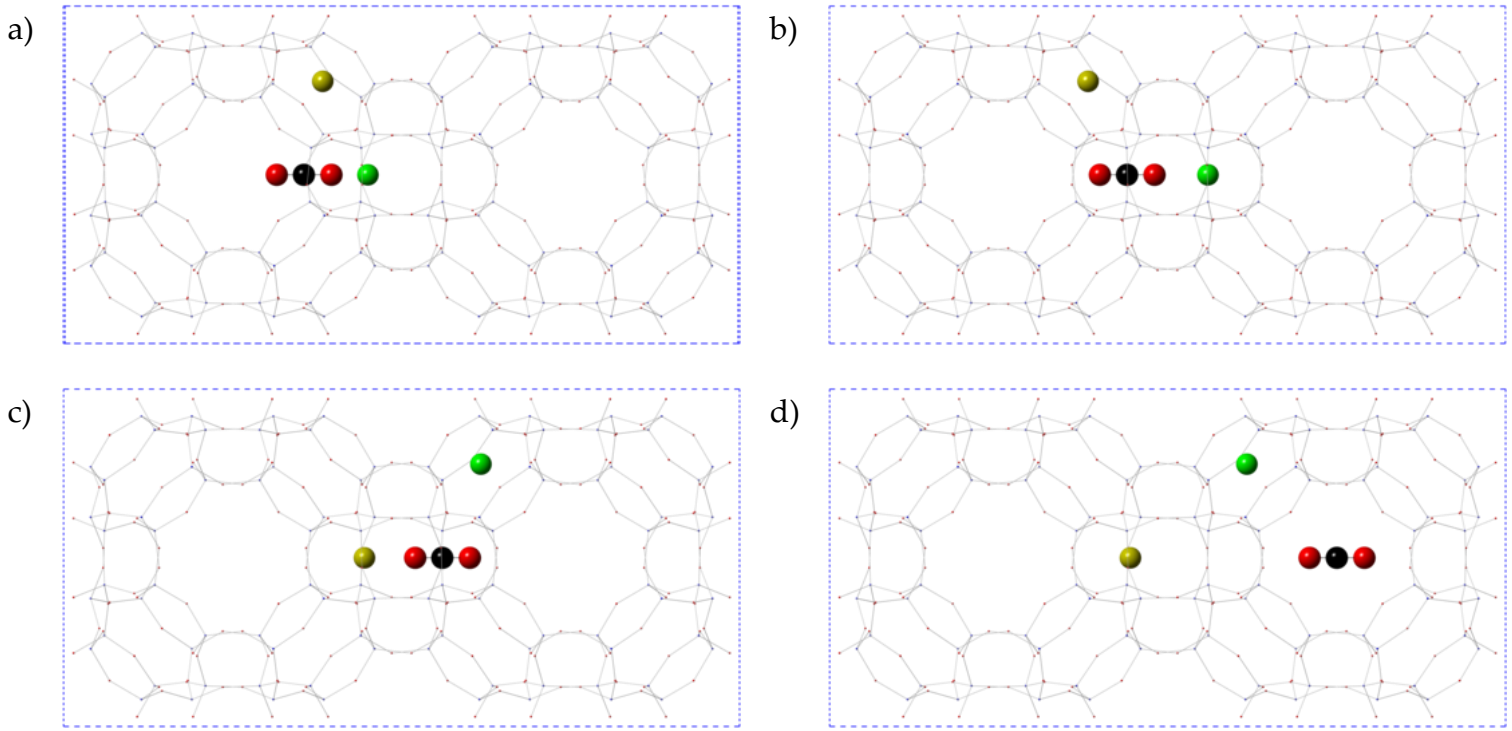

Figure 4.8: Schematic for the CO_2 mechanism through a D8R in the presence of a gating cation.

CO_2 diffusion mechanism with no cations

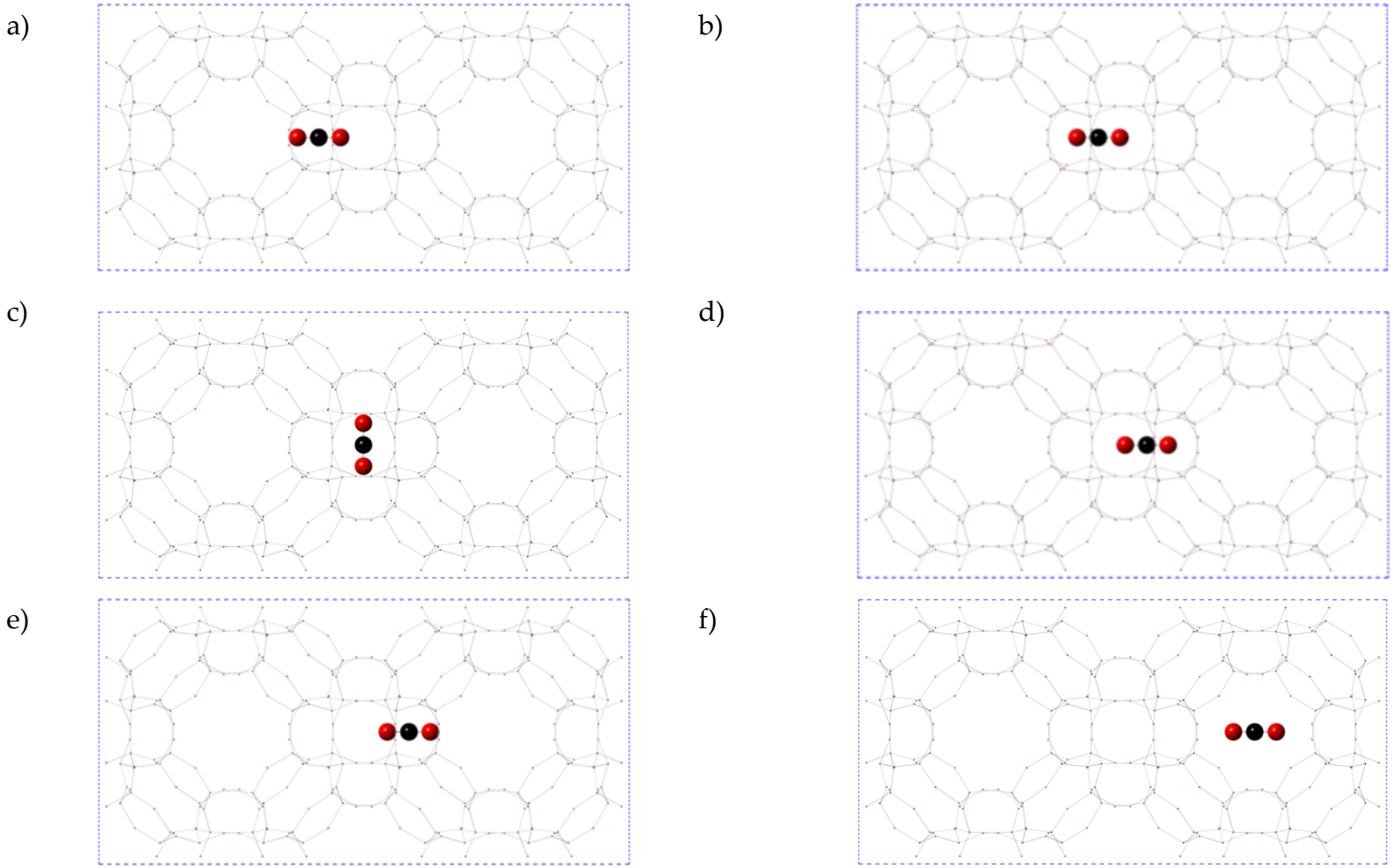

Figure 4.9: Schematic for the CO_2 mechanism through a D8R in the absence of a gating cation.

4.5. Diffusion rates

The diffusion of a CO_2 molecule can be calculated, as described in Section 2.4.5 by plotting the mean square displacement against time from a long MD simulation. If the plot is linear, the diffusion coefficient can be calculated from Equation (2.62). For these simulations the equilibrium loading from the 1 bar simulation at 300 K is used (129 molecules/ 2 x 2 x 2 supercell) and the MD simulation is then run at 600 K.

Figure 4.10 shows how the mean squared displacement (msd) varies with time and the result of a linear fit through the simulation points for temperatures between 300 K and 600 K. The first 10 ns are excluded from the graphs to allow for equilibration. The remaining simulation points up to 1 μs are then used (with a data point output every 10 ps). Even with an equilibrated period accounted for, the fits are clearly non-linear at the start. This is a result of the CO_2 molecules being confined to cages. Initially the molecules are able to explore their occupying cage rapidly so a steep change in gradient is seen. Intercage diffusion takes longer however and so once the initial cage is explored, the rate of change of the msd reduces. With higher temperatures (more kinetic energy) the probability of crossing a D8R increases and so the rate of change of msd is higher (hence the different scales on the y axes of the four plots).

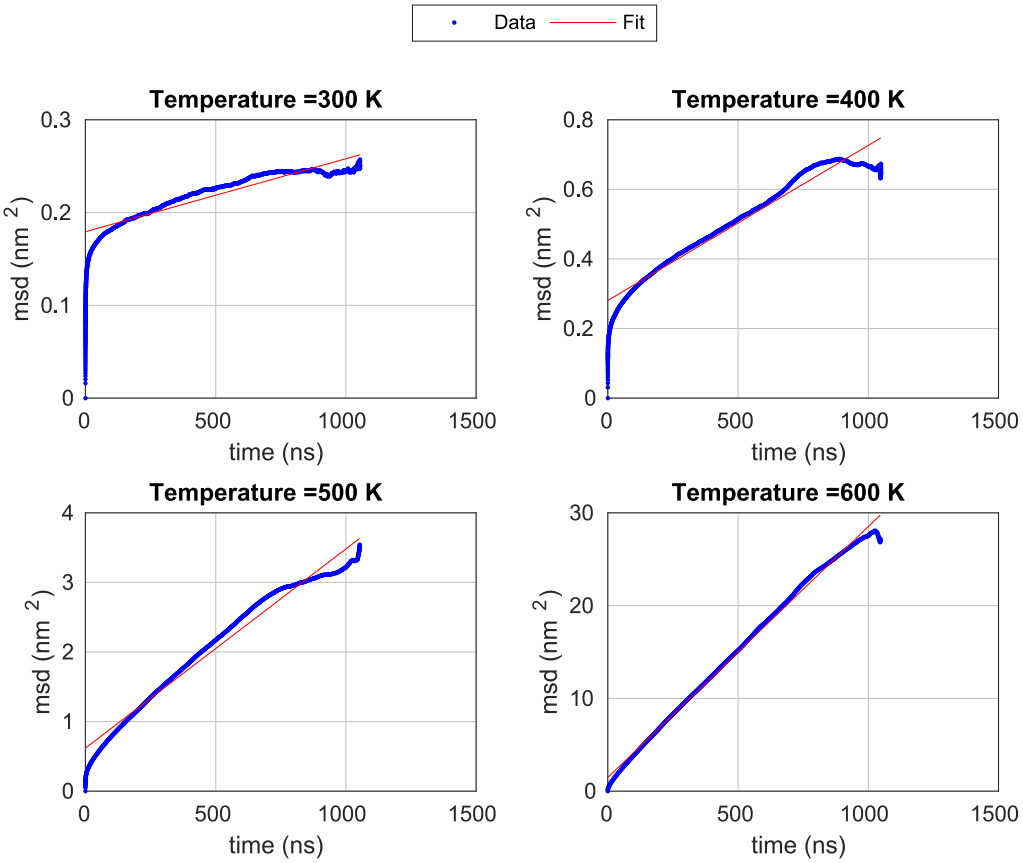

Figure 4.10: Mean squared displacement (msd) for CO_2 in Na-RHO between 300 K and 600 K.

To calculate the self-diffusion coefficient from Equation (2.62) the linear fit should, formally, pass through the origin. As described in Section 2.4.5, the diffusion coefficient can then be calculated from the gradient of the line. In the case of Figure 4.10, the fits are offset slightly from the origin due to the increased speed at which the first unit cell is explored. In terms of the msd, this faster rate of exploration takes up only a very small fraction of the total simulation time so the overall effect on the gradient is minimal. Table 4.1 therefore shows the diffusion rates calculated taking into account only the gradient of the line of best fit. This shows that the CO_2 diffusion rate increases by two orders of magnitude between 300 K and 600 K.

Table 4.1: Self-diffusion coefficients for 129 molecules of CO_2

Temperature (K)	Gradient (x 10^8 cm^2/s)	Estimate of D (x 10^9 cm^2/s)
300	0.0786	0.001
400	0.4457	0.006
500	2.861	0.037
600	27.0524	0.3495

This confined diffusion [99], where molecules periodically jump from cage to cage is better described using Equation (4.5).

$$\langle r^2 \rangle \approx \langle r^2 \rangle_0 \left[1 - \exp\left(\frac{t}{\tau}\right)\right] \tag{4.5}$$

The fit can be improved further by adding an additional fitting parameter, c, (Equation (4.6)).

$$\langle r^2 \rangle \approx a^2 \left[1 - \exp\left(\frac{-t}{\tau}\right)\right]^c \tag{4.6}$$

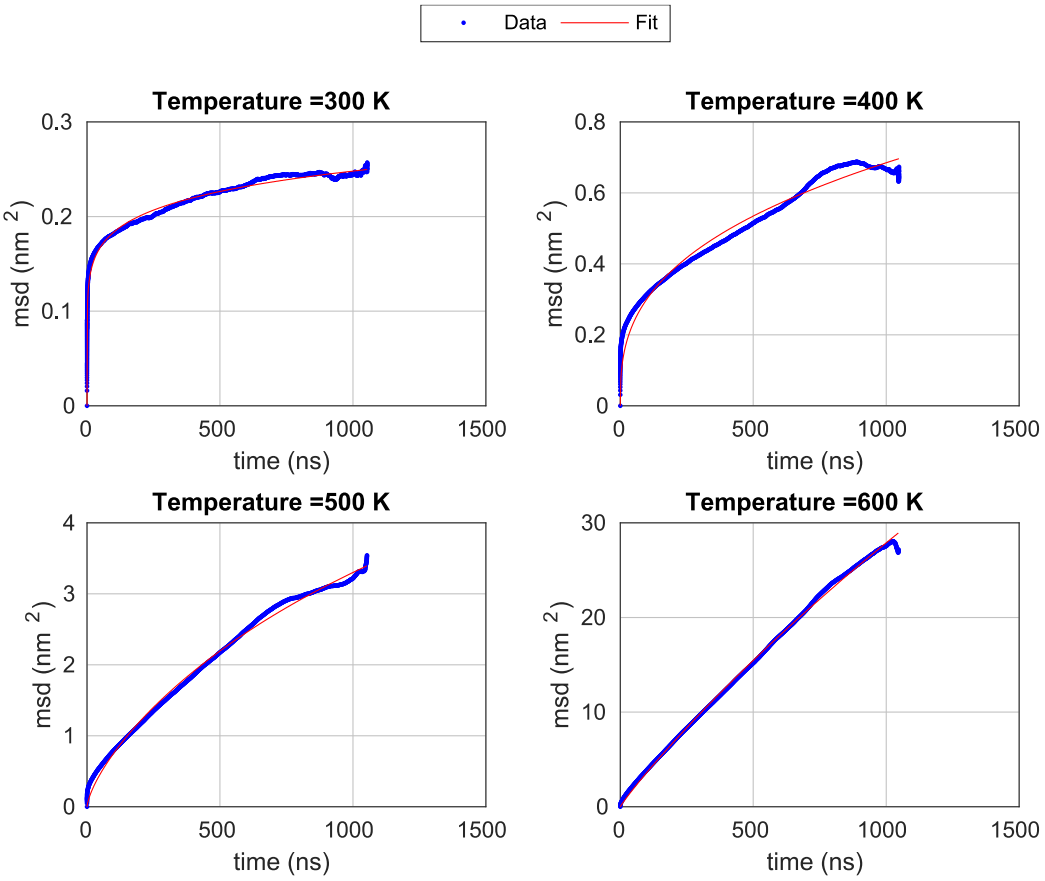

Figure 4.11: Mean squared displacement fitted with Equation (4.6)

Fitting the evolution of the mean squared displacement with Equation (4.6) gives an improved fit over the linear description used in Figure 4.10. This fit can also be used to describe consistently the full range of behaviour across all four temperatures.

The disadvantage of fitting the mean square displacement with Equation (4.6) is that the diffusion rate becomes time-dependent so a self-diffusion coefficient can't

be calculated from this model. However, the coefficients in Table 4.2 still provide useful information. The *a* parameter gives an indication of how far the particle will reach (the size of the domain) at infinite time and the tau parameter an indication of the time required to reach that plateau. For example, at 300 K, the value of *a* is 7.2 Å. This corresponds to the displacement seen by an average particle located at the centre of a single *lta* cage (N_{cells} = 1) of width 14.4 Å. The N_{cells} value in Table 4.2, describes the number of cells explored by an average CO_2 molecule. This gives a rough diffusion rate (the number of cells crossed per microsecond).

Table 4.2: Coefficients in Equation (4.6)

Temperature (K)	a^2 (nm^2)	tau (ns)	*c*	*a* (Å)	N_{cells}
300	0.5204	284291	0.1311	7.2	1.0
400	6.309	496714	0.3575	25.1	3.5
500	6.3744	1990	0.7089	25.2	3.5
600	116.2614	4132	0.9289	107.8	15.0

Table 4.2 shows that at 300 K, intercage CO_2 diffusion does not occur (N_{cells} = 1). This provides evidence of a critical admission temperature [6], below which the cations do not move from their equilibrium positions. As the temperature is raised to 400 K and 500 K, CO_2 is able to diffuse between cages and this occurs at an increased rate with increasing temperature (tau decreases). At 600 K, the cations are more mobile and the CO_2 molecules have sufficient energy to diffuse more readily through the D8R (N_{cells} = 15).

4.6. Concluding remarks

In this chapter, the mechanism of CO_2 diffusion in Na-RHO has been studied with classical MD for the first time. There are two mechanisms found for CO_2 diffusion in Na-RHO. In the most common case, where there is a cation present, a CO_2 molecule enters and remains normal to the plane of the D8R for the duration of the transition. In the more uncommon case where there is temporarily no blocking cation present, the CO_2 rotates 90° normal to the ring in an intermediate state between the two S8Rs. Although more uncommon, the energetic penalty for diffusion through an unoccupied ring is 4 kT as opposed to 9 kT when a cation is present. This is in agreement with the swinging door [45] study which also found that the energy barrier halved when a cation moved out of the window (Figure 4.2c).

This study also supports the trapdoor mechanism, which suggests that cations indeed act as gate-keeping sentries. Figure 4.5 shows that an 8MR cation moves out of the way of a CO_2 by pushing a cation through a D8R and into an empty 6MR on the other side of an *lta* cage. In doing so, an adjacent 6MR cation moves from the 6MR into an 8MR. This ensures that a gate-keeping cation is still present after the CO_2 molecule has diffused through the D8R.

It should be re-stressed that experimentally, diffusion is seen at 300 K whereas in the simulation a temperature of 600 K is needed for substantial CO_2 diffusion. This indicates that whilst the adjusted forcefield parameters can be useful for gaining a preliminary understanding of the underlying mechanism, further optimisation of the parameters is required before predicting diffusion coefficients useful for design in process engineering applications.

5. Application of Na-RHO to the adsorption of other gases

5.1. Preface

Having developed a methodology to model Na-RHO with adsorbed CO_2, it is interesting to extend the simulations to other gases. This section begins by first introducing the three separations of interest: the separation of noble gases (He, Kr, Ar and Xe), the purification of air (O_2/ N_2) and the separation of CH_4 and CO_2.

Next, the type I Langmuir isotherm is introduced. For the majority of gases examined, this is a convenient means of interpolating between points when finding the heat of adsorption. (The heat of adsorption is one of the three main criteria outlined in Chapter 1 for assessing whether a porous material will be suitable for a given separation.)

Finally, a combination of MC and MD simulations are used to evaluate Na-RHO as a potential adsorbent for the three separations. Here, both the adsorption isotherms and the rates of gas diffusion in Na-RHO are considered. Full details of the simulation parameters used are provided in Appendices A-D.

5.2. Background

5.2.1. Separation of noble gases

Perhaps one of the first descriptions of a cation trapdoor system in a zeolite comes from the controlled trapping and release of Xe in Cd-RHO [39]. As mentioned briefly in Section 3.6.3, when Cd-RHO is heated, Cd^{2+} cations move from the S8R position to occupy the S6R sites. This causes an expansion in the length of the unit cell from 14.5 to 15.0 Å. The combination of the cations moving away from their sentinel 8MR positions and the resulting expansion of the unit cell allows Xe to diffuse into the structure [39]. When the structure is cooled, the Cd^{2+} ions return to the S8R, trapping the Xe in the pores [39]. Similar cation behaviour is not seen for

Na^+ (see Section 3.6.3 and literature [39]) but Na-RHO is still of interest for standard cation-gating separation.

In general, the extraction and separation of He, Ar, Kr and Xe from air is challenging. The noble gases are inert, uncharged single atom molecules and due to their chemical similarity, there is little to distinguish them from each other as they pass through an adsorbent. (Separation occurs generally due to a difference in size and strength of the van der Waals interactions). In addition, the noble gases are present in only low atmospheric concentrations (Xe = 0.0087 ppmv, Kr = 1.14 ppmv, He = 5.2 ppmv and Ar = 10,000 ppmv) [100] making their separation from bulk air more challenging.

Despite their low naturally occurring concentrations, the noble gases find widespread use. Xe is used in fluorescent tube lighting [101], hospital MRI (Magnetic Resonance Imaging) scans [102] and anaesthesia [103] and is valued at about $5000/kg [100]. Ar is used in fire-extinguishers [104], for treating lesions found during medical endoscopies [105] and arc-welding [106]. Radioactive forms of both ^{135}Xe and ^{85}Kr are produced in nuclear fission and must be captured as part of nuclear reprocessing [100].

5.2.2. Separation of O_2/N_2

Oxygen and Nitrogen are also valuable as purified gases. The separation of O_2 from N_2 is traditionally accomplished via cryogenic distillation, although with suitable materials, it is also possible through adsorption [107] and membrane separation [108].

In power-generation plants using oxyfuel combustion, an enriched oxygen supply is used to achieve complete combustion [107]. This enriched stream is formed by mixing the oxygen stream from an air separation unit with recycled flue/exhaust gas from combustion [109]. The end result is a flue stream consisting predominantly of CO_2 and H_2O. These can be separated easily from each other by condensation

then further drying, leaving behind a CO_2 rich steam that can be used for sequestration [107]. Enriched oxygen is also used in welding [110], steel production [110] and in hospitals to treat carbon monoxide poisoning [111].

One of the highest tonnage uses of N_2 is in the production of NH_3 for fertiliser in the Haber process - more than 100 million tons of NH_3 were produced in 2010 [112]. As nitrogen is relatively inert, it is also used as a blanketing agent for tanks containing flammable liquid and for purging empty vessels [4]. Liquefied N_2 is also widely used as a coolant [4].

5.2.3. Separation of CO_2/CH_4

The separation of CO_2 and CH_4 is particularly important in the field of gas processing. Gas wells can contain up to 70% CO_2 by volume [113]. This is exacerbated when CO_2 is pumped into the well during Enhanced Gas Recovery [114]. In both cases, a large fraction of CO_2 must be extracted from the desired CH_4 to produce a fuel rich stream.

CO_2 and CH_4 are also produced together by microorganisms at landfill sites [115]. This represents a major source of CH_4 emissions and there is significant interest in capturing the CH_4 produced, both as a fuel source and to stop emission to the atmosphere [115].

5.3. The Langmuir isotherm

If the adsorption of a gas in a zeolite follows a standard 'Type I' isotherm [116], it is possible to model the adsorption process using a Langmuir model (Equation (5.1)). This described the loading, q, as a function of the pressure P. The q_{sat} parameter describes the saturation loading at infinite pressure and the Langmuir b parameter introduces a temperature dependency.

$$q = q_{sat}\frac{bP}{1+bP} \tag{5.1}$$

In the limit of infinitely low pressure, Equation (5.1) generates the Henry constant (K_H in Equation (5.2)) which is a useful initial measure of a material's ability to adsorb a gas [117].

$$K_H = \lim_{P\to 0}\left(\frac{dq}{dP}\right) = q_{sat}b \tag{5.2}$$

Once an isotherm has been generated, it can be replotted using Equation (5.3) and (5.4). If the Langmuir model holds, the isotherm will be linear and the values of b and q_{sat} can be obtained from the gradient and intercept of a line of best fit.

(HP)
$$\frac{P}{q} = \frac{1}{q_{sat}}P + \frac{1}{q_{sat}b} \tag{5.3}$$

(LP)
$$\frac{1}{q} = \frac{1}{bq_{sat}}\frac{1}{P} + \frac{1}{q_{sat}} \tag{5.4}$$

Equation (5.3) and (5.4) are mathematically equivalent however, Equation (5.3) is more reliable (less sensitive) when fitting at higher pressures (HP) and Equation (5.4) is better suited to lower pressures (LP).

Significant variation can often be seen in the q_{sat} and b parameters depending on whether Equation (5.1), (5.3) or (5.4) are used (Table E.1/Table E.2). For this reason, parameters are fitted using all three forms and the one giving the highest R^2 value is used.

The b parameter in Equations (5.1) - (5.4) generally follows the Arrhenius type dependence given in Equation (5.5). If isotherms are obtained at a range of different temperatures and the b_0 and E parameters calculated it is then theoretically possible to predict an adsorption isotherm at any intermediate temperature.

Starting from Equation (5.5), taking logs of both sides and then plotting $ln\ b$ vs $1/T$ (the highlighted variables) yields another straight line. This line has an intercept of $ln(b_0)$ and a gradient E/R (where R is the universal gas constant and E is an activation energy).

$$b = b_0 \exp\left(-\frac{E}{RT}\right) \tag{5.5}$$

$$\ln(b) = -\frac{E}{R}\frac{1}{T} + \ln(b_0) \tag{5.6}$$

5.4. Calculation of the isosteric heat of adsorption

Once isotherms have been obtained at different temperatures (in this case from separate simulations), the isotherms can be used to calculate a loading dependent heat of adsorption, ΔH (Figure 5.1).

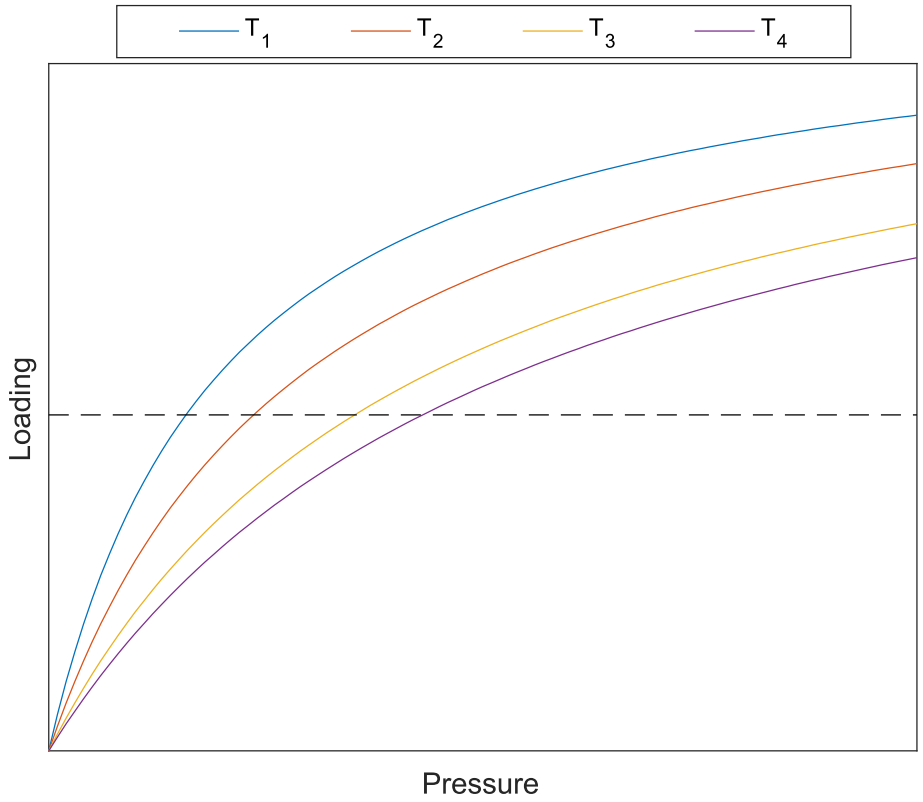

Figure 5.1: Sample isotherm with dotted isostere ($T_1 < T_2 < T_3 < T_4$)

By taking an isostere, a line of constant loading, the pressure required to yield the same loading can be found for different temperatures. A plot of $ln\ P$ vs $1/T$ yields a line with gradient of $\Delta H/R$ as per Equation (5.7). This method is used to calculate the heat of adsorption in Section 5.5.

$$\left(\frac{\delta(\ln P)}{\delta\left(\frac{1}{T}\right)}\right)_{\theta=constant} = \frac{\Delta H}{R} \tag{5.7}$$

Where θ is the coverage (loading) of the material

5.5. Isotherm Analysis

Figure 5.2, Figure 5.3 and Figure 5.4 show the simulated adsorption isotherms for the three separations of interest. The data points are generated from GCMC simulations (see Appendix A and Appendix C for details) so equilibrium rather than kinetic/diffusion control is assumed. In Section 5.5, the diffusion rates are examined to determine whether molecules are able to transition between cages.

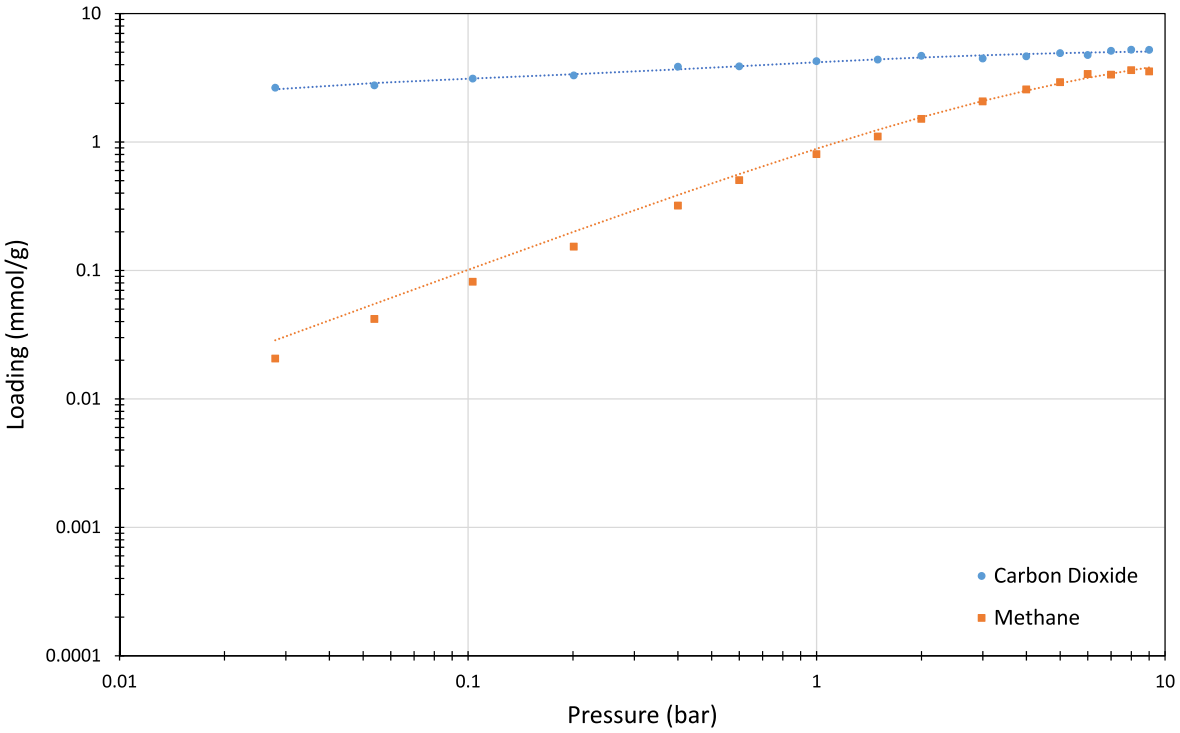

Figure 5.2: Simulated isotherms for pure CO_2 and CH_4 at 298 K after 3 rounds of MC/MD in Na-RHO (Si/Al=3.92)

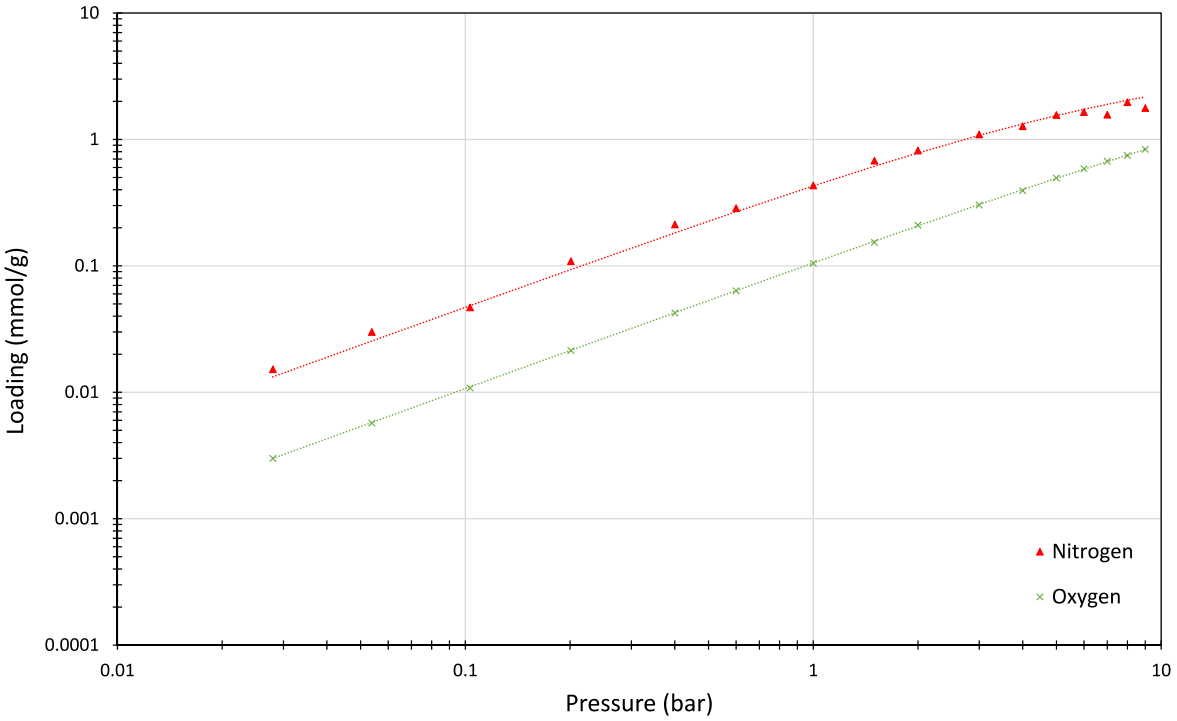

Figure 5.3: Simulated isotherms for pure O_2 and N_2 at 298 K after 3 Rounds of MC/MD in Na-RHO (Si/Al=3.92)

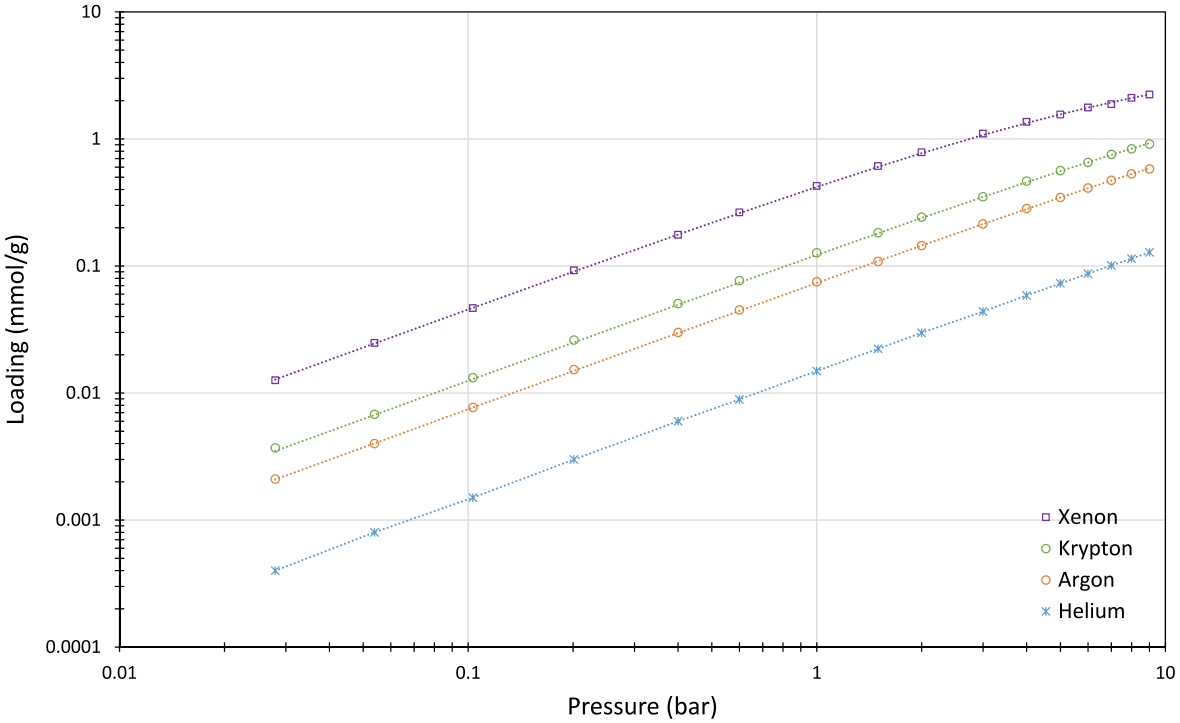

Figure 5.4: Simulated isotherms for noble gases at 298 K after 3 Rounds of MC/MD in Na-RHO (Si/Al=3.92)

With the exception of CO_2, all of the gases are well fitted by a single site Langmuir model in the range 0.03 – 9 bar between temperatures of 285 K and 315 K. The saturated loading, Langmuir b_0 parameter and activation energy for these are

given in Table 5.1. In each case, fits were attempted using Equations (5.1), (5.3) and (5.4) and the fit that gave the highest R^2 value was chosen. The separated b_0 and $\Delta E/R$ terms were calculated assuming the saturated loading value at 285 K does not change with temperature. (This gives a good fit to the simulated data at 285 K, 298 K and 315 K so is a reasonable assumption).

Table 5.1: Heat of adsorption and Henry's/Langmuir constants in Na-RHO at 298 K

Gas	Average heat of adsorption (kJ/mol)	q_{sat} (mmol/g)	b_0 x10^6 (bar^{-1})	ΔE/R (K)	Henry's constant (molecules/unit cell/bar)	Henry's constant (mmol/g/bar)
He	-4.2	2.66	1067.2	498	0.05	0.02
Ar	-11.0	4.71	180.3	1342	0.23	0.07
Kr	-12.5	4.33	662.8	490	0.05	0.02
O_2	-12.7	6.06	101	1547	0.33	0.11
Xe	-17.5	4.91	673.3	2140	1.42	0.46
N_2	-23.6	4.11	6.5	2927	1.37	0.44
CH_4	-25.4	6.46	0.1	4175	3.19	1.03
CO_2	-40.3	SSL does not provide a suitable fit. See Table 5.2 for DSL parameters				

Although CO_2 is not well-modelled by a standard single site Langmuir model, the dual site Langmuir (DSL) model given in Equation (5.8) can reproduce the isotherm. The DSL model extends the underlying single site adsorption assumption to a second site. This would be consistent with CO_2 molecules being found both in the main *lta* cage (site I) and sitting partially at the interface between the *lta* cage and D8R (site II).

$$q = q_{1,sat}\frac{b_1 P}{1 + b_1 P} + q_{2,sat}\frac{b_2 P}{1 + b_2 P} \tag{5.8}$$

One particular problem with the Dual Site Langmuir model is that it requires a very accurate isotherm to obtain reliable values for $q_{1,sat}$, b_1, $q_{2,sat}$ and b_2. The values will often match a given isotherm well but the parameters are more sensitive to fluctuations in the data. In particular, the calculation of the Henry constant is affected as it is calculated directly from these quantities (Equation (5.9)).

$$K_H = q_{1,sat}b_1 + q_{2,sat}b_2 \tag{5.9}$$

The fitting parameters obtained using the DSL model for CO_2 at 298 K are given in Table 5.2. These give a Henry constant of ≈1500 molecules/unit cell/bar (483 mmol/g/bar).

Table 5.2: Dual site Langmuir parameters for simulated CO_2 uptake at 298 K

	Site 1	Site 2
q_{sat} (mmol/g)	2.182	3.101
b at 298 K (bar^{-1})	1.007	152.6

For any separation, the ideal porous material will have a low heat of adsorption, a high Henry's constant for the component of interest and a high saturation capacity. This is to ensure, respectively, that the energy required for removal of the adsorbed species during desorption is low, the affinity for the component of interest is high and the zeolite can remove a large amount of the component of interest from the feed gas before desorption is required.

To provide a benchmark to assess the values in Table 5.1, the heats of adsorption, equilibrium uptakes and Henry constants are provided for typical industrial zeolites[4] in Appendix F. These show that zeolite RHO is competitive with other zeolites based on equilibrium properties alone. The focus here is therefore on whether Na-RHO exhibits cation-gating with other gases (high kinetic selectivities) and therefore offers an advantage over more traditional adsorbents.

[4] Of the zeolites described there, zeolite 4A and 5A have LTA [118] topology and zeolite 13X has FAU [119] topology.

5.6. Diffusion rates at 600 K

In this section, 30 molecules of each gas are added to a 2 x 2 x 2 supercell and the mean squared displacement measured. The simulations are run at 600 K based on the findings of Section 4.4 which showed that due to limitations with the forcefield, a high temperature was needed to obtain substantial diffusion past the gating cations. This section therefore aims to assess, qualitatively, the difference in diffusion rates for different gases.

5.6.1. Diffusion of noble gases

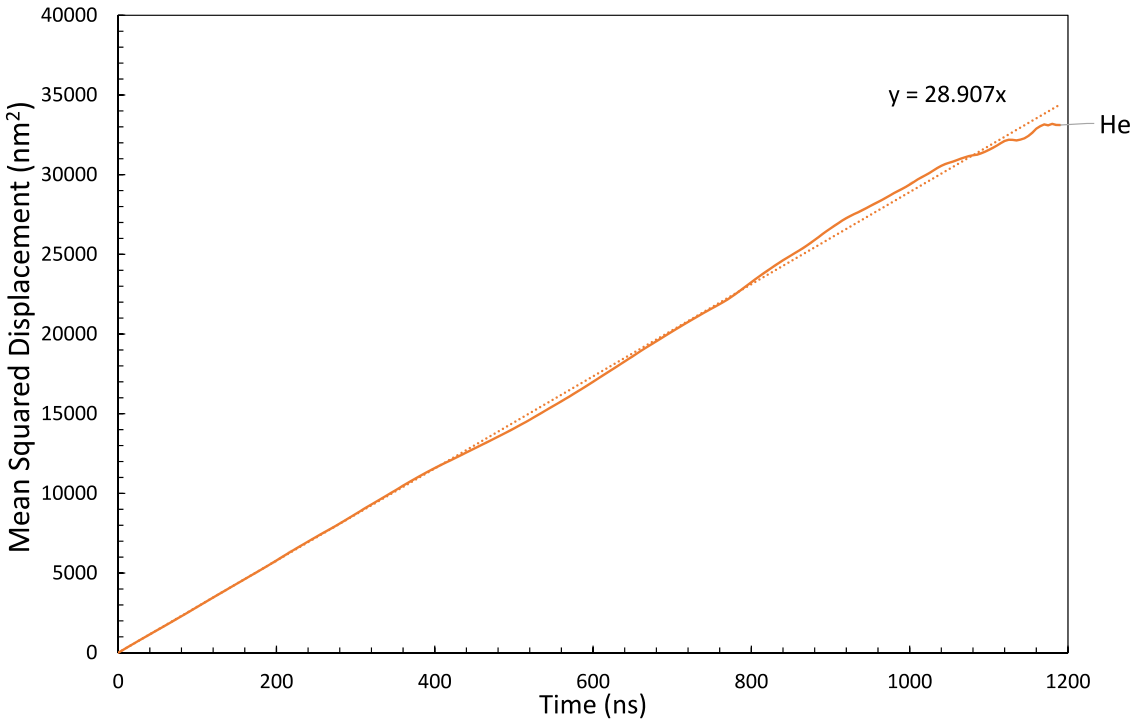

Figure 5.5: He mean squared displacement in Na-RHO at 600 K

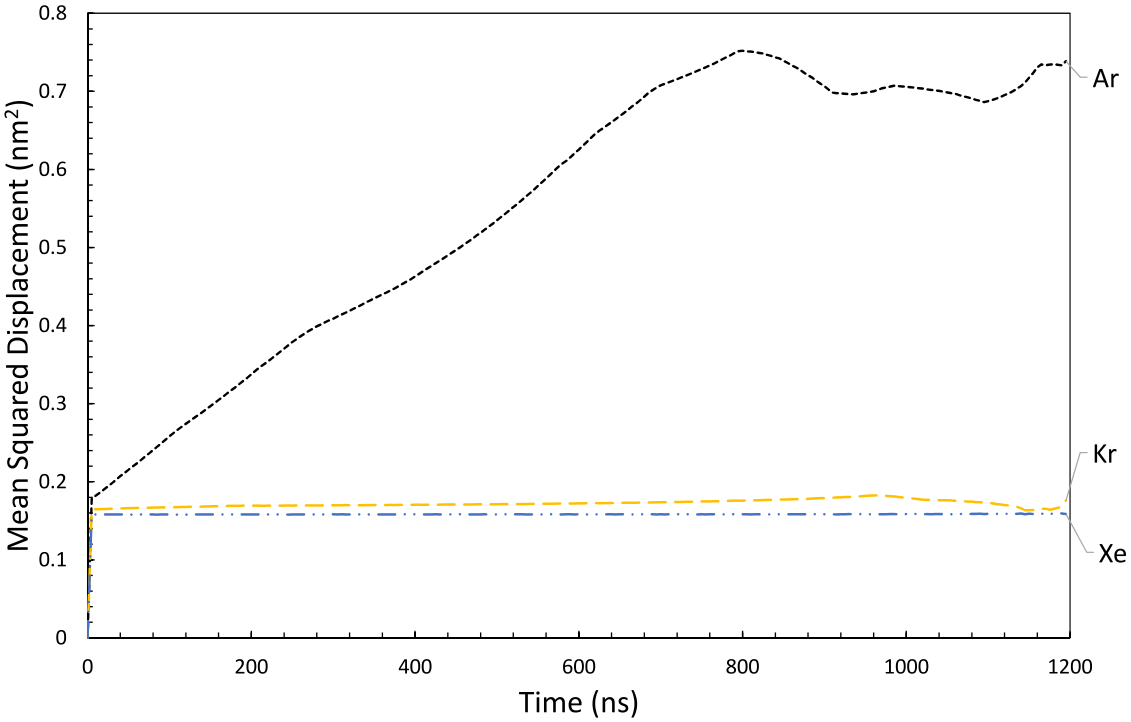

Figure 5.6: Ar/Kr/Xe mean squared displacement in Na-RHO at 600 K

Figure 5.5 shows that helium diffusion is well characterised by a linear fit through the origin. Examination of the helium trajectory shows that due to its small size, helium is able to diffuse through an 8MR, even in the presence of a cation. Helium is also able to pass through the 6MRs. This gives He a much faster rate of diffusion than Ar, Kr and Xe (Figure 5.6).

Over the microsecond trajectory, Ar diffuses from one *lta* cage into the centre of an adjoining D8R but not beyond. Diffusion of Kr and Xe is confined to a single *lta* cage only. This indicates that in practice Kr and Xe uptake will be very low. Ar uptake would likely be observed experimentally but due to diffusion limitations, would probably be slow to equilibrate.

5.6.2. Diffusion of O_2/N_2

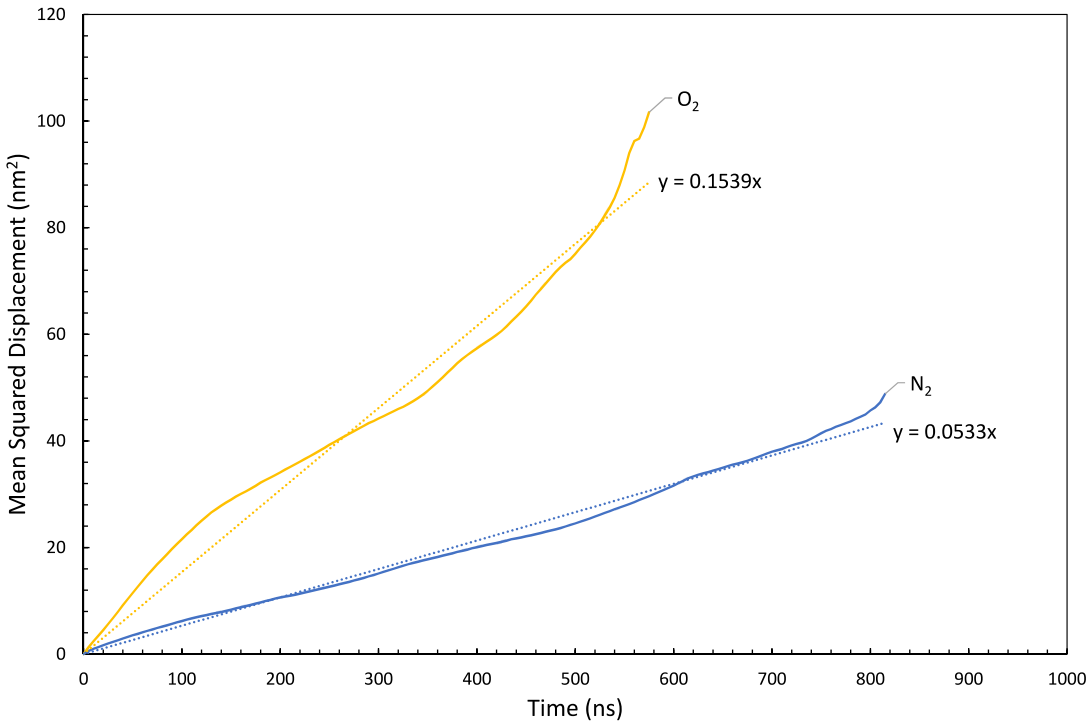

Figure 5.7: O_2/N_2 mean squared displacement in Na-RHO at 600 K

Figure 5.7 shows that, as expected based on the molecular size, smaller O_2 molecules diffuse faster than larger N_2. The diffusion rates, assuming a linear fit, are 8.6 x 10^{-9} cm^2/s for O_2 and 3 x 10^{-9} cm^2/s for N_2. This gives a pure component kinetic O_2/N_2 selectivity of ≈3, comparable to those reported for siliceous MFI [120]. It is therefore likely that cation gating is not playing a significant role in this separation.

5.6.3. Diffusion of CO_2/CH_4

Figure 5.8 shows a low diffusivity for both CO_2 and CH_4 with both gases reaching a plateau in msd after 1 μs. The low diffusion rate seen for CH_4 can be explained by Figure 5.9(L) which shows that CH_4 molecules explore only the *lta* cage that they are initially placed in and do not reach the S8Rs of the D8R cages. This suggests that CH_4 is repelled by both the D8R and D8R+cation combination.

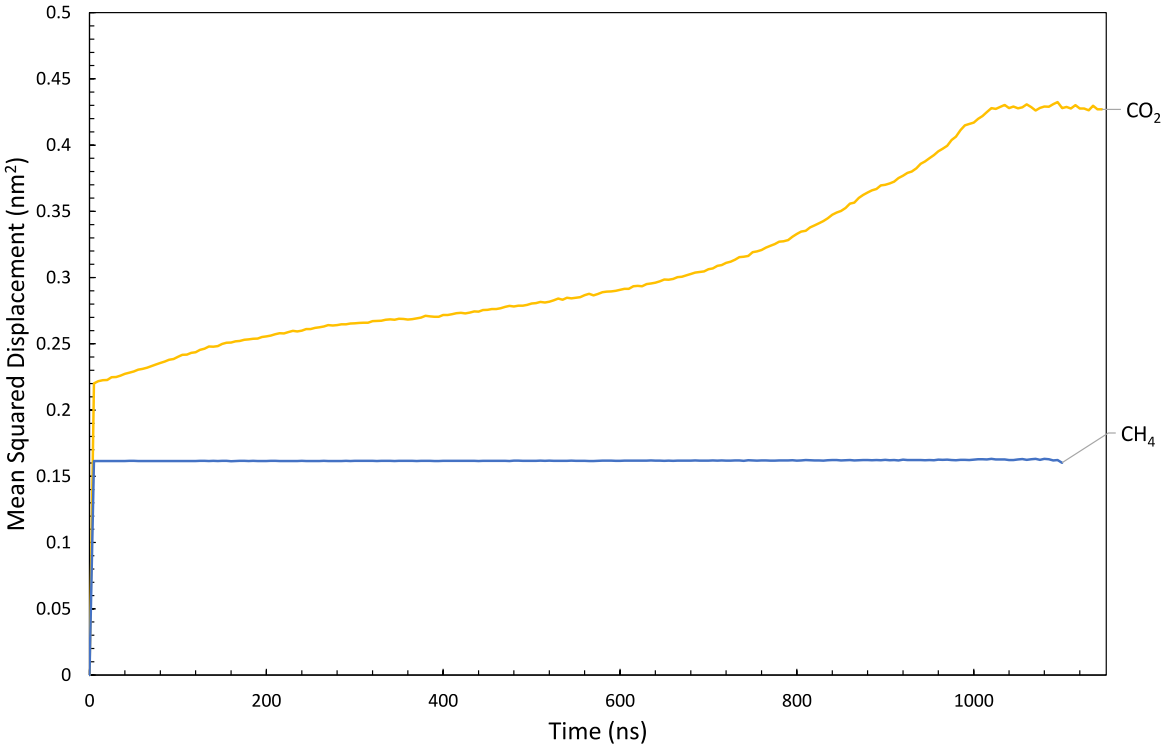

Figure 5.8: CO_2/CH_4 mean squared displacement (msd) in Na-RHO at 600 K

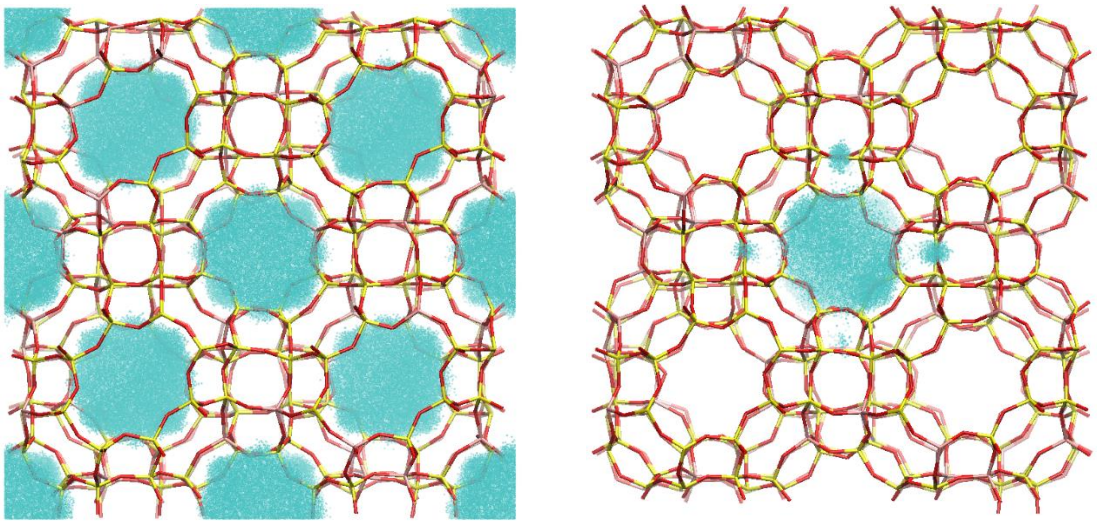

Figure 5.9: Regions explored by all CH_4 molecules (Left) and a single CO_2 molecule (Right) during MD simulation at 600 K (just the carbon atoms are shown in both cases)

The low CO_2 diffusion (Figure 5.8/Figure 5.9) is particularly interesting as in MD simulations with a loading of to 16.125 molecules/unit cell (Section 4.4), many crossings were observed. Figure 5.9(R) on the other hand shows that when the trajectory of individual CO_2 molecules is examined at an overall loading of 3.75 molecules/unit cell, no D8R crossings are observed.

The difference in diffusion rates between the two simulations suggests that a critical CO_2 loading is needed to observe diffusion. Experimental measurements of CO_2 uptake (Figure 5.10) also support this. At low pressures (<0.004 bar), uptake is very low but then climbs rapidly. Equilibrium MC simulations do not reproduce this effect suggesting that whilst it is energetically favourable to have molecules of gas adsorbed at low pressure, experimentally it takes a long time to observe uptake.

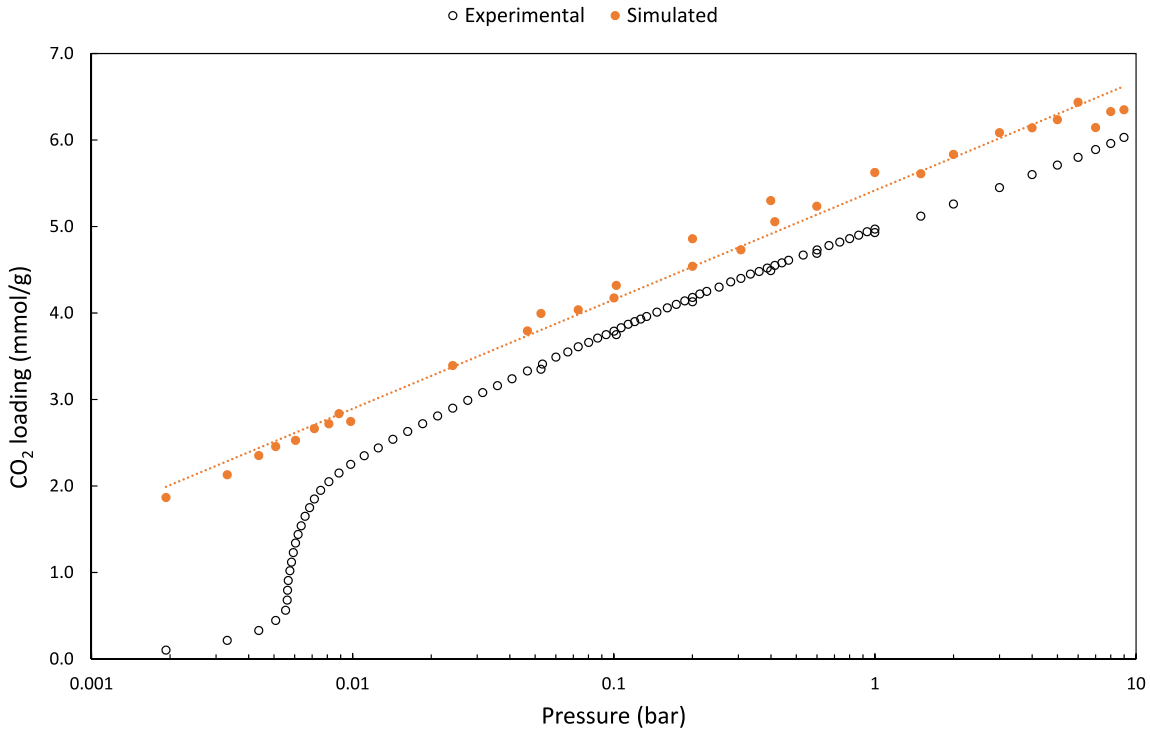

Figure 5.10: Comparison of simulated and experimental isotherm over an expanded pressure range at 298 K. (Simulated results using cation parameters by Maurin et al. [80]*)*

A critical CO_2 uptake is important as it suggests that whilst the trapdoor motion occurs primarily because of the mechanism outlined already (Section 4.4), there is

also a collaborative element occurring between multiple CO_2 molecules and the Na^+ cation. For the gating mechanism to function, cations must experience a significant force from more than just a single CO_2 molecule and it is this combined set of interactions which is responsible for the gating mechanism as a whole.

5.7. Concluding remarks

In this section, Na-RHO has been shown to have a high equilibrium selectivity for the CO_2/CH_4 separation (Figure 5.2). At the low concentrations examined here (3.75 molecules/unit cell), the diffusion rate of CO_2 is quite slow and this provides valuable insight into the cooperative nature of CO_2 in allowing diffusion past an 8MR cation. CH_4 was unable to enter/approach the D8R and this is likely due to its larger kinetic diameter (3.7 Å for CH_4 as opposed to 3.3 Å for CO_2 [121]).

For the separation of O_2/N_2, a pure component equilibrium selectivity of between 5 (at 0.03 bar) and 2 (at 9 bar) was observed (Figure 5.3). The O_2/N_2 kinetic selectivity was 3, with both components able to diffuse through the D8R.

With the noble gases, the heavier noble gases were adsorbed more strongly than the lighter ones (Figure 5.4). This is the expected result and is due to the stronger dispersion interactions modelled by the Lennard-Jones potential. The diffusion rate of helium was faster than that of any other gas examined in this study. This is a result of being able to pass unhindered through the 8MR, independent of the presence of a cation. It is also small enough to pass through the 6MR.

For the heavier noble gases, Ar is able to pass through the D8R (albeit slowly) but Kr and Xe are blocked. Na-RHO is therefore a candidate for separating He/Ne/Ar from Kr and Xe but would unlikely be much use for a Xe/Kr separation.

6. Framework tuning

I would like to acknowledge the work of Dr Claire Hobday at the University of Bath for running the DFT simulations in this section.

6.1. Preface

The separation of a gas mixture is traditionally dependent on three main factors [122]: size/steric exclusion where molecules which are too big are unable to fit through the windows (molecular sieving); thermodynamic selectivity, a measure of the relative uptake between species; and kinetic selectivity measuring the difference in the rate at which molecules diffuse through the cages. In zeolites, these can often be adjusted by modifying the Si/Al ratio [123] or changing the cation species through ion exchange [124].

It is difficult to decouple the three mechanisms. When either the Si/Al ratio or cation content is altered both the window size (hence kinetics) and the thermodynamic selectivity are affected. In general, Si/Al ratios closer to unity will cause the unit cell to contract, shrinking the size of the windows. Increasing the ionic radius of the compensating cation will push the windows open further, increasing also the size of the unit cell. The additional effect of trapdoor gating brings with it further changes in kinetic selectivity.

In this section, the effect of adjusting the Si/Al ratio and partially exchanging Na-RHO with Li^+ is explored using available experimental data where possible as a guide [43].

6.2. Si/Al adjustment

6.2.1. Introduction

A first approach to maximising selectivity for a given separation, whether based on a trapdoor separation or otherwise, is to control the size of the cage windows. Adjusting the size of the windows effects the energy barrier that must be overcome for cage-to-cage diffusion and ultimately can prevent uptake altogether (molecular sieving). A balance must be struck between ensuring that unoccupied windows are small enough to block uptake of the larger species but large enough to achieve a reasonable rate of the diffusion for the smaller molecule.

Zeolite RHO has been synthesised with a variety of Si/Al ratios (Table 6.1). It is typical to produce RHO at a Si/Al ratio around 3 and then reduce the aluminium content in post-synthetic steaming [125], although there has been some success in producing higher silica RHO zeolites during synthesis [126].

Table 6.1: Si/Al ratios compositions synthesised for RHO

Si/Al ratio	Number of Al/ unit cell	Source
∞	0	Not synthesised
27 (steamed)	1.7	[125]
15.9 (NMR measurement)	2.8	[126]
8.6 (refinement)	5	[126]
5	8	[127]
3.9	9.8	[7]
3.2	11.4	[43]
1.9	19.2	[128]
1	24	Not synthesised

The range of Si/Al ratios in Table 6.1 varies over most of the possible cation compositions (between 2 cation/uc and 19 cations/uc out of a maximum 24 cations/uc). To identify the trends associated with changing Si/Al, the full range from silicalite RHO to Si/Al=1 is examined. Most of the data generated therefore corresponds to structures which could theoretically be synthesised via known routes. It should be emphasised at this point that to the best of author's knowledge, there are no known published measurements of the unit cell length for Si/Al ratios other than 3.9 in the Na-RHO form. Data presented here should

therefore be treated cautiously as the model has not been calibrated to reproduce experimental unit cell length for other Si/Al ratios. (Work in Chapter 3 showed that the unit cell length is particularly sensitive to the choice of the Coulombic scale factor and in this chapter the value has been fixed at 0.385 as per the previous sections).

Table 6.2: Si/Al ratios examined in this work

Si/Al	Number of cations/supercell	Number of cations/unit cell
∞	0	0
18.2	20	2.5
8.6	40	5
5.4	60	7.5
3.92	78	9.75
2.84	100	12.5
2.07	125	15.625
1.56	150	18.75
1.19	175	21.875
1	192	24

6.2.2. Cation Locations

Table 6.3 shows the cation occupancies for the Na-RHO structures following a 5 ns REMD simulation. This shows a consistent preference for Na^+ to occupy the S8R.

As the number of occupied 8MR sites increases, cations increasingly sit in the 6MR. There are a total of twelve 8MRs/unit cell and eight 6MRs/unit cell so cations would rather dual-occupy a 6MR (one cation either side of the ring) than dual occupy a S8R.

Table 6.3: Na^+ occupancies with increasing Si/Al ratios

Si/Al	Number of cations/supercell	Number of cations/unit cell	Number of cations in D8R/unit cell	Number of cations in S8R/unit cell	Number of cations in 6MR/unit cell
∞	0	0	0	0	0
18.2	20	2.5	0	1.375	1.125
8.6	40	5	0	3.6250	1.3750
5.4	60	7.5	0	5.5	2.5
3.92	78	9.75	0	5.6250	4.1250
2.84	100	12.5	0	8.125	4.375
2.07	125	15.625	0	10.25	5.375
1.56	150	18.75	0	11.125	7.625
1.19	175	21.875	0	12	9.875
1	192	24	0	12.125	11.825

6.2.3. Limiting pore diameter

In the absence of cations, the dimensions of the 8MR control whether a molecule is able to diffuse through the ring. The limiting 8MR diameter (AE vs CG in Figure 2.4) is therefore key to predicting whether a molecule can diffuse through the ring. This opens up the possibility of pore size modification through adjustment of the Si/Al ratio.

Figure 6.1 shows the variation of the minimum aperture in the 8MR with increasing Al content. As the Al content increases, the rings distort further and so the minimum 8MR width reduces. Over the range of synthesised RHO structures (Si/Al = 1.9 – 27), the 8MR width for Na-RHO decreases from 5.35 Å to 4.86 Å.

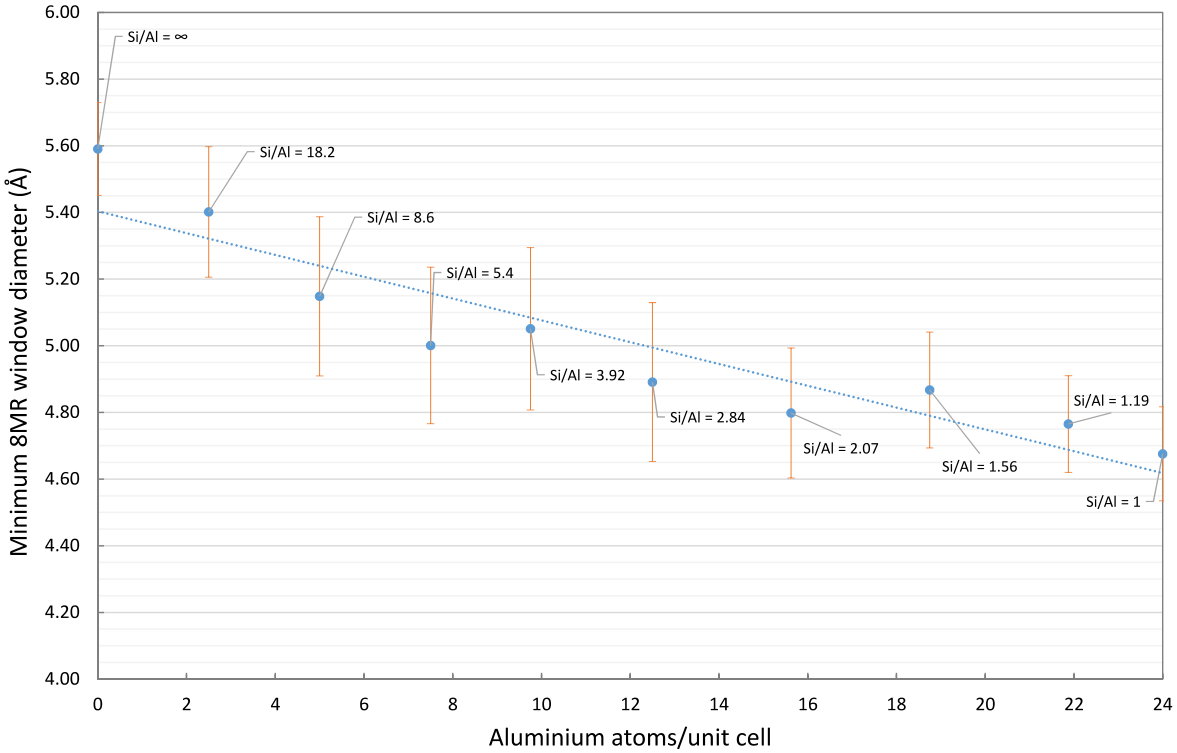

Figure 6.1: Minimum 8MR window diameter in Na-RHO at 300 K calculated from the average of all 8MRs during a 5 ns MD simulation

6.2.4. 8MR distortion

A characteristic measure of the 8MR distortion, Δ, is introduced in Section 2.2. This parameter quantifies the degree to which an 8MR is longer than it is wide. For a Si/Al ratio of 3.92, the delta parameter is 2.04 Å. Over the range of synthesised RHO structures (Si/Al = 1.9 – 27), the delta parameter varies from 1.57 Å to 2.26 Å.

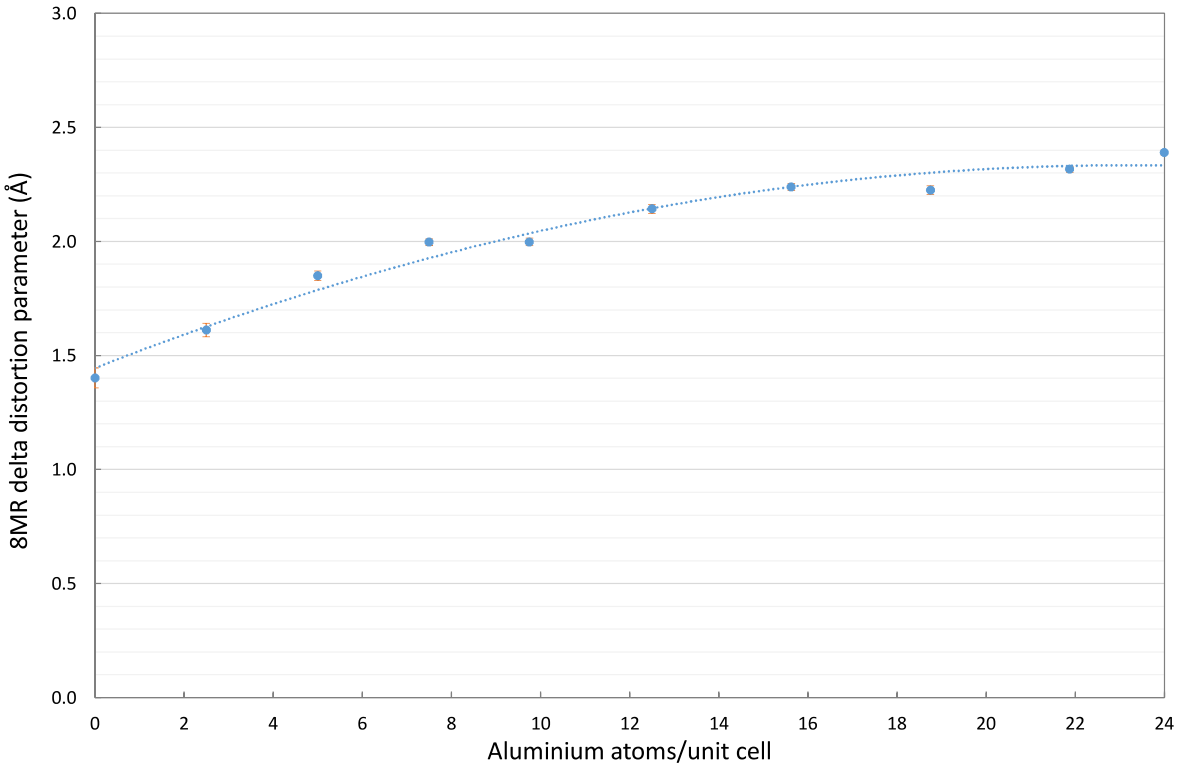

Figure 6.2: Variation of delta 8MR parameter in Na-RHO at 300 K calculated from the average of all 8MRs during a 5 ns MD simulation. Line of best fit is intended to guide the eye only.

6.2.5. Cell dimension

The most useful measure for quantifying the rings when looking at the change in aluminium content is the minimum 8MR aperture (Section 6.2.3). This is because the delta parameter (Section 6.2.4) is a relative measure of the difference between the length and width of the 8MR and is dependent partially on the size of the unit cell. (As the unit cell expands, the 8MRs are pulled into a more centric form.)

Table 6.4 shows that up to a Si/Al ratio of 2.07, the unit cell length generally decreases with increasing cation/aluminium content. As the aluminium content increases, the repulsion between the atoms increases and the unit cell begins to expand again. This likely explains why the rate of increase in delta slows with increasing cation content in Figure 6.2.

Table 6.4: Variation in unit cell length at 300 K with increasing aluminium content

Si/Al	Number of cations/supercell	Number of cations/unit cell	cell dimension (Å)	Uncertainty in cell dimension (Å)
∞	0	0	14.58	0.02
18.2	20	2.5	14.52	0.02
8.6	40	5	14.43	0.01
5.4	60	7.5	14.39	0.01
3.92	78	9.75	14.43	0.01
2.84	100	12.5	14.39	0.02
2.07	125	15.625	14.39	0.01
1.56	150	18.75	14.47	0.01
1.19	175	21.875	14.46	0.01
1	192	24	14.44	0.01

6.2.6. CO_2 adsorption

When selecting a Si/Al ratio, one of the key characteristics is the working capacity i.e. the difference between the uptakes of a gas at the adsorption and desorption pressure. For the component of interest (in this case CO_2), this wants to be as large as possible.

To investigate the uptake of CO_2, 3 rounds of MC and MD were undertaken for the Si/Al ratios listed in Table 6.3. Figure 6.3 shows there is a peak for CO_2 adsorption at around 10 cations/unit cell. In terms of maximising equilibrium adsorption, there is a balance between a beneficial increase in the number of CO_2-cation interactions at lower Si/Al ratios and decreasing the available pore volume by filling the cages with cations.

Figure 6.3 shows that up to 10 cations/uc, adding additional cations is beneficial, after which the reduction in the pore volume and increased Na^+-Na^+ repulsion reduces the uptake of CO_2. The effect is particularly noticeable for pressures below 1 bar.

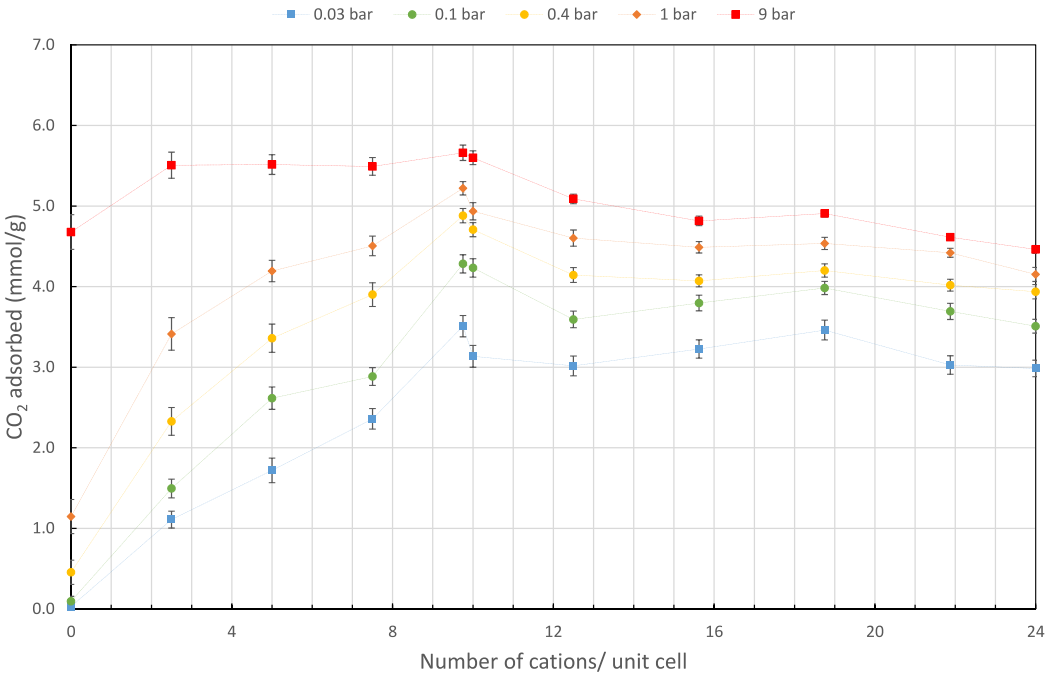

Figure 6.3: CO_2 adsorption isotherms in Na-RHO with varying numbers of cations (lines are to guide the eye only). Error bars show 1 standard deviation on the final 50% of the MC simulation. MC simulations are run from the final frame of an NPT MD simulation so the error bars do not include the effect of slightly different framework configurations.

6.2.7. CO_2 diffusion

Figure 6.4 shows the variation of the mean squared displacement with time for a range of different Si/Al ratios. For this section each framework is loaded with 100 CO_2 molecules/supercell. In each case, the temperature is set to 600 K in order to observe noticeable diffusion.

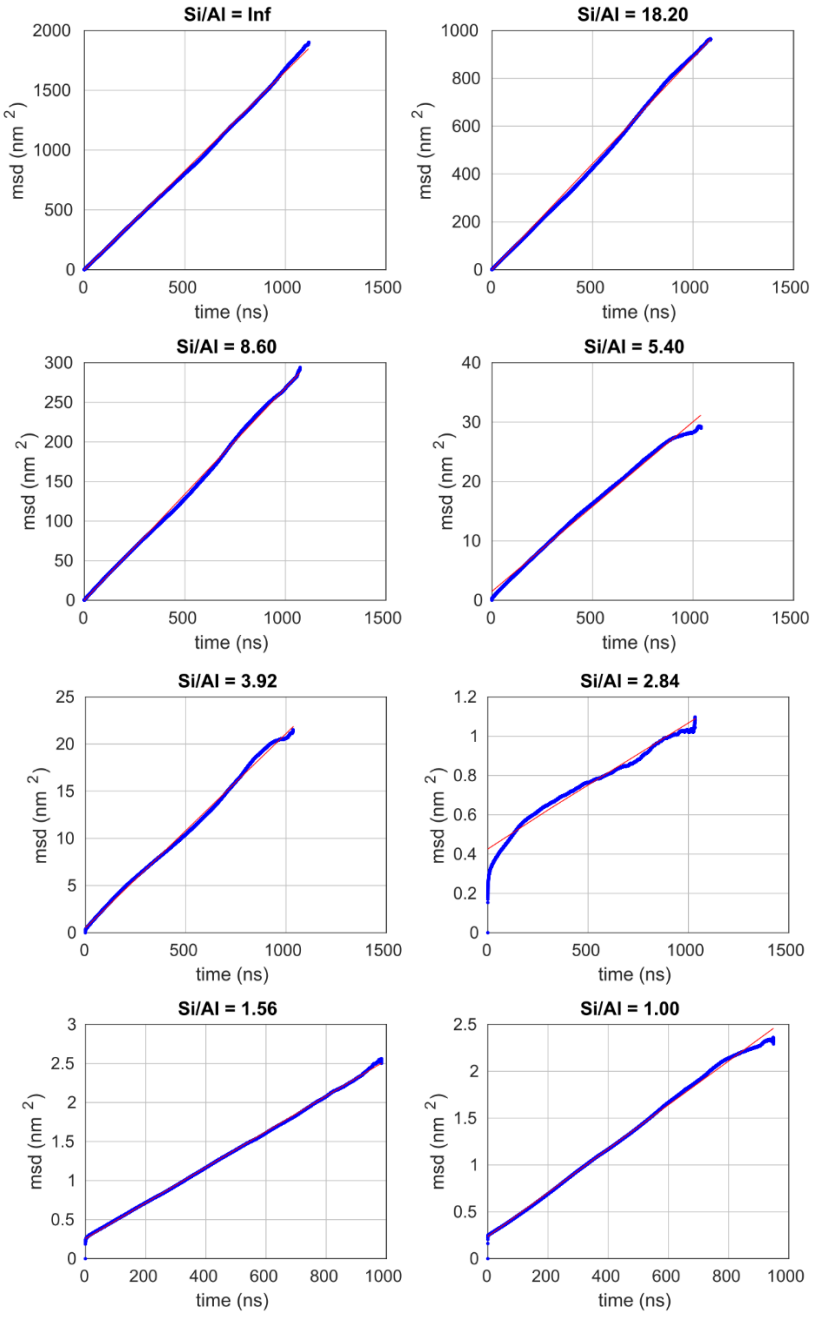

Figure 6.4: Mean squared displacement as a function of time for different Si/Al ratios at 600 K. The blue points show the msd and the red line is a fit to the linear diffusion model (Equation (2.64))

Table 6.5 gives the diffusion coefficients calculated from each graph in Figure 6.4. The highest diffusion rate is for siliceous RHO. Here, CO_2 is free to diffuse through the 8MRs unobstructed by cations. (This was identified in Section 4.3 as the lowest energy pathway between two cages.) Addition of 2.5 cations/unit cell, cuts the diffusion rate by half and the diffusion rate continues to slow with the addition of further cations. As the Si/Al ratio reduces below 3.92, the number of unoccupied low energy cation positions reduces and cation movement becomes increasingly hindered. At this point (Si/Al<3.92), there is a further reduction in diffusion rate and the diffusion rate plateaus at a minimum.

Table 6.5: Estimate of diffusion coefficients at 600 K based on 100 molecules CO_2/2 x 2 x 2 supercell

Si/Al	Number of cations/supercell	Number of cations/unit cell	Gradient (x 10^8 cm^2/s)	Estimate of D (x 10^{13} cm^2/s)
∞	0	0	16.53	2756
18.2	20	2.5	8.85	1476
8.6	40	5	2.67	446
5.4	60	7.5	0.29	48
3.92	78	9.75	0.21	34
2.84	100	12.5	0.006	1.1
1.56	150	18.75	0.023	3.8
1	192	24	0.023	3.9

6.3. Li-RHO simulations

6.3.1. Introduction

In this subsection, the effect of exchanging some (or all) of the Na^+ cations with Li^+ is explored. The objective here is to gain an understanding of the computational challenges required to look at mixed cation systems. With a suitable model, it would be possible in future work to tailor a RHO zeolite to a separation of interest by exploiting both cation gating and pore size modification.

Experimental work [43] has shown that unlike Na-RHO, the cations in Li-RHO preferentially occupy the 6MRs (Table 6.6). Li^+ also interacts more strongly with the framework than Na^+ and this causes the cell to contract to 14.24 Å [43]. This is substantially smaller than the 14.41 Å cell dimension observed for Na-RHO [7] with the same Si/Al ratio.

The contraction from 14.41 Å to 14.24 Å results in the 8MRs becoming highly elliptical [43] (Δ =1.9). This prevents hydrocarbons from diffusing through the 8MRs but still allows uptake of CO_2. For the CO_2/CH_4 separation, this gives both a high selectivity and fast kinetics [43].

Table 6.6: Cation occupancies per unit cell in Li-RHO [43]

	Number of cations in S8R/unit cell	Number of cations in 6MR/unit cell
Li-RHO	3	6.5

Although Na-RHO offers high CO_2/CH_4 selectivity, one of the practical failings is the slow diffusion kinetics [43]. In Li-RHO, the kinetics are faster but fewer 8MRs are blocked so the high selectivity observed is due mainly to molecular sieving (only 3 out of 6 D8Rs have a cation in so cation-gating is less significant). A Li/Na mixture therefore has the potential to offer moderate kinetics and high selectivity.

6.3.2. Lithium Lennard-Jones parameters

To study Li-RHO, a similar approach to the modelling of Na-RHO is used. 17 parameters for Li^+ are sourced from a variety of applications (Table 6.7) and the appropriate 1-4 scaling factor is found to reproduce the experimental unit cell length of 14.24 Å. REMD is then used to find the equilibrium cation positions. Once the cation positions have been found, 3 cycles of MC/MD are completed to capture the cell expansion on adsorption of CO_2.

Table 6.7: Lithium parameters and cation sitings. For the parameters by Watanabe et al. [129], the parameters are found from the N-N/N-Li and O-O/O-Li parameters using the Lorentz-Berthelot mixing rules.

Name	sigma (Å)	epsilon/k_B (K)	k_{scale}	Unmatched	D8R	S8R	6MR
Aqvist et al. [48]	1.46	34.02	0.360	0	0	3.125	6.625
CVFF [71]	2.84	2383	0.365	0	5.75	0.125	3.875
Hutson et al. [130]	1.22	4.38	0.355	0.125	0	3.5	6.125
Jeffroy et al. [55]	2.35	38.68	0.370	0	0	6.625	3.125
Jensen et al. [76]	2.87	0.25	0.360	0	0	3.5	6.25
Jensen et al. [76] (prior values)	2.13	9.20	0.368	0	0	4.25	5.5
Kowsari et al. [131]	1.09	4.38	0.360	0	0	3.375	6.375
Kumar et al. [132]	1.44	51.90	0.362	0	0	3.125	6.625
Lamoureux et al. [77]	2.31	1.17	0.365	0	0	3.875	5.875
Lee et al. [85]	2.21	495.30	0.355	0	0	7.625	2.125
Maurin et al. [80]	1.10	362.18	0.363	0	0	3.25	6.5
UFF [47]	2.18	12.58	0.365	0	0	4.375	5.375
Vessal et al. [133]	5.76	0.0001	0.370	0	0	5.75	4
Watanabe et al. (N) [129]	1.06	4.01	0.355	0	0	3	6.75
Watanabe et al. (O) [129]	1.07	4.82	0.355	0.125	0	3.75	5.875
Webb et al. [134]	1.40	201.29	0.360	0	0	3	6.75
Wozniak et al. [135]	1.60	2381	0.370	0	0	4.5	5.25

6.3.3. Cell expansion

The study of Li-RHO is more complex than that of Na-RHO as the available experimental gas adsorption data comes from a hydrated form with 3.7 H_2O molecules/unit cell. This hydrated structure has a unit cell length of 14.34 Å with no CO_2 adsorbed [43], as opposed to 14.24 Å. The additional molecules of water likely enter during the drying phase when hot air is used to dry the sample in-situ (before XRD measurements are taken [43]). The water becomes strongly bound to the cations and is not fully removed by the air stream.

Figure 6.5 shows the simulated cell expansion on loading Li-RHO with CO_2 at pressures up to 9 bar with no H_2O present. Of the parameters tested, only those by Aqvist et al. [48] give a reasonable expansion. (All others show essentially no expansion with CO_2 loading). As the Aqvist et al. [48] parameters also worked well for Na-RHO and the Li^+ parameters are essentially rescaled Na^+ parameters [48], the parameters from Aqvist et al. [48] are also selected for the study of Li-RHO.

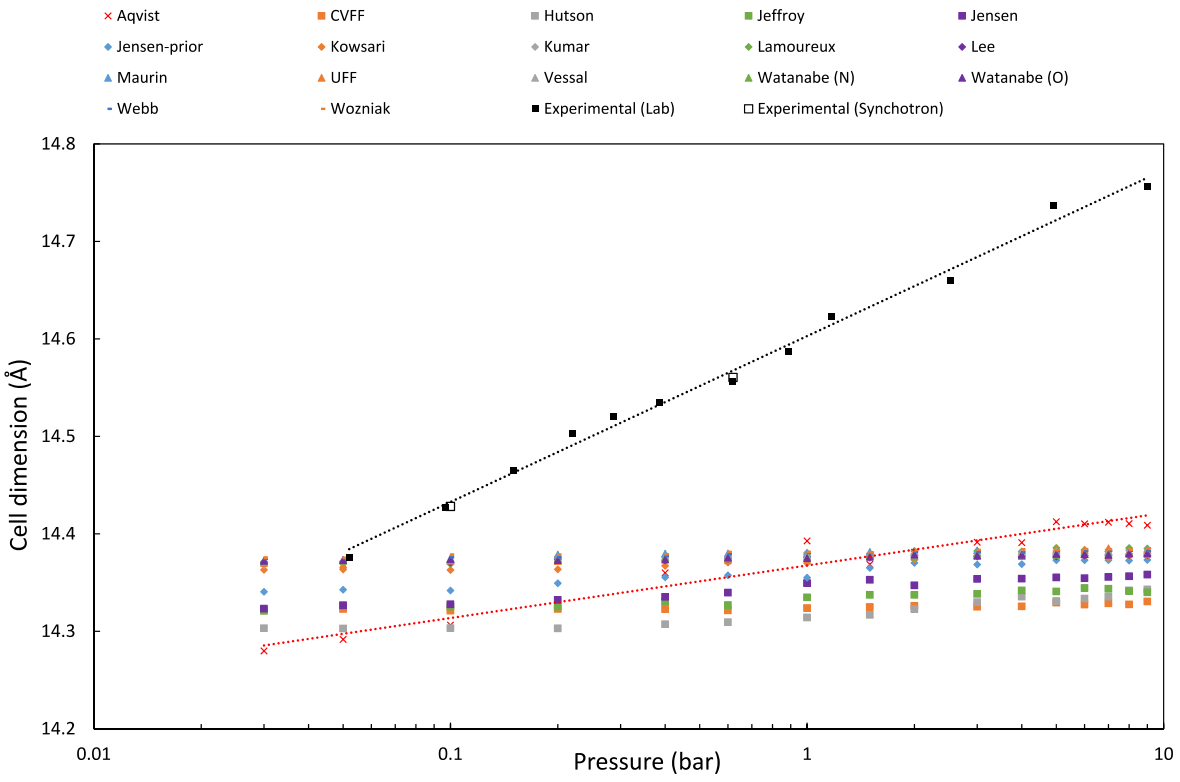

Figure 6.5: Unit cell expansion on loading with CO_2 at the end of the third round of NPT molecular dynamics. The red (lower) line shows the line of best fit for the parameters by Aqvist et al. [48] and the black (upper) line of best fit shows the trend through the hydrated experimental points.

Figure 6.6a and Figure 6.6b show the CO_2 adsorption isotherm in Li-RHO for both the simulated and experimental results. A dual site Langmuir fit is added to both to see more clearly the trend in the simulated points. The parameters are given in Table 6.8.

Table 6.8: Dual Site Langmuir parameters for simulated CO_2 uptake in Li-RHO isotherm at 298 K

	Site 1	Site 2
q_{sat} (mmol/g)	2.173	3.526
b (bar^{-1})	133.5	2.688

Figure 6.6 shows a comparison between the simulated isotherms, along with previously published [43] and updated isotherms [136]. There is a clear mismatch between the simulated and experimental isotherms, although this is improved somewhat with the updated (experimental) isotherm. The discrepancy likely arises due to the difference in simulated vs experimental cell expansion (Figure 6.5). However, in the region most of interest for desorption (between 0.1 and 1 bar), the gradient of the line in Figure 6.6 is well matched. This indicates that although less CO_2 is adsorbed than expected, similar trends in behaviour can be observed within this region.

a)

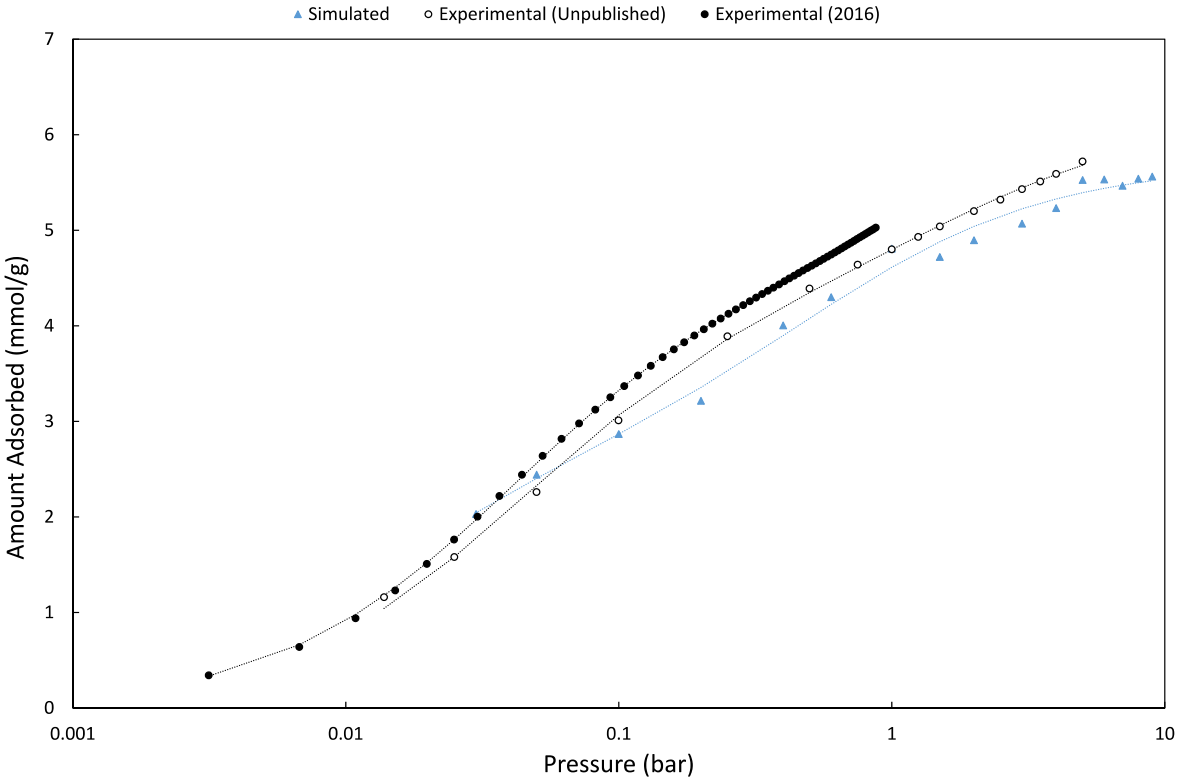

b)

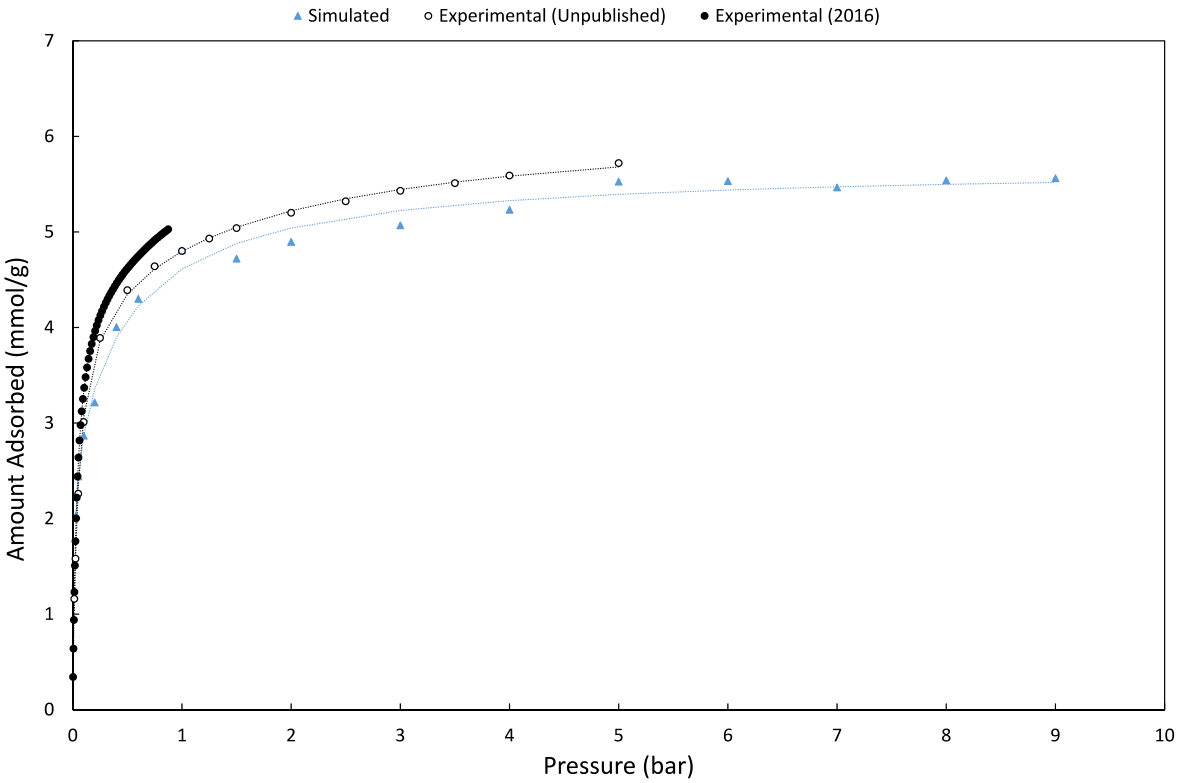

Figure 6.6: Comparison of simulated and experimental CO_2 adsorption in Li-RHO at 298 K on a) log scale, b) linear scale

6.3.4. Effect of water

One way to gain additional insight into the behaviour of Li-RHO on adsorption of CO_2 is to run variable volume (NPT) DFT simulations with increasing numbers of CO_2 molecules (Figure 6.7). With no water or CO_2 present, the DFT simulations give a cell length of 14.11 Å. Assuming that the dehydrated structure at 14.24 Å is completely free of H_2O, this represents an underprediction of the unit cell length.

This discrepancy in unit cell length could be explained by the DFT simulation simply underpredicting the unit cell length. However, this is somewhat unexpected as the Generalised Gradient Approximation (GGA) used in the DFT simulation would generally be expected to overpredict, rather than underpredict, the unit cell length of a zeolite [137].

A second explanation might be that there are still a few water molecules present in the 14.24 Å sample. To dehydrate the sample, the zeolite was heated at 300 °C for extended periods under vacuum and then sealed. If water is still present then the conditions were either not severe enough to remove all the water, as would be the case for Cd-RHO [85] (see section 3.6.3 for details), or some water was reabsorbed after heating (before sealing).

Ensuring that the unit cell length is correct is particularly important for calibrating the k_{scale} value. For this work, the completely dehydrated Li-RHO structure is assumed to have a unit cell length of 14.24 Å and the k_{scale} value is set accordingly to 0.36.

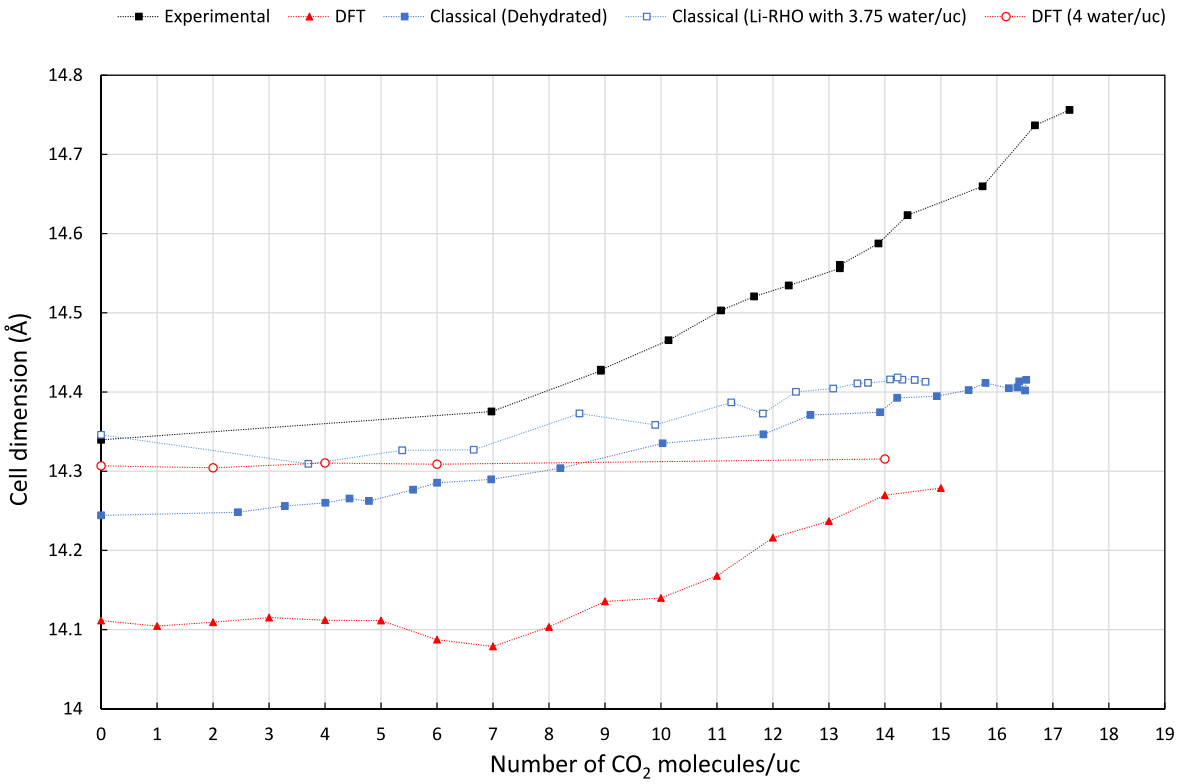

Figure 6.7: Comparison of the unit cell dimension at 298 K for Li-RHO measured with increasing numbers of CO_2 molecules: experimentally at 298 K (black); in a DFT simulation with (red unfilled) and without (red filled) water; and in a classical MD NPT simulation with (blue unfilled) and without (blue filled) water.

Figure 6.7 shows a comparison of the Li-RHO cell dimension obtained at 298 K with increasing numbers of CO_2 molecules via experimental measurements (black), classical simulations (blue) and DFT calculations (red). Filled symbols indicate dehydrated measurements and unfilled circles indicate hydrated measurements.

The blue, unfilled symbols correspond to adding 3.75 molecules of water/unit cell (30 molecules of water/2 x 2 x 2 supercell). This is the closest match to 3.7 molecules/uc measured experimentally [43]. For these measurements, 30 molecules of water are added along with a fixed number of CO_2 molecules. The volume of the box is then allowed to relax. Up to the addition of 10 molecules CO_2/unit cell, both the dehydrated and hydrated classical simulations match the general upward trend of the experimental results. As expected, the hydrated simulations give a

better match to the unit cell lengths measured in the partially hydrated experimental system.

The DFT simulations with 4 H_2O molecules/uc are in good agreement with the experimental XRD measurement with 3.7 H_2O molecules/uc, although unlike the experimental work, the DFT results do not then show further expansion on CO_2 loading.

In the dehydrated DFT simulations, the general trend (slope) of the experimental data is matched although the simulations are offset by -0.3 Å. Up until 8 molecules CO_2/uc both the experimental and DFT simulations show little expansion on CO_2 uptake but then expand linearly with increasing numbers of CO_2 molecules.

6.3.5. Comparison of hydration effect in Na-RHO

As the addition of water gives rise to a significant change in unit cell length in Li-RHO (increase from 14.2442 to 14.3396 Å), it is interesting to do a similar comparison for Na-RHO. On very thorough dehydration (up to 500 °C - Figure 3.14) the unit cell length reduces from 14.4139 Å [7] to 14.329 Å [128]. This new measurement is in good agreement with the DFT simulations that predict the unit cell length to be 14.332 Å (Figure 6.8). The measurement of 14.4139 Å agrees well with the AIMD simulation containing 1 water molecule. This may go some way to explain why in Figure 3.26, the simulated cell parameter in the optimised classical simulations is lower than the experimental measurements (no water was included in these simulations).

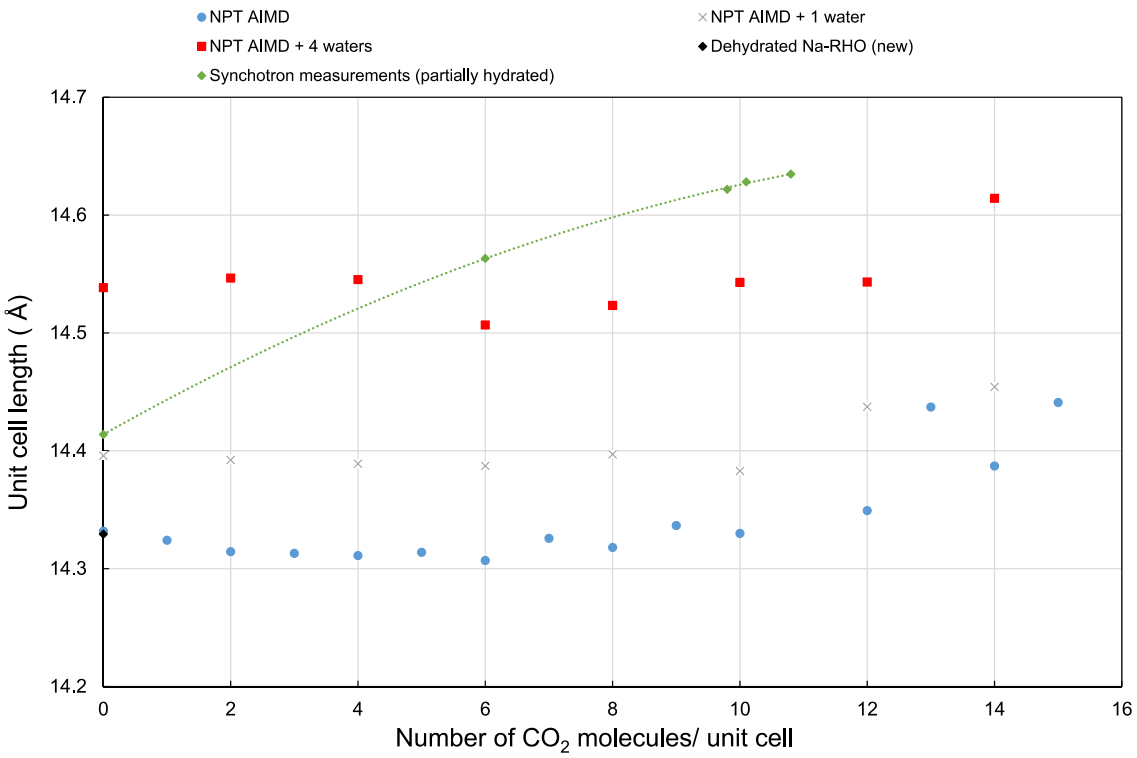

Figure 6.8: DFT cell expansion observed for Na-RHO. A curve has been fitted to the synchrotron measurements to guide the eye only.

Figure 6.8 shows that the DFT simulated unit cell length for Na-RHO is unresponsive to loading of CO_2 molecules until there are around 12 molecules of CO_2/unit cell. Thereafter, some cell expansion is seen but still less than that observed experimentally.

One of the most significant results is that adding water increases the unit cell faster and more substantially than adding CO_2. The addition of each water molecule increases the unit cell size by ≈0.05 Å/molecule. This is because the water is attracted much more strongly to the cations and is drawn to the S8R, forming a Na-H_2O complex. The close proximity of the water molecules to the cations creates an additional repulsive force causing increased cell expansion. CO_2 on the other hand sits more centrally in the *lta* cage so the repulsive forces are not as strong.

6.4. Li/Na mixtures

6.4.1. Introduction

A range of LiNa-RHO structures have been studied experimentally [43] to examine the effect of different cations on the CO_2 uptake and diffusion rate. This section aims to investigate the difficulty of applying the model used so far to mixed cation systems.

6.4.2. Scale factors

In the Li/Na study [43], Li/Na structures with Si/Al= 3.9 were refined for structures with 2.1, 4.3 and 6.2 Na^+ ions [43]. These are used to determine the necessary Coulombic scale factors needed to reproduce the experimentally measured cell lengths (Table 6.9). Prior to refinement, the mixed Li/Na structures were heated at 623 K under a vacuum pressure of 10^{-7} bar to fully dehydrate the samples.

Table 6.9: Li/Na mixture data [7] [43]

Structure	Experimental cell length (Å)	k_{scale}
Li	14.2442	0.36
$Li_{7.7}Na_{2.1}$	14.3017	0.368
$Li_{5.4}Na_{4.3}$	14.3176	0.37
$Li_{3.6}Na_{6.2}$	14.3331	0.37
Na	14.4139	0.385

6.4.3. Adsorption isotherms

Figure 6.9 shows the simulated CO_2 isotherms for the five systems examined (Table 6.9). The figure shows that replacing Na^+ with Li^+ decreases the uptake. This is due in part to the weaker CO_2-cation interactions with the smaller cation and in part to the decrease in cell volume (Table 6.9). The effect is most pronounced at lower loadings but is evident across the full pressure range examined.

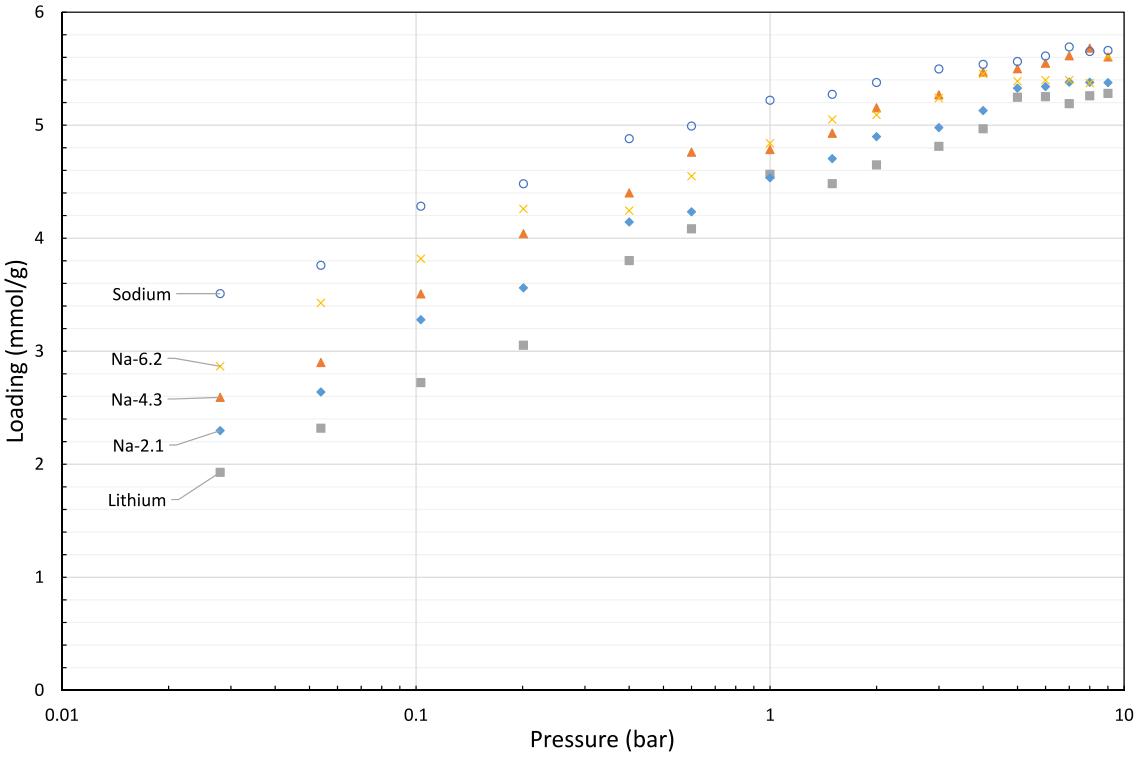

Figure 6.9: CO_2 adsorption isotherms at 298 K in Li/Na-RHO systems (Si/Al = 3.92)

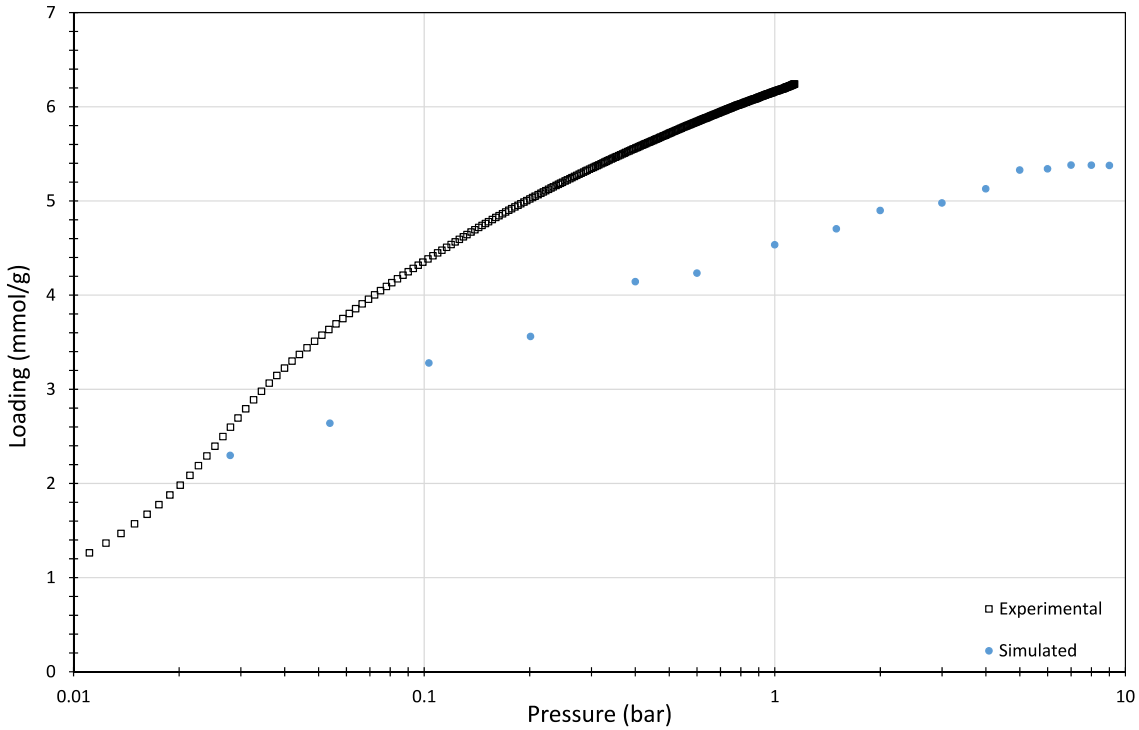

Figure 6.10: Comparison of simulated and experimental CO_2 adsorption isotherms in $Li_{7.7}Na_{2.1}$-RHO at 293 K

Figure 6.10 shows a comparison of the simulated and experimental [43] isotherms for the $Li_{7.7}Na_{2.1}$ mixture. As with the Li-RHO adsorption isotherm (Figure 6.6), there is an underprediction in the amount of CO_2 adsorbed. The maximum uptake at a given set of conditions is strongly influenced by the available pore volume and without being confident in capturing the correct Li-RHO expansion behaviour, refining the Li parameters to obtain a matching experimental isotherm is difficult. This final section therefore aims to look for qualitative trends rather than absolute agreement with experiment.

6.4.4. Effect on diffusivity

In this section, the diffusion rate of CO_2 is examined for each of the Li/Na systems. Data is collected from 1 μs simulations run with 100 molecules of CO_2/2 x 2 x 2 supercell. A temperature of 600 K is used to ensure intercage diffusion as per Chapter 4.

Figure 6.11 shows the variation of mean square displacement with time for the five systems examined. The general trend is for a decrease in CO_2 diffusivity with increasing Na^+ content up to $Li_{5.4}Na_{4.3}$-RHO. The estimated diffusion self-coefficients obtained assuming a linear fit (Equation (2.64)) are given in Table 6.10.

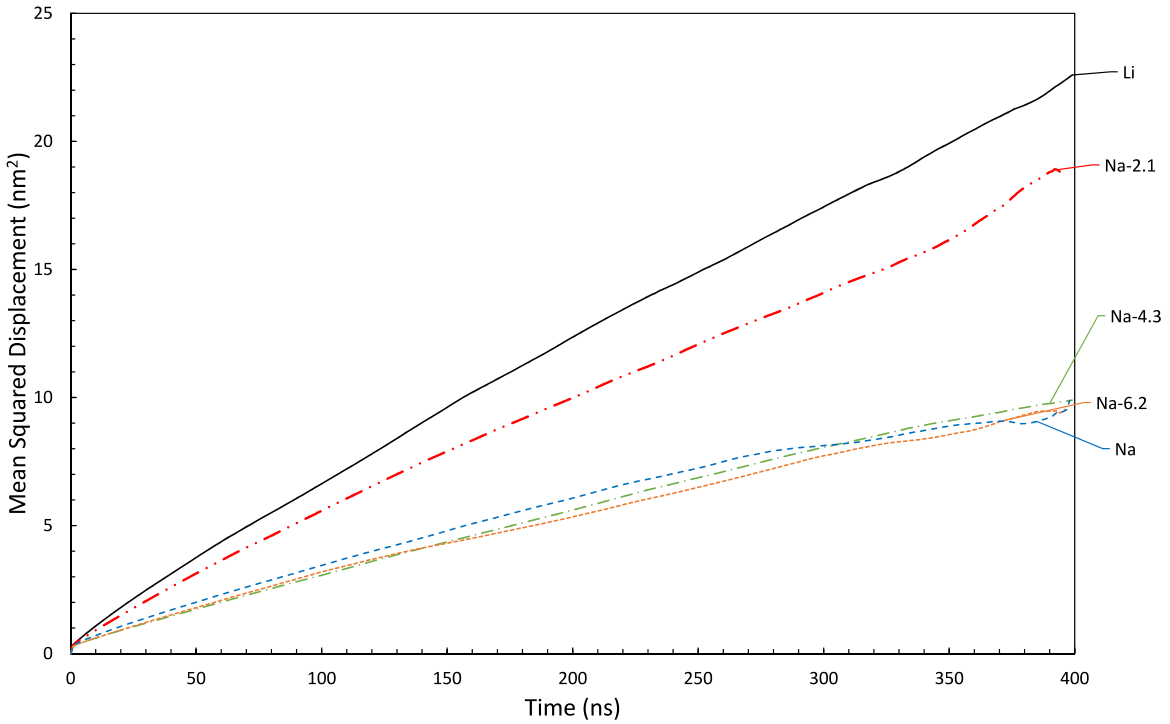

Figure 6.11: Variation of mean squared displacement at 600 K with 100 molecules of adsorbed CO_2/2 x 2 x 2 supercell for increasing Na^+ contents following 600 ns of equilibration

Table 6.10: Estimate of diffusion coefficients at 600 K based on 100 molecules CO_2/2 x 2 x 2 supercell

System	Estimate of D (x 10^9 cm^2/s)
Li-RHO	3.050
Na-2.1	2.467
Na-4.3	1.318
Na-6.2	1.271
Na-RHO	1.275

Figure 6.11 and Table 6.10 suggest that as the Na^+ content increases, a critical concentration is reached after which additional Na^+ does not change the overall CO_2 diffusion rate. (The diffusion rates for $Li_{7.7}Na_{4.3}$-RHO, $Li_{5.4}Na_{6.2}$-RHO and Na-RHO systems are very similar.)

Table 6.11 shows a gradual progression in cation occupancy of the 8MR from 2.6 to 4.25 cations/unit cell in the 8MR windows. The 8MRs are preferentially filled by Na^+ rather than Li^+, so the critical Na^+ occupancy is between 1.625 and 3 8MR cations/unit cell. This corresponds to between 2.1 Na^+ and 4.3 Na^+ out of a total of 9.8 cations/unit cell i.e. between ≈20-40% Na^+ content.

Table 6.11: Cation siting in CO_2 simulations

Cation	Framework	Unmatched	D8R	S8R	6MR
Li	Na-2.1	0	0	1.625	6
Li	Na-4.3	0	0	0.375	5
Li	Na-6.2	0	0	0.375	3.25
Na	Na-2.1	0	0	1.625	0.5
Na	Na-4.3	0	0	3	1.375
Na	Na-6.2	0	0	3.75	2.375
Total	Li-RHO	0	0	2.625	7.125
Total	Na-2.1	0	0	3.25	6.5
Total	Na-4.3	0	0	3.375	6.375
Total	Na-6.2	0	0	4.125	5.625
Total	Na-RHO	0	0	4.25	5.5

6.5. Concluding remarks

In this section, it has been shown that substantial pore size modification is possible by changing the Si/Al ratio (Figure 6.1). In the known range of zeolite compositions (Si/Al = 1.9 to 27), it is possible to adjust the limiting pore diameter of the 8MR between 4.85 Å and 5.35 Å (Figure 6.1) by changing the Si/Al ratio. The peak CO_2 uptake was found at 10 cations/unit cell where experimental work is already focussed.

The simulation of Li-RHO is a greater challenge than Na-RHO. In part this is due to the presence of water in the experimental refinements but even if water is added to the simulation, the large increase in cell volume observed experimentally is not yet captured by the simulations (Figure 6.7). It is interesting to note that the addition of water molecules has a greater impact on the unit cell length than the addition of CO_2 molecules. This occurs because the H_2O is drawn strongly to the cation and sits alongside it in the 8MR. Due to the flexible nature of RHO, the unit cell expands to accommodate the complex, much as it would with a larger cation.

The difficulty in modelling Li-RHO propagates into the modelling of Li/Na mixtures. Qualitatively however, the expected trends are identified. The Li^+ cations prefer the 6MR and the Na^+ cations prefer the 8MR. For the mixed systems, as the Na^+ content increases the 8MR sites are increasingly populated (Table 6.11) and CO_2 diffusion also becomes more difficult. For Na^+ compositions above 40%, the diffusion rate remains constant as the Na^+ content increases (Figure 6.11) with the critical Na^+ content being reached at about 3 Na^+/unit cell.

7. Summary and Future Work

Using molecular simulations, this work has investigated the RHO family of zeolites for use as industrial adsorbents. Zeolite RHO is particularly promising in this regard as it offers enhanced selectivities through cation-gating separation. RHO is also an usually flexible zeolite where the limiting window diameter (hence kinetic selectivity) can be adjusted by changing the Si/Al ratio and through ion-exchange, the extraframework cations.

After introducing the simulation techniques used and the physical properties of RHO (Chapters 1 and 2), this work focuses first on finding a suitable forcefield to model zeolite RHO (Chapter 3). Due to the flexible nature of RHO, off-the-shelf forcefields do not sufficiently capture both the framework flexibility and the expected interaction energies with CO_2 (in the form of adsorption isotherms). Therefore in Chapter 3, the forcefield by Gabrieli et al. [46] is adjusted to improve the agreement with the bond lengths and bond angles observed in *ab initio* molecular dynamics simulations of Na-RHO. These modifications led to a significant improvement in the size and shape of the windows compared to both experimental work and DFT observations.

In the Gabrieli et al. [46] forcefield, the flexibility of bonds and angle bends is described using a harmonic approximation. For the modifications to the forcefield in this work, only the values of the equilibrium bond lengths and equilibrium bond angles have been varied. This assumes that i) the equilibrium values are simply offset from their true value and ii) the strength of the interactions captured by the spring constants are correct. In the future it is recommended that, following the methodology of Gabrieli et al. [46], power spectra are generated from DFT simulations and then the classical MD parameters adjusted to reproduce these spectra. This would allow optimisation of both the spring constants and the equilibrium values.

In addition to optimising the bonded parameters, significant attention has been given to understanding the effect of the cation parameters used. This has shown that the Lennard-Jones sigma value is responsible for the distribution of the cations between the 8MRs and the 6MRs and that the cation sitings are largely independent of the epsilon value. However, the effect of epsilon is more significant when considering gas adsorption and cell expansion. Full forcefield optimisation therefore requires an additional iterative layer adjusting both Lennard-Jones parameters and bonded interactions. The problem is complicated further by the need to adjust the cation-oxygen parameter independently of the other cation cross terms (Section 3.6.5).

In Section 3.7, reference is made to a study [54] where bonded torsional parameters were used to improve the agreement in window distortion. In this work, the Coulombic scale factor is used to compensate for the lack of torsional potentials. This is only an approximation and the cell dimension reproduced has some dependence on the location of the cations and aluminium atoms. Long term this is not desirable as the force field parameters should hold for all RHO zeolites, independent of the number and type of cations (without requiring continual calibration against experimental data).

As well as adding torsional parameters, it has been suggested that bonded 1-5 interactions may be needed [56]. As with the torsional parameters, atoms connected by four bonds can be located in close geometric vicinity of each other (e.g. in a 4MR) and this may justify additional exclusion policies and pseudo bond stretches.

From both a computational and experimental standpoint, the presence of water in the framework is an extra challenge. In Chapter 6, it is shown that the presence of one water molecule/unit cell changes the unit cell length of Na-RHO (Si/Al=3.9) from 14.35 Å to 14.41 Å. To calibrate force field models without water present, experimental samples must therefore be heated to a high temperature to ensure

full dehydration. Care must also be taken to ensure that the structure does not become amorphous (Chapter 3). When adsorbing gases and measuring cell expansion and gas uptake, it is also difficult to ensure that the sample is completely dry both initially and after loading. In simulations, water represents one of the most challenging molecules to model reliably. This is seen in both classical and DFT approaches, where the addition of water molecules failed to satisfactorily reproduce the experimental unit cell expansion seen in hydrated Li-RHO. (The agreement for 1 molecule of water/ unit cell for Na-RHO is better).

Despite the difficulties faced with the forcefield, qualitative strides have been made towards understanding the CO_2 diffusion mechanism in Na-RHO (Chapter 4). The cation-gating mechanism suggested by Lozinska et al. [8], which is based on chemical intuition, has been observed in classical simulations and the energy barriers for CO_2 diffusion in these simulations correspond to those predicted from DFT simulations [45]. In addition, a second mechanism for CO_2 diffusion has been observed for cases where there is no cation present in the D8R. Here CO_2 enters normal to the D8R cage, undergoes a 90 degree rotation when it is encapsulated fully by the D8R and then exits again normal to the D8R cage.

In order to observe CO_2 diffusion, the temperature of the simulation has to be raised to between 400 K and 600 K. Experimentally, CO_2 diffusion is expected at 300 K therefore this is an indication that the force field requires some further optimisation. Although useful for observing the trapdoor behaviour, the increased temperature biases the simulations towards increased diffusion as the framework, as well as the cations, possess more energy than expected.

In Chapter 5, the 600 K diffusion studies are extended to gases other than CO_2. These shows that helium has a very high diffusivity through Na-RHO, being small enough to cross both the 8MRs and 6MRs. Krypton and xenon are both effectively blocked by Na^+ cations, whilst argon shows low diffusivity through Na-RHO. O_2

and N_2 both show moderate diffusivity through Na-RHO with larger N_2 being slower than O_2. Unlike experimental work, CH_4 shows no intercage diffusion.

Chapter 6 examines first the pore size modification possible by changing the Si/Al ratio and then more generally the effect of adjusting the Li/Na cation composition. When adjusting the Si/Al ratio, the work assumes that the 1-4 Coulombic scale factor calibration against the Si/Al ratio of 3.9 observed experimentally [8] holds across the entire Si/Al range. This potentially limits the quantitative predictions which can be made but does show that on a qualitative basis, substantial alterations to the limiting 8MR window diameter are possible by adjust the Si/Al ratio.

When gradually varying the cation composition from pure Li-RHO to pure Na-RHO, three main effects are observed: i) an expansion in unit cell volume, ii) enhanced equilibrium uptake of CO_2 and iii) a sudden drop in CO_2 diffusivity. As well as the pure Li-RHO and Na-RHO zeolites, $Li_{7.7}Na_{2.1}$, $Li_{5.4}Na_{4.3}$ and$Li_{3.6}Na_{6.2}$ RHO are also examined. Li-RHO has the highest CO_2 diffusion rate, with a 20% reduction observed for $Li_{7.7}Na_{2.1}$-RHO. The remaining RHO zeolites all have comparable diffusion rates which are approximately 50% lower than Li-RHO. This suggests that beyond a critical Na^+ content, no change in diffusion rate is observed and this is attributed to reaching a critical number of blocking Na^+ cations in the 8MRs.

In summary, whilst qualitative/semi-quantitative predictions can be made with relative ease, to predict reliably both the diffusion rates and gas uptake with finer accuracy, further optimisation of the force field is required. Once this point is reached, it would also be possible to easily extend the work to other zeolites which share a similar topology. Particularly of interest are PAU, ZSM-25, PST-20 and PST-25 [138] which all have additional secondary building units separating the *lta* cages. These, amongst other 8MR zeolites, offer promise for cation-gating

separations and by adjusting the Si/Al ratio and cation content it is likely that the performance of these zeolites can be improved further.

8. Works Cited

[1] D. S. Sholl and R. P. Lively, "Seven chemical separations to change the world," *Nature,* vol. 532, no. 7600, pp. 435-437, 2016.

[2] R. S. Haszeldine, "Carbon Capture and Storage: How green can black be?," *Science,* vol. 325, no. 5948, pp. 1647-1652, 2009.

[3] J. Vitillo, B. Smit and L. Gagliardi, "Introduction: Carbon Capture and Separation," *Chemical Reviews,* vol. 117, no. 14, pp. 9521-9523, 2017.

[4] R. Sinnott and G. Towler, Chemical Engineering Design: Fifth Edition, Oxford: Elsevier, 2009.

[5] N. Notman, "MOFs find a use," *Chemistry World,* 28 March 2017.

[6] J. Shang, G. Li, R. Singh, Q. Gu, K. M. Nairn, T. J. Bastow, N. Medhekar, C. M. Doherty, A. J. Hill, J. Z. Liu and P. A. Webley, "Discriminative Separation of Gases by a "Molecular Trapdoor" Mechanism in Chabazite Zeolites," *Journal of the American Chemical Society,* vol. 134, no. 46, p. 19246–19253, 2012.

[7] M. M. Lozinska, J. P. S. Mowat, P. A. Wright, S. P. Thompson, J. L. Jorda, M. Palomino, S. Valencia and F. Rey, "Cation Gating and Relocation during the Highly Selective "Trapdoor" Adsorption of CO_2 on Univalent Cation Forms of Zeolite RHO," *Chemistry of Materials,* vol. 26, no. 6, p. 2052–2061, 2014.

[8] M. M. Lozinska, E. Mangano, J. P. S. Mowat, A. M. Shepherd, R. F. Howe, S. P. Thompson, J. E. Parker, S. Brandani and P. A. Wright, "Understanding Carbon Dioxide Adsorption on Univalent Cation Forms of the Flexible

Zeolite RHO at Conditions Relevant to Carbon Capture from Flue Gases," *Journal of the American Chemical Society,* vol. 134, no. 42, p. 17628–17642, 2012.

[9] H. E. Robson, D. P. Shoemaker, R. A. Ogilvie and P. C. Manor, "Synthesis and crystal structure of zeolite rho - a new zeolite related to Linde Type A," *Advances in Chemistry (Molecular Sieves),* vol. 121, pp. 106-115, 1973.

[10] International Zeolite Association (IZA), "Framework RHO," 1978. [Online]. Available: http://www.iza-structure.org/IZA-SC/framework.php?STC=RHO. [Accessed 22 May 2018].

[11] Y. G. Bushuev and G. Sastre, "Feasibility of Pure Silica Zeolites," *Journal of Physcial Chemistry C,* vol. 114, no. 45, p. 19157–19168, 2010.

[12] J. Weitkamp and L. Puppe, Catalysis and Zeolites: Fundamentals and Applications, New York: Springer, 2013.

[13] C. R. A. Catlow, A. R. George and C. M. Freeman, "Ab initio and molecular-mechanics studies of aluminosilicate fragments, and the origin of Lowenstein's rule," *Chemical Communications,* no. 11, pp. 1311-1312, 1996.

[14] J. B. Parise, L. Abrams, T. E. Gier, D. R. Corbin, J. D. Jorgensen and E. Prince, "Flexibility of the Framework of Zeolite RHO. Structural Variation from 11 to 573 K. A Study Using Neutron Powder Diffraction Data," *Journal of Physical Chemistry,* vol. 88, no. 11, pp. 2303-2307, 1984.

[15] S. R. G. Balestra, J. J. Gutiérrez-Sevillano, P. J. Merkling, D. Dubbeldam and S. Calero, "Simulation Study of Structural Changes in Zeolite RHO," *Journal of Physical Chemistry C,* vol. 117, no. 22, pp. 11592-11599, 2013.

[16] S. R. G. Balestra, S. Hamad, A. R. Ruiz-Salvador, V. D. Garcia, P. J. Merkling, D. Dubbeldam and S. Calero, "Understanding nanopore window distortions

in the reversible molecular valve zeolite RHO," *Chemistry of Materials,* vol. 27, no. 16, p. 5657–5667, 2015.

[17] J. Dědeček, Z. Sobalík and B. Wichterlová, "Siting and Distribution of Framework Aluminium Atoms in Silicon-Rich Zeolites and Impact on Catalysis," *Catalysis Reviews,* vol. 54, no. 2, pp. 135-223, 2012.

[18] J. Dedecek, M. J. Lucero, C. Li, F. Gao, P. Klein, M. Urbanova, Z. Tvaruzkova, P. Sazama and S. Sklenak, "Complex Analysis of the Aluminum Siting in the Framework of Silicon-Rich Zeolites. A Case Study on Ferrierites," *The Journal of Physical Chemistry C,* vol. 115, no. 22, pp. 11056-11064, 2011.

[19] S. Sklenak, J. Dedecek, C. Li, B. Wichterlova, V. Gabova, M. Sierka and J. Sauer, "Aluminium siting in the ZSM-5 framework by combination of high resolution ^{27}Al NMR and DFT/MM calculations," *Phys Chem Chem Phys,* vol. 11, no. 8, pp. 1237-47, 2009.

[20] R. E. Fletcher, S. Ling and B. Slater, "Violations of Lowenstein's rule in zeolites," *Chem Sci,* vol. 8, no. 11, pp. 7483-7491, 2017.

[21] W. Löwenstein, "The Distribution of Aluminum in the Tetrahedra of Silicates and Aluminates," *American Mineralogist,* vol. 39, no. 1-2, pp. 92-96, 1954.

[22] E. Dempsey, G. H. Kuehl and D. H. Olson, "Variation of the lattice parameter with aluminum content in synthetic sodium faujasites. Evidence for ordering of the framework ions," *The Journal of Physical Chemistry,* vol. 73, no. 2, pp. 387-390, 1969.

[23] S. M. Auerbach, K. A. Carrado and P. K. Dutta, Handbook of Zeolite Science and Technology, New York: Marcel-Decker, 2003.

[24] R. Szostak and R. F. T. Stepto, Molecular Sieves: Principles of Synthesis and Identification, London: Thomson-Science, 1998.

[25] J. V. Selinger, Introduction to the theory of matter from ideal gases to liquid crystals, Switzerland: Springer, 2016.

[26] M. S. Shell, Thermodynamics and Statistical Mechanics: An Integrated Approach, Cambridge: Cambridge University Press, 2015.

[27] M. Tuckerman, Statistical Mechanics: Theory and Molecular Simulation, Oxford: OUP, 2010.

[28] D. Frenkel and B. Smit, Understanding molecular simulation: From algorithms to Applications, London: Elsevier, 2002.

[29] N. Metropolis, A. W. Rosenbluth, M. N. Rosenbluth and A. H. Teller, "Equation of State Calculations by Fast Computing Machines," *Journal of Chemical Physics,* vol. 21, no. 6, pp. 1087-1092, 1953.

[30] J. Smith, H. V. Ness, Abbott and M. M., Introduction to Chemical Engineering Thermodynamics, New York: McGraw Hill, 2005.

[31] M. P. Allen and D. J. Tildesley, Computer Simulation of Liquids: Second Edition, Oxford: OUP, 2017.

[32] W. Swope, H. C. Anderson, P. Berens and K. Wilson, "A computer simulation method for the calculation of equilibrium constants for the formation of physical clusters of molecules: Application to small water clusters," *Journal of Chemical Physics,* vol. 76, no. 637, pp. 637-649, 1982.

[33] A. I. Skoulidas and D. S. Sholl, "Transport Diffusivities of CH_4, CF_4, He, Ne, Ar, Xe, and SF_6 in Silicalite from Atomistic Simulations," *J. Phys. Chem. B,* vol. 106, no. 19, p. 5058–5067, 2002.

[34] R. O. Dror, M. O. Jensen, D. W. Borhani and D. E. Shaw, "Exploring atomic resolution physiology on a femtosecond to millisecond timescale using molecular dynamics simulations," *J Gen Physiol,* vol. 135, no. 6, pp. 555-562, 2010.

[35] C. Niethammer, S. Becker, M. Bernreuther, M. Buchholz, W. Eckhardt, A. Heinecke, S. Werth, H. J. Bungartz, C. W. Glass, H. Hasse, J. Vrabec and M. Horsch, "ls1 mardyn: The Massively Parallel Molecular Dynamics Code for Large Systems," *J Chem Theory Comput,* vol. 10, no. 10, pp. 4455-4464, 2010.

[36] W. M. Meier, "Molecular Sieves," in *1st international Zeolite Conference*, London, 1967.

[37] J. B. Parise and E. Prince, "The structure of cesium-exchanged zeolite-RHO at 293 K and 493 K determined from high resolution neutron powder data," *Material Research Bulletin,* vol. 18, pp. 841-852, 1983.

[38] C. J. Tsiao, J. S. Kauffman, D. R. Corbin, L. Abrams, E. E. Carroll and C. Dybowski, "Xenon in zeolite Rho. Adsorption and xenon-129 NMR spectroscopy," *The Journal of Physical Chemistry,* vol. 95, no. 14, pp. 5586-5591, 1991.

[39] J. B. Parise, D. R. Corbin and L. Abrams, "Structural changes upon sorption and desorption of Xe from Cd-exchanged zeolite rho: a real-time synchrotron X-ray powder diffraction study," *Microporous materials,* vol. 4, no. 2-3, pp. 99-110, 1995.

[40] J. Parise, "Structural Case Studies of Inclusion Phenomena in Zeolites: Xe in zeolites: Xe in RHO and stilbene in ZSM-5," *Journal of inclusion phenomena and molecular recognition in chemistry,* vol. 21, no. 1-4, pp. 79-112, 1995.

[41] M. Palomino, A. Corma, J. L. Jorda, F. Rey and S. Valencia, "Zeolite RHO: a highly selective adsorbent for CO_2/CH_4 separation," *Chemical Communications,* vol. 48, p. 215–217, 2012.

[42] J. Shang, G. Li, R. Singh, P. Xiao, J. Z. Liu and P. A. Webley, "Determination of Composition Range for "Molecular Trapdoor" Effect in Chabazite Zeolite," *The Journal of Physical Chemistry C,* vol. 117, no. 24, pp. 12841-12847, 2013.

[43] M. M. Lozinska, E. Mangano, A. G. Greenaway, R. Fletcher, S. P. Thompson, C. A. Murray, S. Brandani and P. A. Wright, "Cation Control of Molecular Sieving by Flexible Li-Containing Zeolite RHO," *Journal of Physical Chemistry C,* vol. 120, no. 35, pp. 19652-19662, 2016.

[44] N. Bamberger and D. Kohen, "Atomistic Simulations of CO_2 During "Trapdoor" Adsorption onto Na-RHO zeolite," in *Foundations of Molecular Modeling and Simulation: Select Papers from FOMMS 2015*, Singapore, Springer, 2016, pp. 153-168.

[45] F. X. Coudert and D. Kohen, "Molecular Insight into CO_2 "Trapdoor" Adsorption in Zeolite Na-RHO," *Chemistry of Materials,* vol. 7, no. 2724-2730, p. 29, 2017.

[46] A. Gabrieli, M. Sant, P. Demontis and G. B. Suffritti, "Development and Optimization of a New Force Field for Flexible Aluminosilicates, Enabling Fast Molecular Dynamics Simulations on Parallel Architectures," *Journal of Physical Chemistry C,* vol. 117, no. 1, p. 503–509, 2013.

[47] A. K. Rappe, C. J. Casewit, K. S. Colwell, W. A. Goddard and W. M. Skiff, "UFF, a Full Periodic Table Force Field for Molecular Mechanics and

Molecular Dynamics Simulations," *Journal of the American Chemical Society,* vol. 114, no. 25, pp. 10024-10035, 1992.

[48] J. Aqvist, "Ion Water Interaction Potentials Derived from Free-Energy Perturbation Simulations," *Journal of Physical Chemistry,* Vols. 8021-8024, p. 94, 1990.

[49] E. Akten, R. Siriwardane and D. Sholl, "Monte Carlo Simulation of Single- and Binary-Component Adsorption of CO_2, N_2, and H_2 in Zeolite Na-4A," *Energy & Fuels,* vol. 17, pp. 977-983, 2003.

[50] M. Sanders, M.Leslie and C. Catlow, "Interatomic Potentials for SiO_2," *Journal of the Chemical Society, Chemical Communications,* no. 19, pp. 1271-173, 1984.

[51] J. R. Hill and J. Sauer, "Molecular Mechanics Potential forMolecular Mechanics Potential for Silica and Zeolite Catalysts Based on ab Initio Calculations. 2. Aluminosilicates," *Journal of Physical Chemistry,* vol. 99, no. 23, pp. 9536-9550, 1995.

[52] R. A. Jackson and C. R. A. Catlow, "Computer Simulation Studies of Zeolite Structure," *Molecular Simulation,* vol. 1, no. 4, pp. 207-224, 1988.

[53] R. Jackson, R. Bell and C. Catlow, "Studies in Surface Science and Catalysis," *Molecular Simulation,* vol. 52, pp. 203-208, 1988.

[54] S. E. Boulfelfel, P. I. Ravikovitch, L. Koziol and D. S. Sholl, "Improved Hill–Sauer Force Field for Accurate Description of Pores in 8-Ring Zeolites," *Journal of Physical Chemistry C,* vol. 120, no. 26, p. 14140–14148, 2016.

[55] M. Jeffroy, C. Nieto-Draghi and A. Boutin, "Molecular simulation of zeolite flexibility," *Molecular simulation,* vol. 40, no. 1-3, pp. 6-15, 2014.

[56] A. Gabrieli, M. Sant, P. Demontis and G. B. Suffritti, "Fast and efficient optimization of Molecular Dynamics force fields for microporous materials: Bonded interactions via force matching," *Microporous and Mesoporous Materials,* vol. 197, pp. 339-347, 2014.

[57] B. Zheng, M. Sant, P. Demontis and G. B. Suffritti, "Force Field for Molecular Dynamics Computations in Flexible ZIF-8 Framework," *Journal of Physical Chemistry C,* vol. 116, no. 1, pp. 933-938, 2011.

[58] J. G. Harris and K. H. Yung, "Carbon Dioxide's Liquid-Vapor Coexistence Curve and Critical Properties As Preducicted by a Simple Molecular Model," *The Journal of Physical Chemistry,* vol. 99, no. 31, pp. 12021-12024, 1995.

[59] A. Martin-Calvo, J. Parra, C. Ania and S. Calero, "Insights on the Anomalous Adsorption of Carbon Dioxide in LTA Zeolites," *Journal of Physical Chemistry C,* vol. 118, no. 44, pp. 25460-25467, 2014.

[60] J. Potoff and J. Siepmann, "Vapor-liquid equilibria of mixtures containing alkanes, carbon dioxide and nitrogen," *AIChE Journal,* vol. 47, pp. 1676-1682, 2001.

[61] GROMACS v2018.1 manual.

[62] M. Lundborg and E. Lindahl, "Automatic GROMACS topology generation and comparisons of force fields for solvation free energy calculations," *J Phys Chem B,* vol. 119, no. 3, pp. 810-823, 2015.

[63] P. Demontis, G. B. Suffritti, S. Quartieri, E. S. Fois and A. Gamba, "Molecular-Dynamics Studies on Zeolites .3. Dehydrated Zeolite-A," *Journal of Physical Chemistry,* vol. 92, no. 4, pp. 867-871, 1988.

[64] B. R. Brooks, R. E. Bruccoleri, B. D. Olafson, D. J. Slates, S. Swaminathan and M. Karplus, "CHARMM: A program for macromolecular energy, minimization, and dynamics calculations," *Journal of Computational Chemistry,* vol. 4, no. 2, pp. 187-217, 1983.

[65] J. D. Gale and A. L. Rohl, "The General Utility Lattice Program (GULP)," *Molecular Simulation,* vol. 29, no. 5, pp. 291-341, 2003.

[66] I. T. Todorov, W. T. K. Smith and M. T. Dove, "DL_POLY_3: new dimensions in molecular dynamics simulations via massive parallelism," *Journal of Materials Chemistry,* vol. 16, no. 20, pp. 1911-1918, 2003.

[67] J. I. M. S. F. a. V. J. Hutter, "CP2K: atomistic simulations of condensed matter systems," *Wiley Interdisciplinary Reviews: Computational Molecular Science,* vol. 4, no. 1, p. 15–25, 2013.

[68] M. Sant, A. Gabrieli, P. Demontis and G. B.Suffritti, "InfiniCharges: A tool for generating partial charges via the simultaneous fit of multiframe electrostatic potential (ESP) and total dipole fluctuations (TDF)," *Computer Physics Communications,* vol. 200, pp. 190-198, 2016.

[69] A. García-Sánchez, C. O. Ania, J. B. Parra, D. Dubbeldam, T. J. H. Vlugt, R. Krishna and S. Calero, "Transferable Force Field for Carbon Dioxide Adsorption in Zeolites," *Journal of Physical Chemistry C,* vol. 113, no. 20, pp. 8814-8820, 2009.

[70] E. Beerdsen, D. Dubbeldam, B. Smit, T. J. H. Vlugt and S. Calero, "Simulating the Effect of Nonframework Cations on the Adsorption of Alkanes in MFI-type Zeolites," *Journal of Physical Chemistry B,* vol. 107, no. 44, pp. 12088-12096, 2003.

[71] I. Biosym Technologies, *CVFF forcefield file in new format, converted from original format file shipped with Discover 2.6.0 / InsightII 1.1.0 / Insight 2.6,* 1990.

[72] R. T. Cygan, J. J. Liang and A. G. Kalinichev, "Molecular models of hydroxide, oxyhydroxide, and clay phases and the development of a general force field," *Journal of Physical Chemistry B,* vol. 108, no. 4, pp. 1255-1266, 2004.

[73] S. L. Mayo, B. D. Olafson and W. A. I. Goddard, "DREIDING: A generic force field for molecular simulations," *Journal of Physical Chemistry,* vol. 94, no. 26, pp. 8897-8909, 1990.

[74] T. Halicioğlu and G. Pound, "Calculation of potential energy parameters form crystalline state properties," *Physica Status Solidi (a),* vol. 30, no. 2, pp. 619-623, 1975.

[75] E. Jaramillo and M. Chandross, "Adsorption of Small Molecules in LTA Zeolites. 1. NH_3, CO_2, and H_2O in Zeolite 4A," *Journal of Physical Chemistry B,* vol. 108, no. 52, p. 20155–20159, 2004.

[76] K. Jensen and W. L. Jorgensen, "Halide, Ammonium, and Alkali Metal Ion Parameters for Modeling Aqueous Solutions," *Journal of Chemical Theory and Computation,* vol. 2, no. 6, pp. 1499-1509, 2006.

[77] G. Lamoureux and B. Roux, "Absolute Hydration Free Energy Scale for Alkali and Halide Ions Established from Simulations with a Polarizable Force Field," *Journal of Physical Chemistry B,* vol. 110, no. 7, pp. 3308-3322, 2006.

[78] J. P. Larentzos, W. Schneider and E. Maginn, "Transferable force field for water adsorption in cation-exchanged titanosilicates," *Industrial & Engineering Chemistry Research,* vol. 46, no. 17, pp. 5754 - 5765, 2007.

[79] S. H. Lee and J. C. Rasaiah, "Molecular dynamics simulation of ionic mobility. I. Alkali metal cations in water at 25 °C," *Journal of Chemical Physics,* vol. 101, pp. 6964-6974, 1994.

[80] G. Maurin, P. Llewellyn, T. Poyet and B. Kuchta, "Influence of Extra-Framework Cations on the Adsorption Properties of X-Faujasite Systems: Microcalorimetry and Molecular Simulations X-Faujasite Systems: Microcalorimetry and Molecular Simulations," *Journal of Physical Chemistry B,* vol. 109, no. 1, p. 125–129, 2005.

[81] B. G. Rao and U. C. Singh, "A Free Energy Pertubtation Study of Solvation in Methanol and Dimethyl Sulfoxide," *Jorunal of the American Chemical Society,* vol. 112, no. 10, pp. 3803-3811, 1990.

[82] B. Vujić and A. P. Lyubartsev, "Transferable force-field for modelling of CO_2, N_2, O_2 and Ar in all silica and Na+ exchanged zeolites," *Modelling and Simulation in Materials Science and Engineering,* vol. 24, no. 4, pp. 1-26, 2016.

[83] K. Watanabe, N. Austin and M. R. Stapleton, "Investigation of the Air Separation Properties of Zeolites Types A, X and Y by Monte Carlo Simulations," *Molecular Simulation,* vol. 15, no. 4, pp. 197-221, 1995.

[84] G. Tribello, M. Bonomi, D. Branduardi, C. Camilloni and G. Bussi, "PLUMED 2: New feathers for an old bird," *Computer Physics Communications,* vol. 185, no. 2, pp. 604-613, 2014.

[85] Y. Lee, J. C. Reisner, J. C. Hanson, G. A. Jones, J. B. Parise, D. R. Corbin, B. H. Toby, A. Freitag and J. Z. Larese, "New insight into cation relocations within the pores of zeolite RHO: In situ synchrotron X-ray and neutron powder diffraction studies of Pb- and Cd-exchanged Rho," *J. Phys Chem B.,* vol. 105, no. 30, pp. 7188 - 7199, 2001.

[86] P. D. J. Grootenhuis and P. A. Kollman, "Molecular Mechanics and Dynamics Studies of Crown Ether Cation Interactions - Free-Energy Calculations on the Cation Selectivity of Dibenzo-18-Crown-6 and Dibenzo-30-Crown-10," *Journal of the American Chemical Society,* vol. 111, no. 6, pp. 2152-2158, 1989.

[87] J. A. Purton, J. C. Crabtree and S. C. Parker, "DL_MONTE: a general purpose program for parallel," *Molecular Simulation,* vol. 39, no. 14-15, pp. 1240-1252, 2013.

[88] A. Martin-Calvo, J. J. Gutierrez-Sevillano, J. B. Parra, C. O. Ania and S. Calero, "Transferable force fields for adsorption of small gases in zeolites," *Phys Chem Chem Phys,* vol. 17, no. 37, pp. 24048-24055, 2015.

[89] M. Rouha and I. Nezbeda, "Non-Lorentz–Berthelot Lennard-Jones mixtures: A systematic study," *Fluid Phase Equilibria,* vol. 277, no. 1, pp. 42-48, 2009.

[90] W. Song, P. J. Rossky and M. Maroncelli, "Modeling alkane+perfluoroalkane interactions using all-atom potentials: Failure of the usual combining rules," *The Journal of Chemical Physics,* vol. 119, no. 17, pp. 9145-9162, 2003.

[91] J. Delhommelle and P. Millié, "Inadequacy of the Lorentz-Berthelot combining rules for accurate predictions of equilibrium properties by molecular simulation," *Molecular Physics,* vol. 99, no. 8, pp. 619-625, 2001.

[92] J. Wong-Ekkabut and M. Karttunen, "The good, the bad and the user in soft matter simulations," *Biochim Biophys Acta,* vol. 1858, no. 10, pp. 2529-2538, 2016.

[93] A. Patriksson and D. van der Spoel, "A temperature predictor for parallel tempering simulations," *Phys Chem Chem Phys,* vol. 10, no. 15, pp. 2073-2077, 2018.

[94] W. L. Jorgensen, D. S. Maxwell and J. Tirado-Rives, "Development and Testing of the OPLS All-Atom Force Field on Conformational Energetics and Properties of Organic Liquids," *Journal of the American Chemical Society,* vol. 118, no. 45, pp. 11225-11236, 1996.

[95] Y. Duan, C. Wu, S. Chowdury, M. C. Lee, G. Xiong, W. Zhang, R. Yang, P. Cieplak, R. Luo, T. Lee, J. Caldwell, J. Wang and P. Kollman, "A point-charge force field for molecular mechanics simulations of proteins based on condensed-phase quantum mechanical calculations," *J Comput Chem,* vol. 24, no. 16, pp. 1999-2012, 2003.

[96] A. Ghysels, S. L. C. Moors, K. Hemelsoet, K. De Wispelaere, M. Worquier, G. Sastre and V. Van Speybroech, "Shape-Selective Diffusion of Olefins in 8-Ring Solid Acid Microporous Zeolites," *The Journal of Physical Chemistry C,* vol. 119, no. 41, pp. 237721-23734, 2015.

[97] F. Liu, Advances in Applied and Computational Mathematics, New York: Nova Science Publishers, Inc., 2006.

[98] R. J. Carroll and D. Ruppert, "The Use and Misuse of Orthogonal Regression in Linear Errors-in-Variables Models," *The American Statistician,* vol. 50, no. 1, pp. 1-6, 1996.

[99] M. J. Saxton, "Modelling 2D and 3D diffusion," in *Methods in Membrane Lipids*, Totowa, New Jersey, Springer Science & Business Media, 2007, pp. 295-322.

[100] L. Chen, P. S. Reiss, S. Y. Chong, D. Holden, K. E. Jelfs, T. Hasell, M. A. Little, A. Kewley, M. E. Briggs, A. Stephenson, K. M. Thomas, J. A. Armstrong, J. Bell, J. Busto, R. Noel, J. Liu, D. M. Strachan, P. K. Thallapally and A. Cooper, "Separation of rare gases and chiral molecules by selective

binding in porous organic cages," *Nature Materials,* vol. 13, no. 10, pp. 954-960, 2014.

[101] Z. Liu, Y. Wu, B. Liu, S. C. Oh, W. Fan, Y. Qian and H. Xi, "Tuning the adsorption and separation properties of noble gases and N_2 in CuBTC by ligand functionalization," *RSC Advances,* vol. 6, no. 94, pp. 91093-91101, 2016.

[102] Z. Liu, A. T. Y. Okajima, M. Albert and H. Hatabu, "Pulmonary hyperpolarized noble gas MRI: recent advances and perspectives in clinical application.," *European Journal of Radiology,* vol. 83, no. 7, pp. 1282-1291, 2014.

[103] N. P. Franks, R. Dickinson, S. L. M. de Sousa, Hall. A. C. and W. R. Lieb, "How does xenon produce anaesthesia?," *Nature,* vol. 396, no. 6709, p. 324, 1998.

[104] N. Saito, Y. Ogawa, Y. Saso, C. Liao and R. Sakei, "Flame-extinguishing concentrations and peak concentrations of N_2, Ar, CO_2 and their mixtures for hydrocarbon fuels," *Fire safety journal,* vol. 27, no. 3, pp. 185-200, 1996.

[105] K. E. Grund, D. Storek and G. Farin, "Endoscopic argon plasma coagulation (APC) first clinical experiences in flexible endoscopy.," *Endoscopic Surgery and Allied Technologies,* vol. 2, no. 1, pp. 42-46, 1994.

[106] A. Durgutlu, "Experimental investigation of the effect of hydrogen in argon as a shielding gas on TIG welding of austenitic stainless steel," *Materials & Design,* vol. 25, no. 1, pp. 19-23, 2004.

[107] S. S. Hashim, A. R. Mohamed and S. Bhatia, "Oxygen separation from air using ceramic-based membrane technology for sustainable fuel production

and power generation," *Renewable and Sustainable Energy Reviews,* vol. 15, no. 2, pp. 1284-1293, 2011.

[108] R. S. Murali, T. Sankarshana and S. Sridhar, "Air Separation by Polymer-based Membrane Technology," *Separation & Purification Reviews,* vol. 42, no. 2, pp. 130-186, 2013.

[109] R. Stanger, T. Wall, R. Spörl, M. Paneru, S. Grathwohl, M. Weidmann, G. Scheffknecht, D. McDonald, K. Myöhänen, J. Ritvanen, S. Rahiala, S. Rahiala, T. Hyppänen, J. Mietzko, A. Kather and S. Santos, "Oxyfuel combustion for CO_2 capture in power plants," *International Journal of Greenhouse Gas Control,* no. 55-125, p. 40, 2015.

[110] S. P. S. Badwal and F. T. Ciacchi, "Ceramic Membrane Technologies for Oxygen Separation," *Advanced Materials,* vol. 13, no. 12-13, pp. 993-996, 2001.

[111] J. G. Hansel, "Oxygen," in *Kirk-Othmer Encyclopedia of Chemical Technology,* 2005, pp. 1-24.

[112] R. Lan, J. T. S. Irvine and S. Tao, "Synthesis of ammonia directly from air and water at ambient temperature and pressure," *Nature scientific reports,* vol. 3, p. 1145, 2013.

[113] D. D. Iarikov and S. T. Oyama, "Review of CO_2/CH_4 Separation Membranes," *Membrane Science and Technology,* vol. 14, pp. 91-115, 2011.

[114] E. Keskes, C. S. Adjiman and A. Galindo, "A Physical Absorption Process for the Capture of CO_2 from CO_2-Rich Natural gas Streams," in *2008 AIChE Annual Meeting*, 2008.

[115] M. Mofarahi and F. Gholipour, "Gas adsorption separation of CO_2/CH_4 system using zeolite 5A," *Microporous and Mesoporous Materials,* vol. 200, pp. 1-10, 2014.

[116] M. Thommes, K. Kaneko, A. V. Neimark, J. P. Olivier, F. Rodriguez-Reinoso, J. Rouqerol and K. S. W. Sing, "Physisorption of gases, with special reference to the evaluation of surface area and pore size distribution (IUPAC Technical Report)," *Pure and Applied Chemistry,* vol. 87, no. 9-10, 2015.

[117] P. Z. Moghadam, D. Fairen-Jimenez and R. Q. Snurr, "Efficient identification of hydrophobic MOFs: application in the capture of toxic industrial chemicals," *Journal of Materials Chemistry A,* vol. 4, no. 2, pp. 529-536, 2016.

[118] Y. Sun and S. Han, "Diffusion of N_2, O_2, H_2S and SO_2 in MFI and 4A zeolites by molecular dynamics simulations," *Molecular Simulation,* vol. 41, no. 13, pp. 1095-1109, 2014.

[119] T. Tomita, K. Nakayama and H. Sakai, "Gas separation characteristics of DDR type zeolite membrane," *Microporous and Mesoporous Materials,* vol. 68, no. 1-3, pp. 71-75, 2004.

[120] S. Sircar and A. L. Myers, "Gas Separation by Zeolites," in *Handbook of Zeolite Science and Technology*, New York, Marcel Dekker, Inc., 2003.

[121] M. Palomino, A. Corma, F. Rey and S. Valencia, "New Insights on CO_2–Methane Separation Using LTA Zeolites with Different Si/Al Ratios and a First Comparison with MOFs," *Langmuir,* vol. 26, no. 3, p. 1910–1917, 2010.

[122] T. Remy, S. A. Peter, L. Van Tendeloo, S. Van der Perre, Y. Lorgouilloux, C. E. A. Kirschhock, G. V. Baron and J. F. M. Denayer, "Adsorption and Separation of CO_2 on KFI Zeolites: Effect of Cation Type and Si/Al Ratio on Equilibrium and Kinetic Properties," *Langmuir,* vol. 29, no. 16, p. 4998–5012, 2013.

[123] Y. Ji, J. Birmingham, M. A. Deimund, S. K. Brand and M. E. Davis, "Steam-dealuminated, OSDA-free RHO and KFI-type zeolites as catalysts for the methanol-to-olefins reaction," *Microporous and Mesoporous Materials,* vol. 232, pp. 126-137, 2016.

[124] Q. Ke, T. Sun, H. Cheng, H. Chen, X. Liu, X. Wei and S. Wang, "Targeted Synthesis of Ultrastable High-Silica RHO Zeolite Through Alkali Metal-Crown Ether Interaction," *Chemistry An Asian Journal,* vol. 12, no. 10, pp. 1043-1047, 2017.

[125] C. Casada-Coterillo, A. Fernandez-Barquin, S. Valencia and A. Irabien, "Estimating CO_2/N_2 Permselectivity through Si/Al = 5 Small-Pore Zeolites/PTMSP Mixed Matrix Membranes: Influence of Temperature and Topology," *Membranes,* vol. 8, no. 2, pp. 1-15, 2018.

[126] E. Bruce, *Unpublished sample,* University of St. Andrews, 2018.

[127] A. J. Richard, K. Watanabe, N. Austin and M. R. Stapleton, "Computer simulation of the gas separation properties of zeolite Li-X," *Journal of Porous Materials,* vol. 2, no. 1, pp. 43-49, 1995.

[128] N. D. Hutson, S. C. Zajic and R. T. Yang, "Influence of Residual Water on the Adsorption of Atmospheric Gases in Li–X Zeolite: Experiment and Simulation," *Industrial & Engineering Chemistry Research,* vol. 39, no. 6, pp. 1775-1780, 2000.

[129] M. H. Kowsari, "Tracing Experimentally Compatible Dynamical and Structural Behavior of Atmospheric N_2/O_2 Binary Mixtures within Nanoporous Li–LSX Zeolite: New Insights to Influence of Extra-Framework Cations by MD Simulations," *Journal of Physical Chemistry C,* vol. 121, no. 3, pp. 1770-1780, 2017.

[130] N. Kumar and J. M. Seminario, "Lithium-Ion Model Behavior in an Ethylene Carbonate Electrolyte Using Molecular Dynamics," *Journal of Physical Chemistry C,* vol. 120, no. 30, pp. 16322-16332, 2016.

[131] J.-R. Hill, C. M. Freeman and L. Subramanian, "Use of Force Fields in Materials Modeling," *Reviews in Computational Chemistry,* vol. 16, pp. 141-216, 2007.

[132] M. A. Webb, B. M. W. Z.-G. Savoie and T. F. Miller III, "Chemically Specific Dynamic Bond Percolation Model for Ion Transport in Polymer Electrolytes," *Macromolecules,* vol. 48, no. 19, pp. 7346-7358, 2015.

[133] A. Wozniak, B. Marler, K. Angermund and H. Gies, "Water and Cation Distribution in Fully and Partially Hydrated Li-LSX Zeolite," *Chemistry of Materials,* vol. 20, no. 19, pp. 5968-5976, 2008.

[134] M. Lozinska, *Unpublished isotherm data,* 2018.

[135] M. Fischer, "Structure and bonding of water molecules in zeolite hosts: Benchmarking plane-wave DFT against crystal structure data," *Zeitschrift für Kristallographie - Crystalline Materials,* vol. 230, no. 5, 2015.

[136] P. Guo, J. Shin, A. G. Greenaway, J. G. Min, J. Su, H. J. Choi, L. Liu, P. A. Cox, S. B. Hong, P. A. Wright and X. Zou, "A zeolite family with expanding structural complexity and embedded isoreticular structures," *Nature,* vol. 524, no. 7563, pp. 74-78, 2015.

[137] M. Sant, J. M. Leyssale, G. K. Papadopoulos and D. N. Theodorou, "Molecular dynamics of carbon dioxide, methane and their mixtures in a zeolite possessing two independent pore networks as revealed by computer simulations," *J Phys Chem B,* vol. 113, no. 42, pp. 13761-13767, 2009.

[138] W. L. Jorgensen, J. Chandrasekhar, J. D. Madura, R. W. Impey and M. L. Klein, "Comparison of simple potential functions for simulating liquid water," *The Journal of Chemical Physics,* vol. 79, no. 2, pp. 926-935, 1983.

[139] M. J. Abraham, T. Murtola, R. Schulz, S. Páll, J. C. Smith, B. Hess and E. Lindhal, "GROMACS: High performance molecular simulations through multi-level parallelism from laptops to supercomputers," *SoftwareX,* Vols. 1-2, pp. 19-25, 2015.

[140] G. J. Martyna, M. Klein and M. Tuckerman, "Nosé–Hoover chains: The canonical ensemble via continuous dynamics," *The Journal of Chemical Physics,* vol. 97, no. 4, pp. 2635-2643, 1992.

[141] S. Nosé, "A molecular dynamics method for simulations in the canonical ensemble," *Molecular Physics,* vol. 52, no. 2, pp. 255-268, 1984.

[142] W. G. Hoover, "Canonical dynamics: Equilibrium phase-space distributions," *Physical Review A,* vol. 31, no. 3, pp. 1695-1697, 1985.

[143] G. J. Martyna, M. E. Tuckerman, D. J. Tobais and M. L. Klein, "Explicit reversible integrators for extended systems dynamics," *Molecular Physics,* vol. 87, no. 5, pp. 1117-1157, 1996.

[144] T. Darden, D. York and L. Pedersen, "Particle mesh Ewald: An N·log(N) method for Ewald sums in large systems," *The Journal of Chemical Physics,* vol. 98, no. 12, pp. 10089-10092, 1993.

[145] J. P. Perdew, K. Burke and M. Ernzerhof, "Generalized Gradient Approximation Made Simple," *Phys Rev Lett,* vol. 77, no. 18, pp. 3865-3868, 1996.

[146] S. Grimme, J. Antony, S. Ehrlich and H. Krieg, "A consistent and accurate ab initio parametrization of density functional dispersion correction (DFT-D) for the 94 elements H-Pu," *J Chem Phys,* vol. 132, no. 15, pp. 154104:1 - 154104:19, 2010.

[147] G. Lippert, J. Hutter and M. Parrinello, "A hybrid Gaussian and plane wave density functional scheme," *Molecular Physics,* vol. 92, no. 3, pp. 477-488, 2010.

[148] J. VandeVondele and J. Hutter, "Gaussian basis sets for accurate calculations on molecular systems in gas and condensed phases," *J Chem Phys,* vol. 127, no. 11, pp. 114105:1-114105:9, 2007.

[149] S. Goedecker, M. Teter and J. Hutter, "Separable dual-space Gaussian pseudopotentials," *Physical Review B,* vol. 54, no. 3, pp. 1703-1710, 1996.

[150] G. Bussi, D. Donadio and M. Parrinello, "Canonical sampling through velocity rescaling," *J Chem Phys,* vol. 126, no. 1, p. 014101, 2007.

[151] L. Chen, J. P. Mowat, F. Fairen-Jimenez, C. A. Morrison, S. P. Thompson, P. A. Wright and T. Düren, "Elucidating the breathing of the metal-organic framework MIL-53(Sc) with ab initio molecular dynamics simulations and in situ X-ray powder diffraction experiments," *J Am Chem Soc,* vol. 135, no. 42, pp. 15763-15773, 2013.

[152] M. J. McGrath, J. I. Siepmann, I. F. Kuo, C. J. Mundy, J. VandeVondele, J. Hutter, F. Mohamed and M. Krack, "Isobaric-isothermal monte carlo

simulations from first principles: application to liquid water at ambient conditions," *Chemphyschem,* vol. 6, no. 9, pp. 1894-901, 2005.

[153] J. Schmidt, J. VandeVondele, I. F. Kuo, D. Sebastiani, J. I. Siepmann, J. Hutter and C. J. Mundy, "Isobaric-isothermal molecular dynamics simulations utilizing density functional theory: an assessment of the structure and density of water at near-ambient conditions," *J Phys Chem B,* vol. 113, no. 35, pp. 11959-11964, 2009.

[154] S. J. Clark, M. D. Segall, C. J. Pickard, P. J. Hasnip, M. I. J. Probert, K. Refson and M. C. Payne, "First principles methods using CASTEP," *Zeitschrift für Kristallographie - Crystalline Materials,* vol. 220, no. 5/6, 2005.

[155] A. Tkatchenko and M. Scheffler, "Accurate molecular van der Waals interactions from ground-state electron density and free-atom reference data," *Phys Rev Lett,* p. 073005, 2009.

[156] D. C. Liu and J. Nocedal, "On the limited memory BFGS method for large scale optimization," *Mathematical Programming,* vol. 45, no. 1-3, pp. 503-528, 1989.

[157] G. Onyestyák, Z. Ötvös and J. Valyon, "The sorption dynamics of N_2, CO_2, CO and CH_4 in zeolite and carbon molecular sieves," *Studies in Surface Science and Catalysis,* vol. 174, no. Part A, pp. 595-598, 2008.

[158] D. M. Razmus and C. K. Hall, "Prediction of gas adsorption in 5A zeolites using Monte Carlo simulation," *AIChE Journal,* vol. 37, no. 5, pp. 769-779, 1991.

[159] R. I. Derrah and D. M. Ruthven, "Sorption of the Inert Gases (Ar, Kr, and Xe) in Type A Zeolites," *Canadian Journal of Chemistry,* vol. 53, no. 7, pp. 996-1006, 1975.

[160] T. C. Golden and S. Sircar, "Gas Adsorption on Silicalite," *Journal of Colloid and Interface Science,* vol. 162, no. 1, pp. 182-188, 1994.

[161] K. Munakata, T. Fukumatsu, S. Yamatsuki, K. Tanaka and M. Nishikawa, "Adsorption Equilibria of Krypton, Xenon, Nitrogen and Their Mixtures on Molecular Sieve 5A and Activated Charcoal," *Journal of Nuclear Science and Technology,* vol. 36, no. 9, pp. 818-829, 2012.

[162] R. E. Bazan, M. Bastos-Neto, A. Moeller, F. Dreisbach and R. Staudt, "Adsorption equilibria of O_2, Ar, Kr and Xe on activated carbon and zeolites: single component and mixture data," *Adsorption,* vol. 17, no. 2, pp. 371-383, 2011.

[163] Y. Park, S. Lee, J. Moon, D. Choi and C. Lee, "Adsorption Equilibria of O_2, N_2, and Ar on Carbon Molecular Sieve and Zeolites 10X, 13X, and LiX," *Journal of Chemical & Engineering Data,* vol. 51, no. 3, pp. 1001-1008, 2006.

[164] M. Van De Voorde, H. Verelst and G. V. Baron, "Measurement of O_2-N_2 binary sorption on 5A zeolite by isotope tracer and perturbation chromatography," *Journal of Porous Materials,* vol. 2, no. 1, pp. 51-57, 1995.

[165] International Zeolite Association (IZA), "Framework FAU," [Online]. Available: http://europe.iza-structure.org/IZA-SC/framework.php?STC=FAU.

[166] International Zeolite Association (IZA), "Framework LTA," [Online]. Available: http://europe.iza-structure.org/IZA-SC/framework.php?STC=LTA.

A. Appendix A: Forcefield parameters

In this section, a full list of the classical simulation parameters is given below.

A.1.Physical parameters

The charges on the framework atoms are given by Table A.1. The Lennard Jones parameters for the framework and cations are given by Table A.2 and in Table A.3 for the gases.

Table A.1: Framework charges

Charge (e^-)	No cations	20 cations	40 cations	60 cations
Si	+2	1.9637059471	1.9440198238	1.9243337004
Al	n/a	1.6605517621	1.4814295154	1.4085980176
O	-1	-1	-1	-1
cation	n/a	+1	+1	+1
Charge (e^-)	78 cations	100 cations	150 cations	192 cations
Si	1.9066161894	1.8849614537	1.8357461454	1.7944052863
Al	1.3663518720	1.3267094714	1.2562360132	1.2055947137
O	-1	-1	-1	-1
cation	+1	+1	+1	+1

Table A.2: Lennard Jones parameters

	sigma (Å)	epsilon (K)	Source
Si	3.92	301.9	[63]
Al	3.92	327.09	[63]
O	3.15	76.49	[63]
Li	1.4582	34.02	[48]
Na (Aqvist et al.)	1.825	13.248	[48]
Na (Akten et al.)	2.85	8	[49]

Table A.3: Lennard Jones parameters of gases

	sigma (Å)	epsilon (K)	Charge	Source
Carbon in CO_2	2.757	28.129	+0.6512	[56] [139]
Oxygen in CO_2	3.033	80.507	-0.3256	[56] [139]
Carbon in CH_4	3.344	25.6644	-0.572	[56]
Hydrogen in CH_4	2.641	27.6772	+0.143	[56]
Nitrogen in N_2	3.31	36	-0.482	[60]
COM in N_2	0	0	+0.964	[60]
Oxygen in O_2	3.02	49	-0.113	[60]
COM in O_2	0	0	+0.226	[60]
Hydrogen H_2O	0	0	+0.41	[140]
Oxygen in H_2O	3.15	76.59	-0.82	[140]
He	2.104	28.1805	0	[47]
Ar	3.446	93.0962	0	[47]
Kr	3.689	110.71	0	[47]
Xe	3.924	167.07	0	[47]

Mixing rules between all atoms use the standard Lorentz-Berthelot rules in Equation (3.11) and (3.12). All Lennard-Jones interactions between gas molecules and silicon/aluminium atoms are turned off. As described in Chapter 3, for Na^+ the parameters by Aqvist et al. [48] are used for all interactions except for the interactions with the framework oxygen where the Lennard-Jones interaction parameters from Akten et al. [49] are used.

To describe the bonded interactions the parameters in Table A.4 are used. The spring constants are doubled in most MD packages (including GROMACS) to account for the factor of two difference in the CHARMM [64] interpretation.

Table A.4: Bonded interactions for framework

Bond	DFT (Å)	Spring constant (kcal/mol/Å^2)	Source
Si-O	1.635	300	[46]/this work
Al-O	1.761	222	[46]/this work
Si-Si (Urey-Bradley)	3.045	30	[46]/this work
Si-Al (Urey-Bradley)	3.073	30	[46]/this work
Bend	**DFT (degrees)**	**Spring constant (kcal/mol/rad^2)**	**Source**
O-Si-O	109.4	75	[46]/this work
O-Al-O	109.3	65	[46]/this work
Si-O-Si	131.9	30	[46]/this work
Si-O-Al	136.2	30	[46]/this work

To describe the bonded interactions in CO_2 and CH_4, the following parameters are used. For O_2 and N_2, the molecules are held rigid.

Table A.5: CO_2 bonded parameters

Bond stretch	bond length (Å)	Epsilon (kcal/mol/Å^2)	Source
C-O	1.178	979.46	[139]

Bond Bend	Equilibrium angle (degrees)	Epsilon (kcal/mol/rad^2)	Source
O-C-O	180	52.76	[139]

Urey Bradley	bond length (Å)	Epsilon (kcal/mol/Å^2)	Source
O-(C)-O	2.353	86.77	[139]

Table A.6: CH_4 bonded parameters

Bond stretch	bond length (Å)	Epsilon (kcal/mol/Å^2)	Source
C-H	1.099	333.74	[139]

Bond Bend	Equilibrium angle (degrees)	Epsilon (kcal/mol/rad^2)	Source
H-C-H	109.47	28.52	[139]

Urey Bradley	bond length (Å)	Epsilon (kcal/mol/Å^2)	Source
H-(C)-H	1.793	18.39	[139]

For the exclusion policy, k_{scale} is set to 0.385 (1-k_{scale}=0.615) for Na-RHO. For Li-RHO, k_{scale} is set to 0.36 (1-k_{scale}=0.64). For CH_4, CO_2, O_2 and N_2 a full 1-3 coulombic exclusion policy is applied within the molecules.

A.2.1-4 scale factors used

Table A.7: 1-4 scale factors used in MD simulations

Source of parameters	k_{scale} (original bonded parameters)	k_{scale} (new bonded parameters)
Akten et al. [49]	0.37	0.40
Aqvist et al. [48]	0.34	0.40
Beerdsen et al. [70]	0.37	0.41
CVFF [71]	0.38	0.41
Cygan et al. [72]	0.37	0.405
Gabrieli et al. [46]	0.37	0.4
DREIDING [73]	0.34	0.365
Garcia-Sanchez et al. (based on $\underline{C}O_2$) [56]	0.37	0.4
Garcia-Sanchez et al. (based on $C\underline{O}_2$) [69]	0.35	0.37
Halicioğlu et al. [74]	0.33	0.34
Jaramillo et al. [75]	0.35	0.37
Jeffroy et al. [55]	0.37	0.395
Jensen et al. [76]	0.36	0.38
Jensen et al. [76] (prior values)	0.37	0.395
Lamoureux et al. [77]	0.37	0.41
Larentzos et al. [78]	0.35	0.37
Lee et al. [79]	0.36	0.375
Maurin et al. [80]	0.35	0.41
Rao et al. [81]	0.33	0.375
UFF [47]	0.37	0.405
Vujic. et al. [82]	0.33	0.375
Watanabe et al. [83]	0.345	0.4

A.3.MD parameters

The majority of MD simulations reported here are completed using GROMACS 2018.1 [141], although much of the preliminary groundwork (not reported here) was done using GULP v4.5 [65] and DLPOLY4 v4.08 [66]. A time step of 1 fs is used with a velocity Verlet integrator. The cut-off for the Lennard-Jones interactions are set to 14.0 Å with force-switching applied between 13.0 Å and 14.0 to smooth the force to zero at 14.0 Å.

A set of ten chained [142] Nosé-Hoover thermostats [143] [144] are applied to control the temperature with a time constant of 0.1 ps. To control the pressure, an isotropic MTTK barostat [145] is used with at time constant of 1.0 ps.

Electrostatics are treated with the Particle Mesh Ewald (PME) method [146]. The real space cut-off is set to 14.0 Å, with Fourier grid spacing set to 1.2 Å and the Ewald tolerance set to 10^{-6}.

A.4.MC parameters

All MC simulations reported here have been completed using DLMONTE v2.03-v2.06 [87]. Similar to the MD simulations, a cut-off of 14.0 Å has been used for the Lennard-Jones potential and real space part of the Ewald summation. The Ewald tolerance is set to 10^{-6} to describe the convergence in reciprocal space. For NVT MC simulations, equally weighted molecule translation and reinsertion (atom translation) moves are attempted. For GCMC simulations, an additional insertion/deletion move (gcinsertmol) is used and where appropriate, a rotation move is applied to molecules (rotatemol). For Li/Na systems, a swap molecules move is also used (swapmols).

B. Appendix B: AIMD parameters

I would like to thank Dr Claire Hobday for providing the following description of the DFT parameters used in this work.

B.1. *Ab initio* molecular dynamics

All *ab initio* (Born-Oppenheimer) MD calculations were performed using the Quickstep module of the CP2K (version 2.6) simulation package [67]. The PBE [147] exchange-correlation functional with semi-empirical dispersion corrections to the energies and gradients from the DFT-D3 [148] method (cut-off radius 15 Å) were used throughout. Energies and forces were calculated utilizing the Gaussian plane-wave (GPW) scheme [149] or Gaussian Augmented Plane-wave (GAPW) scheme [150] which is a dual basis set method wherein a linear combination of Gaussian-type orbitals is used to describe the Kohn-Sham molecular orbitals, while the electron density is described by an auxiliary plane-wave basis set (expressed at an energy cut-off of 400 Ry, accompanied by the relative cut-off of 60 Ry for the Gaussian basis set collocation). The GAWP scheme was used for O and Na atoms and GPW scheme for Si and Al. To avoid unphysical charges, the sodium atoms were represented by double-zeta (DZVP) quality MOLOPT short range basis sets [150], while all other atoms were represented by the triple-zeta (TZV2P) quality MOLOPT basis sets [150], in conjunction with the relativistic, norm-conserving Goedecker-Teter-Hutter pseudopotentials [151], optimised for use against the PBE functional [147] . The nine outer electrons of Na were treated explicitly, but for all other atoms, only their valence electrons were. During each SCF cycle, the electronic structure was explicitly minimised to a tolerance of 10^{-7} Hartree. The equations of motion were integrated using a time step of 0.55 fs. The starting structures were taken from classical MD simulation outputs which had relatively large unit cell models, ($a = b = c = ca.$ 14.4139 Å, $\alpha = \beta = \gamma = 90°$), which by definition results in compact 1st Brillouin zones. Thus, the constraint that the

QUICKSTEP module employs Γ-point sampling only of the Brillouin zone was not a concern in this work.

For the simulations starting from the single unit cell 1 μs and REMD classical simulations, equilibration was initiated under the isobaric-isothermal ensemble regime (NPT; constant number of particles, pressure and temperature) for 2.4 ps. The temperature was set to 300 K and controlled by a canonical velocity rescaling thermostat [152] with an initial time constant of 10 fs which is gradually increased to 50 fs over the equilibration. The barostat was set up with a coupling time constant of 300 fs and an external pressure of 1 bar. In addition, a reference unit cell of constant volume was defined alongside the model to fix the number of grid points used to compute the Coulomb and exchange-correlation energies. This was used to mitigate any effects of varying grid points due to potential volume fluctuations of the simulation box. It has been shown previously that the use of such a reference cell avoids any discontinuities in the potential energy profile when the volume is permitted to vary [153] [154] [155] The unit cell parameters were then fixed at the equilibrated values and the ensemble switched to NVT for production run dynamics (4.5 ps).

For the simulations looking at the change in the unit cell length as a function of water and CO_2 content, models were initiated under the NPT ensemble. The temperature was set to 300 K and controlled by a canonical velocity rescaling thermostat [152] with a time constant of 50 fs. The barostat was set up with a coupling time constant of 300 fs and an external pressure of 1 bar. In addition, a reference unit cell of constant volume was defined alongside the model to fix the number of grid points used to compute the Coulomb and exchange-correlation energies. Trajectories were simulated for a minimum of 3 ps. To obtain the cell parameters and standard deviations, averages were taken after 1 ps to allow for equilibration.

B.2. DFT geometry optimisations

All calculations were performed using the CASTEP (version 5.11) simulation package [156]. The Hamiltonian operator was approximated using the Perdew-Burke-Ernzerhof (PBE) [147] exchange-correlation functional, with the molecular wavefunction description provided by 'RECPOT' pseudopotentials and a plane wave basis set operating at 900 eV, which gave convergence to within 4 meV per atom. In addition, the Tkatchenko-Scheffler dispersion correction was applied [157]. The electronic structure was sampled at the gamma position only in the Brillouin zone due to the large size of the primitive unit cell (resulting in a k-point sampling grid of no greater than 0.06 $Å^{-1}$). The potential energy surface was searched for energy minima by means of the limited-memory Broyden-Fletcher-Goldfarb-Shanno (LBFGS) algorithm [158]. Structures were considered to be optimised when the energy per atom, maximum force, maximum stress and maximum atomic displacement converged to the values of 0.2×10^{-4} eV $atom^{-1}$, 0.05 eV $Å^{-1}$, 0.5 GPa and 0.001 Å, respectively.

C. Appendix C: DLMONTE sample input files

C.1. FIELD file

The following field file corresponds to a 2 x 2 x 2 supercell with 78 Na^+ cations.

The combined Aqvist-Akten parameters are given.

```
Zeolite RHO simulation
CUTOFF 14
UNITS  eV
NCONFIGS 1
ATOMS 4
Al core 26.9820 1.3663518720
Na core 22.9900 1.0000000000
O core 15.9998 -1.0000000000
Si core 28.0900 1.9066161894
MOLTYPES 2
sodium
ATOMS 1 1
Na core  0.00000000 0.0000000 0.0000000
FINISH
zeolite
MAXATOM 1152
FINISH
VDW 4
Na core Na core lj 0.0011415973 1.825
Na core Si core lj 0.0054500104 2.872
Na core Al core lj 0.0056725507 2.872
Na core O core lj 0.0021316562 3.000
CLOSE
```

C.2. CONTROL file (GCMC)

```
# USE BLOCK                 # 'use' block - simulation control
use gaspressure
use ortho                   # use orthorhombic PBC for speed-up (if the cell is cubic)
use rotquaternion           # Use quartenions rather than Euler's method for rotation
finish                      # close the 'use' block

#STEPS
steps               35000000  # Number of moves to perform in simulation
equilibration       0  # Equilibration time before statistics are gathered (in moves)

# TEMPERATURE
temperature         300     # Set the temperature

# ACCEPTANCE FOR TRANSLATION
acceptmolmoveupdate  100000    # Period (in moves) at which the maximum move size is recalculated
acceptmolmoveratio   0.5       # target acceptance ratio (default is 0.37, real)
maxmoldist          0.2       # max distance to move a molecule (acceptmolmoveupdate n frequency of updating
maxmoldist

# ACCEPTANCE FOR REINSETION
acceptatmmoveupdate  99999999   # Frequency to update atom move
acceptatmmoveratio   0.5       # target acceptance ratio (default is 0.37, real)
maxatmdist          14.0      # max distance to move atom

# ACCEPTANCE FOR ROTATION
acceptmolrotupdate   100000    # Frequency to update molecule
acceptmolrotratio    0.5       # target acceptance ratio (default is 0.37, real)
maxmolrot           360       # max angle to rotate a molecule

# PRINT OPTIONS
revconformat        dlmonte   # REVCON file is in DL_POLY CONFIG format
archiveformat       dlpoly4   # ARCHIVE format
stack               100      # Size of blocks (in moves) for block averaging
yamldata            100000    # Print to YAML file every x iterations
print               100000    # Information is output every 'print' moves
check               100000    # Perform energy check every n iterations
statistics          100000    # Print to PTFILE
sample coords       100000    # Print to HISTORY file

#GCMC TRANSLATE
move molecule 2 33            # Perform translation moves for 1 molecule type X percent of the time
sodium
CO2

# GCMC INSERTION/DELETION      # Perform GCMC insertion and deletion
move gcinsertmol 1 34
CO2 8.494629248e-03

# GCMC ROTATION               # Perform rotation moves
move rotatemol 1 33
CO2

#COMMENCE SIMULATION
Start
```

C.3. CONTROL file (Replica Exchange MC)

```
# USE BLOCK                  # 'use' block - simulation control
use gaspressure
use ortho                    # use orthorhombic PBC for speed-up (if the cell is cubic)
use repexch 16  100  1000     # Replica-Exchange with 16 replicas, delta T = +100, sampling every 1000 MC
steps
finish                     # close the 'use' block

distewald                  # Spread ewald calculation over multiple cores

#STEPS
steps              40000000  # Number of moves to perform in simulation
equilibration      0         # Equilibration time before statistics are gathered (in moves)

# TEMPERATURE
temperature        300       # Set the temperature

# ACCEPTANCE FOR TRANSLATION
acceptmolmoveupdate  100000    # Period (in moves) at which the maximum move size is recalculated
acceptmolmoveratio   0.5       # target acceptance ratio (default is 0.37, real)
maxmoldist         0.2       # max distance to move a molecule (acceptmolmoveupdate n frequency of updating
maxmoldist

# ACCEPTANCE FOR REINSETION
acceptatmmoveupdate  99999999   # Frequency to update atom move
acceptatmmoveratio   0.5       # target acceptance ratio (default is 0.37, real)
maxatmdist         14.4      # max distance to move atom

# PRINT OPTIONS
revconformat       dlmonte   # REVCON file is in DL_POLY CONFIG format
archiveformat      dlpoly4   # ARCHIVE format
stack              100       # Size of blocks (in moves) for block averaging
yamldata           100000    # Print to YAML file every x iterations
print              100000    # Information is output every 'print' moves
check              100000    # Perform energy check every n iterations
statistics         100000    # Print to PTFILE
sample coords      100000    # Print to HISTORY file

#GCMC TRANSLATE
move molecule 1 50           # Perform translation moves for 1 molecule type X percent of the time
sodium

#GCMC REINSERT               # Perform reinsertion moves for 1 atom type X percent of the time
move atom 1 50
Na core

#COMMENCE SIMULATION
start
```

D. Appendix D: Sample GROMACS file

D.1.GROMPP mdp file

```
; RUN CONTROL PARAMETERS
integrator              = md-vv          ; Integrator

; LENGTH OF SIMULATION AND TIME STEP
tinit                   = 0              ; Initial time in ps
dt                      = 0.001          ; Time step in ps
nsteps                  = 1000000        ; number of steps

; TEMPERATURE AND PRESSURE OF THE SYSTEM
ref_t                   = 300            ; in K
ref_p                   = 0.0            ; in bar

# THERMOSTAT OPTIONS
Tcoupl                  = nose-hoover    ; Thermostat
tau_t                   = 0.1            ; Time constant (ps)
tc-grps                 = System         ; Groups to couple separately

; BAROSTAT OPTIONS
Pcoupl                  = MTTK           ; Barostat
Pcoupltype              = isotropic      ; Isotropic or otherwise
tau_p                   = 1.0            ; Time constant (ps)
compressibility         = 4.5e-5         ; 1/bar

; RESTART or CONTINUE: YES (1) or NO (0)
init_step               = 1              ; Restart parameter

; GENERATE VELOCITIES FOR STARTUP RUN
gen_vel                 = no             ; Generate velocities
gen_temp                = 300            ; Initial temperature to draw velocities from
gen_seed                = 1993           ; Define seed for reproducible trajectories

; VDW SETTINGS
vdw-modifier            = Force-switch   ; Smoothly switches the forces to zero between rvdw-switch and rvdw
rvdw-switch             = 1.3            ; Start switching the force
rvdw                    = 1.4            ; Cut-off
DispCorr                = EnerPres       ; Apply long range dispersion corrections for Energy and Pressure

; ELECTROSTATIC SETTINGS
coulombtype             = PME
rcoulomb                = 1.4            ; Coulombic cut-off
epsilon-r               = 1              ; Dielectric constant
fourierspacing          = 0.12           ; Spacing for the PME/PPPM FFT grid
pme_order               = 4              ; cubic interpolation
ewald_rtol              = 1e-06          ; Coulombic tolerance

; PERIODIC BOUNDARY CONDITIONS
pbc                     = xyz            ; Apply PBCs
periodic_molecules      = yes            ; Apply PBCs

; NEIGHBORSEARCHING PARAMETERS

cutoff-scheme           = Verlet         ; Verlet or group (group will be removed in the future)
```

```
nstlist                 = 5             ; Update the neighbour list every 5 steps. This will be optimised by default.
ns_type                 = grid          ; Update the neighbour list based on a grid
rlist                   = 1.4           ; This value should be set but is ignored in Verlet lists

; COM removal
comm-mode               = Linear        ; mode for center of mass motion removal - change to angular if whole
system rotates
nstcomm                 = 1             ; number of steps for center of mass motion removal
nstcalcenergy           = 1             ; number of steps for center of mass motion removal (energy)
comm_grps               = System        ; Apply COM removal to the whole system


; OUTPUT CONTROL OPTIONS
nstxout                 = 10000         ; Output coordinates every
nstvout                 = 0             ; Output velocities every
nstfout                 = 0             ; Output forces every
nstlog                  = 10000         ; Output energies to the log file every
nstenergy               = 10000         ; Output energies to energy file every
nstxout-compressed      = 10000         ; Write positions to compressed trajectory file every
```

D.2. Abridged topology file

```
;# RHO topology file

; Inter-molecular part :

[ defaults ]
; nbfunc   comb-rule   gen-pairs  fudgeLJ  fudgeQQ
1 2 no 1.0 0.600

[ atomtypes ]
; name   mass     charge ptype   sigma(nm)  epsilon (kJ/mol)
Al 26.982000  1.366352  A 0.392000 2.719600
Cx 12.000000  0.651200  A 0.275700 0.233635
Na 22.990000  1.000000  A 0.182495 0.110147
 O 15.999800 -1.000000  A 0.315000 0.635968
Ox 15.998000 -0.325600  A 0.303300 0.668687
Si 28.090000  1.906616  A 0.392000 2.510400

[ nonbond_params ]
Cx Si 1 0.00 0.00
Cx Al 1 0.00 0.00
Ox Si 1 0.00 0.00
Ox Al 1 0.00 0.00
Na O 1 0.300000 0.205674

; Intra-molecular part :

[ moleculetype ]
; Name nrexcl
SOD 0

[  atoms ]
; nr type  resnr residue  atom  cgnr charge  mass
   1 Na 1 SOD Na  1  1.000000 22.990000

; Intra-molecular part :

[ moleculetype ]
; Name nrexcl
RHO 0

[  atoms ]
; nr type  resnr residue  atom  cgnr charge  mass
   1 Al 1 RHO Al  1  1.366352 26.982000
   2 Al 1 RHO Al  1  1.366352 26.982000
   3 Al 1 RHO Al  1  1.366352 26.982000

[ bonds ]
;  ai    aj    type     r0 (nm)   ks (kJ/(mol nm2)
   1  241 1 0.176000 185769.598677
   1  570 1 0.176000 185769.598677
   1  769 1 0.176000 185769.598677
 [ angles ]
;    ai    aj    ak type    theta0 (degr)   kb (kJ/(mol rad2)
   1  241 1057 1 136.000000 58.576000
```

```
   1  570 1089 1 136.000000 58.576000
   1  769 1130 1 136.000000 58.576000
 [ pairs ]
; ai    aj  funct      f_qq    qi     qj   sigma (nm)  epsilon (kJ/mol)
   1  257 2 0.600000  1.366352 -1.000000 0.353500 1.315134
   1  318 2 0.600000  1.366352 -1.000000 0.353500 1.315134
   1  378 2 0.600000  1.366352 -1.000000 0.353500 1.315134
 [ exclusions ]
; ai    aj
    1   241
    1   257
    1   318
; Intra-molecular part :

[ moleculetype ]
; Name nrexcl
CO2 0

[  atoms ]
; nr type  resnr residue  atom  cgnr charge  mass
   1 Cx 1 CO2 Cx  1  0.651200 12.000000
   2 Ox 1 CO2 Ox  1 -0.325600 15.998000
   3 Ox 1 CO2 Ox  1 -0.325600 15.998000


[ bonds ]
;  ai    aj    type     r0 (nm)   ks (kJ/(mol nm2)
   1    2 1 0.117800 819612.122164
   1    3 1 0.117800 819612.122164
   2    3 1 0.235300 72609.135483

[ angles ]
;    ai    aj    ak type    theta0 (degr)   kb (kJ/(mol rad2)
   2    1    3 1 180.000000 441.411997
[ exclusions ]
; ai    aj
    1     2
    2     3
    1     3

[ system ]
; name
Na-RHO

[ molecules ]
; Compound   #mols
SOD 78
RHO 1
CO2 105
```

D.3.PLUMED metadynamics

```
# Define variable to bias again (the position of atom 5)
p: POSITION ATOM=5

# Activate metadynamics # depositing a Gaussian every 500 time steps,
# with height equal to 1.0 kJoule/mol,# and width 0.01 nm.
metad: METAD ARG=p.x,p.y,p.z, PACE=500 HEIGHT=1.0 SIGMA=0.01,0.01,0.01  FILE=HILLS

# Biasing against position so must ensure that a reference structure is used
FIT_TO_TEMPLATE REFERENCE=REF.pdb

# monitor the two variables and the metadynamics bias potential
PRINT STRIDE=500 ARG=p.x,p.y,p.z,metad.bias FILE=COLVAR
```

E. Appendix E: Langmuir fitting comparison

Table E.1: q_{sat} parameters for fitting with three single-site Langmuir models

Fitting	Temperature (K)	O_2	N_2	He	Ar	Kr	Xe	CH_4	CO_2
normal	285	6.061	4.417	2.6646	4.715	5.2281	4.901	6.4621	6.7062
LP	285	-15.8474	1.2977	-22.394	-18.3514	2.8796	8.1282	16.4618	6.5818
HP	285	7.0592	4.0466	2.8284	4.8962	5.2494	5.045	7.4461	7.0955
normal	300	6.3214	2.9666	2.3834	4.0178	4.3279	4.6373	6.4073	4.7186
LP	300	7.0937	2.2381	1.8259	2.4135	2.4213	7.6279	-12.3639	4.4825
HP	300	6.672	3.0852	2.7037	4.2063	4.3626	4.7907	8.0139	5.195
normal	315	5.7822	4.1846	2.525	4.3384	3.8889	4.8748	8.1911	6.096
LP	315	1.6482	4.1172	1.457	-2.7567	-229.278	3.8843	9.2363	5.891
HP	315	6.3025	3.4189	3.0042	4.2028	3.9879	4.5938	10.1385	6.6025

Table E.2: b parameters for fitting with three single-site Langmuir models

Fitting	Temperature (K)	O_2	N_2	He	Ar	Kr	Xe	CH_4	CO_2
normal	285	0.0232	0.1729	0.0061	0.0202	0.032	0.1365	0.2742	48.5743
LP	285	-2.15474	1.471265	-0.36355	-1.72324	0.484841	5.179202	21.06161	2773.849
HP	285	0.9742	3.4262	0.0462	0.4642	0.8768	3.2972	10.7194	543.8488
normal	300	0.0169	0.1942	0.0063	0.0189	0.0299	0.1021	0.1591	23.7306
LP	300	0.750523	1.224107	0.027251	0.183228	0.314753	3.46452	-9.22059	817.1519
HP	300	0.7085	1.677	0.0404	0.318	0.563	2.223	6.7677	137.5841
normal	315	0.0146	0.0722	0.0055	0.0141	0.0262	0.0671	0.0683	32.8917
LP	315	0.13949	1.42321	0.020092	-0.16709	-22.9987	1.318269	4.665106	1717.737
HP	315	0.5268	1.1456	0.0414	0.2579	0.4046	1.5412	5.2376	315.4588

Negative values indicate an intercept below the origin. These results are mathematically correct but indicate a poor fit (only positive values are physical).

F. Appendix F: Comparison of Na-RHO with other zeolites

F.1. CO_2/CH_4

Table F.1: Isosteric Heats of Adsorption (CO_2/CH_4)

kJ/mol	CO_2	CH_4	Type
Na-RHO	-40.3	-25.4	Simulated
Zeolite-5A	-40	-20	Experimental [115]

Table F.2: Henry's constant (CO_2/CH_4)

mmol/g/bar	CO_2	CH_4	Type
Na-RHO	483	1.03	Simulated
Na-5A	1280	3.5	Experimental [159]

Table F.3: Comparison of uptake (CO_2/CH_4)

	CO_2	CH_4	Type
Zeolite-5A (9 bar/303 K)	3.8 mmol/g	1.8 mmol/g	Experimental [115]
Na-RHO (1 bar/298 K)	4.9 mmol/g	0.1 mmol/g	Experimental [7]

F.2. Noble Gases

Table F.4: Isosteric Heats of Adsorption (noble gases)

kJ/mol	Ar	Kr	Xe	Type
Zeolite – 5 A	-14 [160]	-18 [161]	-24 [161]	Experimental
Na-RHO	-11	-12.5	-17.5	Simulated

Table F.5: Henry's Constants (noble gases)

mmol/g/bar	Ar	Kr	Xe	Type
Zeolite 4A (283 K)	n/a	0.42	n/a	Experimental [122]
Silicalite (MFI) 305 K	0.174	0.7	n/a	Experimental [162]
Zeolite 5A (300 K)	n/a	n/a	0.8	Experimental [163]
Na-RHO (298 K)	0.07	0.02	0.46	Simulated

Table F.6: Comparison of uptake (noble gases)

mmol/g	Ar	Kr	Xe	Type
Zeolite – 13X (10 bar 303 K)	0.7	4	9.9	Experimental [164]
Na-RHO (298 K 9 bar)	0.6	0.9	2.2	Simulated

F.3. O_2/N_2

Table F.7: Isosteric heat of adsorption (O_2/N_2)

	O_2	N_2	Type
Zeolite-13X	-7 kJ/mol	-17 kJ/mol	Experimental [165]
Na-RHO	-12.7 kJ/mol	-23.6 kJ/mol	Simulated

Table F.8: Henry's constants (O_2/N_2)

mmol/g/bar	O_2	N_2	Type
Zeolite-5A	0.138	0.514	Experimental [166]
Na-RHO	0.11	0.44	Simulated

Table F.9: Comparison of uptake (O_2/N_2)

	O_2	N_2	Type
Zeolite-13X (0.6 bar/303 K)	0.06	0.152	Experimental [165]
Na-RHO (1 bar/298 K)	0.06	0.3	Simulated